Electrorheology for Smart Automotive Suspensions

Final Technical Report

Contract No. DAAE07-92-C-R078
UMTRI No. UMTRI-94-15

Submitted to:

U.S. Army
Tank-Automotive Command

By:

The University of Michigan
Transportation Research Institute

290. Baxter Road
Ann Arbor, Michigan 48109-2150

June, 1994

UMTRI The University of Michigan Transportation Research Institute

Technical Report Documentation Page

1. Report No.	2. Government Accession No.	3. Recipient's Catalog No.

4. Title and Subtitle	5. Report Date
Electrorheology For Smart Automotive Suspensions	June, 1994
	6. Performing Organization Code
7. Author(s) Lou, Z.; Winkler, C.B.; Ervin, R.D.; Filisko, F.E.; Filisko, F.E.;Venhovens,P.J.Th.; Johnson,G.E.	8. Performing Organization Report No. UMTRI-94-15
9. Performing Organization Name and Address The University of Michigan Transportation Research Institute 2901 Baxter Road, Ann Arbor, Michigan 48109	10. Work Unit No. (TRAIS) 11. Contract or Grant No. DAAE07-92-C-R078
12. Sponsoring Agency Name and Address U.S. Army Tank-Automotive Command Department of the Army Warren, Michigan 48397-5000 Attn: AMSTRA-RTS	13. Type of Report and Period Covered Final 14. Sponsoring Agency Code 13633

15. Supplementary Notes

COTR: Ms. Nancy Saxon, Mr. Wesley Byls.na

16. Abstract

The purpose of the work reported was to demonstrate the suitability of electrorheological (ER) technology for adaptive control of suspension forces on tracked and wheeled vehicles. The mechanical shear strength properties of ER fluids change in response to the application of an electric field. The change is very rapid and fully reversible. This property was used to create an automotive suspension damper whose resistive force is readily controlled by an external electrical signal. The device was applied in a semiactive suspension system for the Army's high mobility multipurpose wheeled vehicle (HMMWV). The work reported covers a range of development tasks including definition of the semiactive control algorithm, ER fluid formulation, design and fabrication of an ER damper, design of an electrical control circuit, creation of a quarter-HMMWV test stand for the simulation of ride vibrations, laboratory measurement of the ER-damped performance characteristics over a range of physically simulated operating conditions, and computer simulation of the quarter-HMMWV system. The research demonstrated that an ER damper and appropriate control circuits could out perform the conventional hydraulic shock absorber, but that various complexities tend to impede broad application of electrorheology in automotive devices.

17. Key Words	18. Distribution Statement
electrorheological fluid, semiactive suspension, high mobility multipurpose wheeled vehicle (HMMWV)	No restrictions. Available through the National Technical Information Service, Springfield, VA 22161

19. Security Classif. (of this report)	20. Security Classif. (of this page)	21. No. of Pages	22. Price
		154	

TABLE OF CONTENTS

Section *Page*

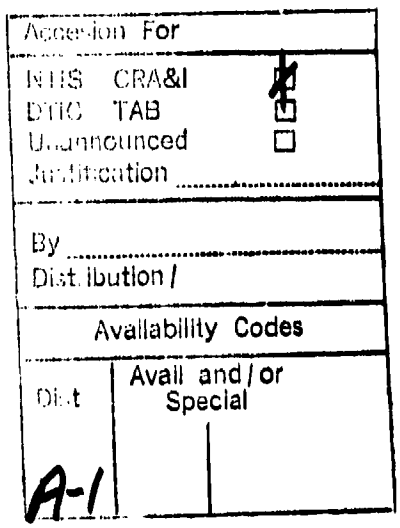

LIST OF FIGURES

LIST OF TABLES

1. Introduction

This document constitutes the final report on a research study entitled "Electrorheology for Smart Automotive Suspensions", sponsored by the U.S. Army Tank Automotive Command (TACOM) under contract No. DAAE07-92-C-R078. The purpose of the project was to demonstrate the suitability of electrorheological (ER) technology for creating adaptive control of suspension forces on tracked and wheeled vehicles. Insofar as ER fluids offer an inherent electrical-to-mechanical interface, the technology is of interest wherever the need exists for the active electronic control of a mechanical function. In the case of motor vehicles, active suspensions offer a means of managing a broad range of variables that otherwise aggravate ride vibrations when only a fixed damping device is installed. Without an active damping function, for example, a fixed shock absorber must be designed for the mean operating condition, offering *too much damping* when the vehicle is unladen and, say, running on roads, but *too little damping* when the vehicle is fully loaded and is traversing rough terrain. It is also not possible, using a passive device, to phase the delivery of damping forces so that ride quality is optimized even within a single cycle of motion. Although the traditional tools of electrohydraulics have been examined for creating active dampers for motor vehicles, the control devices have typically been rather complex and the broad set of system requirements have generally militated against their frequent application.

Since ER fluids offer an inherent medium for mechanical control, there has been an interest in exploring the suitability of this technology for the active control of automotive damping. The basic concept that was explored in this project involved using the fluid in a device that directly substituted for the conventional shock absorber of the Army's high-mobility, multipurpose, wheeled vehicle (HMMWV). The monitoring of vehicle motions using accelerometers and stroke transducers provided the basis for deriving an electrical signal, which was applied as a *command signal* to the ER-controlled device. The instantaneous *thickening* of the fluid with increasing signal level produces a resistance to motion which is calculated to manage the gross ride vibrations which accrue.

The work reported here covers a range of development tasks including fluid formulation, development of an ER device design, fabrication of an ER-active damper, design of an electrical control circuit, simulation of ride vibrations, creation of a quarter-HMMWV test stand, and laboratory measurement of the ER-damped performance characteristics over a range of physically simulated operating conditions.

This introduction is followed by an executive summary of the project. The third chapter of the report provides an overview of vehicle suspension control, introducing the notions of passive, active, and semiactive control, as well as the use of ER devices as dampers. Chapter 4 discusses the steps that have been taken to create a suitable ER fluid for use in an active damping device that is scaled for the HMMWV application. Chapter 5 addresses the specific control strategy and the ER damper design developed for the HMMWV in this project. Chapter 6 is a review of the physical testing of the ER damper. This includes a description of a quarter-HMMWV dynamometer created for the purpose,

as well as a presentation of test data. Finally, a simulation study of the ER device's performance in a quarter-HMMWV model is reviewed in chapter 7.

2. Executive Summary

The project combined analytical, design, and experimental tasks in a study of electrorheological (ER) technology applied to the real-time control of the suspension of the Army's high-mobility, multipurpose, wheeled vehicle (HMMWV). ER technology is based upon certain fluids which offer a change in their mechanical properties in response to a strong electrical field. The changes essentially involve resistance to flow and are entirely reversible and very broad in temporal bandwidth. An ER device, then, is a mechanical actuator, damper, valve, or other element which contains an ER fluid and is configured to apply an electric field across it for the sake of realizing a net mechanical outcome. In this project, an ER-based damping device was substituted for the standard hydraulic shock absorber from an HMMWV suspension to effect a semiactive damping control function. The overall effort combined the following elements: (1) the development and production of a laboratory quantity of ER fluid, (2) characterization of active properties of the ER fluid, (3) development of an ER damper suited to the mechanical constraints of the HMMWV application, (4) simulation of the damper device as the active element in a quarter-HMMWV model (i.e., one wheel and suspension assembly supporting one-quarter of the vehicle's mass), (5) assembly of a quarter-vehicle test stand for laboratory measurements, (6) fabrication and unit testing of an ER damper and (7) evaluation of the performance of the ER damper by means of laboratory testing on a quarter-HMMWV mockup.

The principle behind design of the ER damper in this project involves the *static stress* capability which an ER fluid develops in response to an electrical field. That is, the electric field strength causes the fluid to appear as a limited-strength solid—analogous, say, to a stick of butter. After shearing commences, the fluid's resistance to flow depends increasingly on its baseline viscosity and less on the ER effect of the static stress characteristic. Thus, ER devices give the maximum degree of control over a mechanical outcome if they can work the ER fluid in the vicinity of the near-static condition. This principle was implemented in the design of an ER suspension damper by incorporating a screw-actuated device in which a stack of rotary fins shear the ER fluid at relatively low speed, in resisting the motions of the HMMWV suspension.

The prototype ER damper was sized to fit within the coil spring of the HMMWV suspension, essentially taking the space otherwise occupied by the conventional hydraulic shock absorber. The device was connected to a high-voltage amplifier that applies the electric field across alternating pairs of rotary plates, between which resides the ER fluid. Measurements taken on this device alone, in a test stand, showed that it produced a static force of 700 pounds when energized at a level that is seen as reasonable for long-term operation. Results obtained by comparing the ride vibrations achieved with the ER damper (as opposed to the conventional HMMWV shock absorber) showed improved levels of isolation with the ER device. The primary basis for improvement stems from the fact that active control of the ER damper allows the precise phasing of damping forces so as to optimally oppose the motions of the sprung mass, regardless of the immediate state of the excitation arriving at the wheels. The fact that ER fluids respond

within a few milliseconds provides the inherent speed for accomplishing virtually instantaneous adjustments, well into the frequency range that is above that of wheel-hop motions.

The conclusion of this exercise is that ER technology, while still unrefined in many respects, is an inherently powerful tool offering completely new mechanisms for active control of automotive functions. The principal limitation in the technology at present, pertains to the levels of static shear stress that can be delivered under the fully energized condition. Lesser issues pertain to the settling of solid particulates, the entrainment of air or other vapor bubbles, which permit electrical arcing, and reduction of the levels of electrical voltage required. The rather high level of development of both ER fluids and ER applications technology that is proceeding in private industry suggests that major advances in all of these areas of deficiency should be expected.

3. An Introduction to Vehicle Suspension Control Techniques

The fundamentals of the conventional, passive vehicle suspension are reasonable well understood. Nevertheless, good design requires compromise among passenger ride comfort, requirement for suspension working space, variation in tire/ground contact-force variation, and vehicle attitude control (Sharp and Crolla, 1987b).

A conventional passive suspension consists of a fixed set of components, which implement predetermined spring and damping functions. These spring and damping functions may be complex, incorporating discontinuous responses in differing ranges of speed and stroke, but the operation is entirely mechanical and involves no external energy source. Selection of damper settings is a compromise between ride vibration isolation and control of wheel-hop resonance. Optimal design can be made only under a defined set of conditions, although combinations of road condition, vehicle loading, tire inflation pressure, etc. may vary greatly. In other words, off-optimality is incurred when the system state moves away from the assumed design conditions, which is unavoidable.

In order to improve the overall performance of automotive vehicles, suspensions incorporating active or semiactive components have been developed. *Active* implies that the system uses an external energy source; *semiactive*, that adaptive logic is employed which changes the system properties depending on circumstance. The idea of using active devices to generate suspension forces dates back at least to the 1960s, and this interest has remained until the present, because of the large potential market (Karnopp, 1990). From a control theory point of view, the introduction of active damping forces would be expected to increase system performance. The idea that various active forces really need to be generated by some sort of servomechanism is not particularly attractive in most cases. Most force generators are complex, inefficient, and limited in frequency response. With their necessary power supplies, they tend to be much more expensive, bulky, massive, and delicate than passive elements. This led to the consideration of semiactive force generators such as the semiactive damper (Alanoly and Sankar, 1987; Karnopp, 1990; Karnopp et al., 1974). The idea is to modulate the dissipation in a basically passive damper as a function of sensed variables such as mass velocities.

Passive Suspensions

A conventional passive suspension usually consists of a spring and a shock absorber (a damper). The spring can only store and return energy for some portion of a suspension cycle, and the shock absorber can only dissipate energy. The damping properties of the passive suspension are constant. There is no means of supplying external energy or signal to the system for controlling of the suspension properties.

In order to cover a broad set of conditions, a passive system can be designed to have parameters varying with stroke or velocity of the suspension system. For example, the orifice area varies with the stroke through a needle or plunger with a variable area. Check

valves can be used to obtain velocity-dependent variation, while pressure-relief valves can be used to obtain load- or velocity-dependent properties. However, most military and commercial vehicles have a weight-change factor of two- or three-to-one. The range of the operating conditions often exceeds the coverage obtained by varying parameters passively.

Active Suspensions

An active suspension is a system in which an actuator either totally replaces the conventional spring and damper elements or acts in parallel with a spring. Active suspensions require external power to drive the actuators, which are normally hydraulic cylinders, to generate the desired forces in the suspensions. Such systems can be further classified into two categories: slow-active and fast-active suspensions. The bandwidth of a slow-active system provides for actuation at frequencies higher than that of sprung-mass resonance but lower than that of the fundamental wheel-hop vibration, while the bandwidth of a fast-active system extends beyond the domain of wheel-hop frequencies. The bandwidth of active systems is mainly limited by the type of actuators used although the control strategy also plays an important role. The slow-active systems would typically have a bandwidth around 3 hz and would employ pneumatic actuators (Cho and Hedrick, 1985), oleo pneumatic actuators (Crolla *et al.*, 1987), d.c. motor-driven lead screws (Sharp and Crolla, 1987b), and hydraulic actuators controlled by relatively inexpensive proportional valves (Inagaki *et al.*, 1992). Successful fast-active systems have generally required stiff hydraulic actuators controlled by expensive, precision servo valves.

Among the slow-active types of actuators, pneumatic devices have served to trim out static loads, acting in parallel with mechanical springs. Such actuators perform simply as soft springs when exercised at load frequencies that are beyond their response bandwidth, such that the suspension spring rate stays at the base rate. Stiff hydraulic actuators as well as motor-driven lead screws have also been employed in relatively slow-active systems, being mounted in series with mechanical springs (Sharp and Crolla, 1987b) when load trimming is, again, the objective. Among these variations, pneumatic actuators are treated as variable-force actuators, while hydraulic and mechanical lead screw devices are seen as displacement producers changing the preload on a conventional spring. If the spring is highly nonlinear, as with most multileaf springs, a higher preload also avails a higher local value of spring-rate.

The actuators required for fast-active suspensions are often not suitable for use in mass produced vehicles such as cars and trucks (Karnopp and Heess, 1991). Since the energy-input requirements are high, especially when addressing high frequency suspension activity, the fast-active alternative is adverse to fuel economy goals. The Toyota Motor Corporation, for example, recently abandoned their prototype work on fast-active suspensions as impracticable for the foreseeable future and moved, instead, to develop slow-active systems (Inagaki *et al.*, 1992).

In a slow-active suspension, the active component generally performs the leveling function only, while its conventional spring-damper subsystem is specially tailored for high frequency performance. Therefore, the functions of attitude control and isolation are

separated. Slow-active systems have been shown to be competitive with fast-active systems in certain constrained applications (Cho and Hedrick, 1985; Pollard and Simons, 1984; Sharp and Crolla, 1987a). However, a slow-active system may exhibit deficiencies when the range of condition variables is large and, yet, performance expectations are high (Sharp and Crolla, 1987a). In particular, slow-active systems fail to handle wide-ranging conditions when no mechanism of variable damping control is provided.

Semiactive suspensions

The most common semiactive susp nsions are those whose damping characteristic is adaptively controlled, although some have also entailed direct control of the spring characteristic (Mizuguchi *et al.*, 1984). In the spring case, however, varying the stiffness without, at the same time, effectively varying the free length of the spring produces the undesirable results of having unpredictable distribution of load on the four wheels of a cornering vehicle. Solving this problem may be more difficult than solving those of a fully active system (Sharp and Crolla, 1987b). Recognizing this issue, the following discussion is limited to semiactive suspensions having controllable damping. Such systems can be further classified into two sub categories: force-controlled and resistance-controlled (Karnopp, 1990).

In the force-controlled semiactive system, the damping force is made to be dependent only upon the sign of the relative velocity; that is, the damping force is rendered more or less independent of the magnitude of the relative velocity. The damping force is raised to a step function in the tension portion of the cycle and set to zero on the compression stroke. This kind of control can be accomplished by (a) using hydraulic shock absorbers with electromagnetically loaded pressure control valves (Hamilton, 1985; Karnopp *et al.*, 1974; Krasnicki, 1980a; Krasnicki, 1980b), or (b) incorporating a force sensor and a force control feedback loop (Karnopp, 1990), or (c) using an electromagnetic damper (Karnopp, 1987).

In the resistance-controlled semiactive system, the control target is the ratio of the damping force and relative velocity. In a hydraulic type of system, the damping force can be controlled by changing either the fluid viscosity or the orifice area. Control utilizing fluid viscosity variation will be effective only with long-orifice designs. Since the viscosity of conventional hydraulic fluids can be controlled only by thermal regulation, no feasible control techniques using conventional fluids exist. Two other possible approaches toward viscosity modulation involve ferromagnetic and electrorheological (ER) fluids. The use of ferromagnetic fluids is generally eliminated from automotive consideration by their demand for high levels of electric power, although recent research has indicated a promising new approach (Pinkos *et al.*, 1993). ER fluids offer a solution which avoids both thermal and power-based adjustments in viscous response and which may be practicably scaled for automotive application.

As for changing orifice area to effect semiactive control, the function can be implemented either continuously or discretely. The continuous approach is to regulate the cross-sectional area or opening of a short orifice or valve port. The most developed technologies in this regard involve electrohydraulic servo valves. In such devices,

actuation energy is needed to drive a valve spool, typically through either electromagnetic or piezoelectric media. The discrete approach is to control the availability of flow passages (each of which has a fixed resistance property) to obtain various discrete increments in a control law governing total resistance. This approach can be realized using solenoid-controlled on-off valves, although there tend to be transient disturbances during the on-off switching (Karnopp *et al.*, 1974; Margolis and Goshtasbpour, 1984).

With its much simpler design, better efficiency and lower cost, a semiactive suspension may compete well against active suspensions in practical terms while delivering performance that is much superior to that of passive suspensions (Hrovat *et al.*, 1980; Karnopp, 1990; Katsuda *et al.*, 1992; Kimbrough, 1986; Margolis, 1982; Margolis, 1983; Redfield, 1991). As far as controlling body motion due to roadway unevenness is concerned, semiactive systems can be virtually as effective as fully active systems using state variable feedback (Karnopp, 1990).

Control of Damping by Means of ER Fluid Devices

Although a variety of rather complex changes in the mechanical and electrical properties of electrorheological fluids have been observed in response to an imposed electrical field, the primary characteristic upon which most ER devices seek to operate is the static shear resistance which arises exponentially with increasing field strength. This phenomenon accounts for the common observation that ER fluids can exhibit the properties of a solid, when "energized," and a liquid when de-energized. The electrical field condition is imposed upon a sample of fluid by containing the sample between two opposing electrodes which are energized to some voltage. In order to realize a mechanical stress response from the fluid, a mechanical shear condition is established—typically by inducing flow of the fluid between the electrodes or by translating one electrode relative to the other.

Figure 1 shows the basic characteristic of the so-called *Bingham plastic* model of electrorheological response. As field strength increases, an essentially static stress response to shear is observed. Exceeding the static strength level causes the fluid to shear more or less according to the behavior of Newtonian liquids, assuming that a Newtonian fluid medium has been employed as the liquid phase of the material.

Since the imposed field strength has virtually no influence on the shear stress levels developed at increasing levels of shear rate (i.e., the slopes in the figure are virtually the same across the range of E values, indicating that viscosity, per se, is essentially unaffected by the electric field), it is desirable practice to design devices to operate in the regime of low shear rates. By this approach, variation in the electrical signal level more directly controls the mechanical (stress-based) response, thus increasing the control efficiency of the system package. The shear rate regime can be modified, of course, by changing the nominal gains or gear ratios which directly determine either the flow of the fluid through an electrode gap or the translational movement of the electrodes causing uniform shear across the gap.

The particular variety of semiactive suspension that has been pursued in this study involves an ER controllable damper having parallel rotating disks. It is noted that a

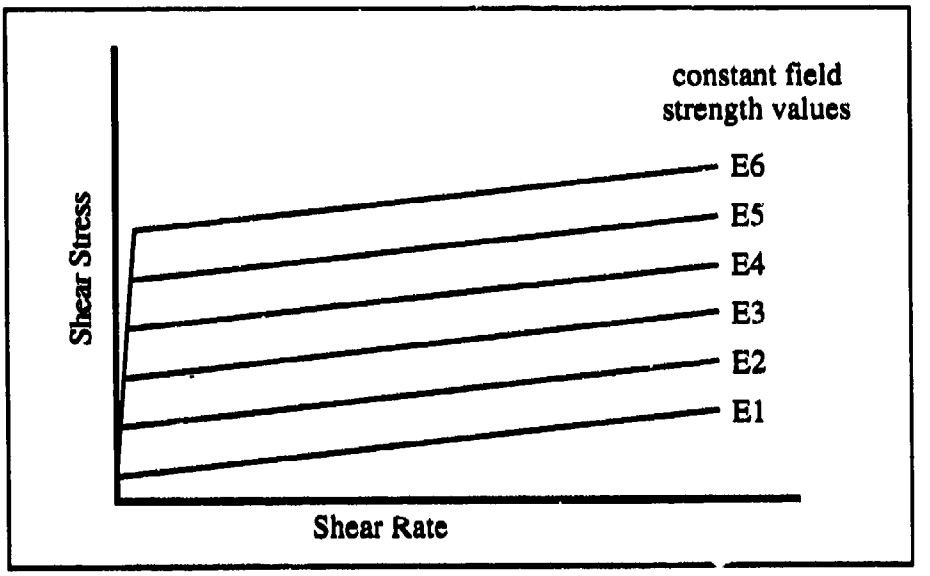

Figure 1. Electrorheologic response per the classical Bingham model

simple prototype of ER damper with concentric-cylinder electrodes has also been tested by Coulter (Coulter, 1993) at Lehigh University within the same time frame as the current Michigan research.

4. An Electrorheological Test Fluid

Within this project, alternative formulations of electrorheological fluid were examined in an attempt to improve upon fluid shear strength capability and to reduce settling of the particulate component in ER suspensions. Four alternative fluid categories were examined, namely, 1) homogenous solutions, 2) colloidal dispersions or gels, 3) amorphous substituted alumino-silicates, and 4) a zeolite-based suspension that was ultimately used as the fluid specimen for testing the automotive damping device in this study. The consideration of each will be discussed below.

Homogenous Solutions

ER active *solutions* present the ideal conceptual approach for solving the problem of settling that is otherwise seen in the multiphase (suspension) materials most commonly used as ER fluids. That is, a solution is, by definition, a single phase system that is inherently stable in terms of the physical distribution of its constituents. Recent discoveries have shown that solutions of poly gamma benzyl-L-glutamate (PBLG) and poly n-hexyl isocyanates (PHIC) exhibit an ER-active behavior. The PBLGs, although ER active in many solvents, are known to be soluble only in polar solvents, resulting in relatively high levels of conductivity and thus requiring rather high levels of electrical power for sustaining the electric field condition.

For this and other reasons, PHIC systems were examined in this study, seeking 25 to 30 percent concentrations of this solute in nonpolar solvents such as xylene and toluene. The selected solvents are also attractive because of their substantially lower cost than the PBLGs. Unfortunately, since the PHIC materials are not commercially available, it was necessary to develop procedures for preparing them in the laboratory. Initial plans were for preparing samples of PHIC from the monomer form, hexyl isocyanate, but it was discovered that only small quantities were available, from a single U.S. vendor, and that the highly costly material could be obtained only when ordered with a nine-month lead time. Accordingly, steps were taken to synthesize the monomer in our laboratories from more readily available base materials (heptanoyl chloride and sodium azide). Published procedures for this synthesis were substantially modified to yield the product quantities and the quality of molecular weight control that the ER application required. Approximately 1000 grams of PHIC was prepared, yielding 4 liters of an ER solution. The solutions thus prepared were found to be substantially ER-active but exhibited properties which were poorer than those of more common fluids prepared by other methods. Since it was not possible, within this project, to further improve the materials by synthetically modifying the components, the search for a suitable ER solution was discontinued.

Colloidal Dispersions/Gels

By a second approach, steps were taken to prepare ER fluids which, under quiescent or static conditions, would constitute a gel which inherently resists settling of a particulate phase of the materials. The desired gel formulation, of course, would exhibit an ER response to an electric field but would otherwise have a very low viscosity when deformed over a range of shear rate values. Various colloidal, as opposed to soluble, gelling agents were used primarily because the colloidal systems produce gels that are highly shear-thinning. By this approach, the gel effect would hold the fluid in a semi-solid state, at rest, presenting an essentially zero static shear strength in the absence of an electric field. Upon even very slight initial loading, the gel would yield and thereafter exhibit a very low viscosity (i.e., thinning) response to increasing shear rate.

Although many colloidal agents were studied, the most promising was a montmorillonite clay modified so that it could be readily dispersed into an organic liquid. The ER-active behavior was achieved by using standard zeolite particles dispersed into paraffin oil with 1 to 2 percent organo-clay added. The fluids had the appearance of jelly but were seen to be highly thinning, even at shear rates down to 0.001 per second. This approach is not known to have been reported previously. Although it is believed to offer a promising approach to achieving stable ER-active suspensions, it was found that the gelled fluid could not be easily loaded into the ER damping device considered here. That is, since the gel-based fluid retains a static shape, it was not possible to fill a complex device with the fluid without entraining a great number of small air pockets. Entrained air is problematic in ER devices because the high field strengths required for the ER effect produce ionic breakdown and arcing across the bubbles. The arcing, in turn, tends to saturate the supply amplifier and thereby disturb the continuous nature of the ER energization voltage. Also, arcing can lead to breakdown of many insulating materials and to the introduction of metallic "spatter" which, itself, can form bridges for further short circuit paths through the fluid. Additionally, optimization of properties of these fluids and techniques for dispersing the clays into the liquids are not straightforward and will require substantial research for their refinement.

Amorphous Substituted Alumino-Silicates

The term, *zeolite*, applies to a crystalline form of alumino-silicates (Al/Si) that were observed by University of Michigan researchers to be an effective ER-active particulate. Amorphous forms of Al/Si as the dispersed phase in ER fluids have also been shown to produce ER active suspensions. The amorphous materials are intrinsically more attractive because the chemistry can be much more radically varied without concern for constraints on the crystalline structure and because the materials are much less hydrophilic than the crystalline (water entrainment on ER particulates is undesirable because of the higher conductivity level that accrues). Seeking the combined qualities of ready synthesis and dry particles, efforts were taken to develop amorphous ER materials during this study. While this task was carried out only to a preliminary level of achievement, the effort was successful in varying the Al/Si ratio over large ranges and in combining the silicon atoms with a wide variety of elements other than Al. These include

boron, germanium, cesium, and silver. Although much work remains to be done, small fluid samples were produced showing ER shear strengths three to four times greater than those which have been achieved customarily using the crystalline materials (zeolites). Research continues in this area, given indications that further increases in static stress capability are possible.

The ER Fluid Used in the Damper for the HMMWV

Toward the conclusion of this study, a relatively conventional form of (nominally-dry) ER fluid was prepared using commercial zeolite particulate dispersed into a medium of transformer oil. The fluid was quite low in conductivity and yielded a shear strength of approximately 0.15 psi in response to an electric field of 3000 volts per millimeter. The very crucial shear strength question is only modestly addressed in this fluid sample. Indeed it is generally accepted that fluid strengths in excess of 1 psi will be needed before ER fluids are broadly attractive for automotive applications, such as in active damping devices. Nevertheless, as the following sections of this document will show, a workable device was created and demonstrated in this project.

The particulate phase of the test fluid did tend to settle when left on the shelf, requiring substantial agitation to redisperse the thick layer that would form within a few days or so. When loaded into the test device, the system was kept in a mild state of agitation so as to simply avoid the settling problem for the duration of testing. The ancillary research thrusts outlined in the previous subsections indicate that while various approaches exist for resolving specific shortcomings in ER fluids, a substantial degree of further refinement is still needed.

5. Design of a Semiactive Suspension System and ER Damper for the HMMWV

In this chapter, substantive issues of the ER application to suspension damping on the HMMWV will be addressed. These issues include the semiactive control strategy, the basis for an ER damper concept given certain generic features of ER fluid behavior, the configuring of a prototype damping device which is scaled to the physical constraints of the HMMWV suspension, and simulation of the dynamic response of this device under conditions that approximate HMMWV operations on selected roadways from Army proving grounds. In the first subsection, a presentation of the semiactive control strategy known as the *skyhook damper* is given. (Later, this skyhook algorithm will be incorporated to operate the ER damper.) Then, a parametric study of the basic design options establishes the principle that ER damper performance is optimized in devices which shear the fluid at relatively low rates. This finding derives from the observation that the electrical field condition controls a *static shear stress* characteristic of the fluid. Given this principle, the discussion proceeds to lay out a design in which the fluid in a specialized ER damper is sheared at low rate, throughout the operating range of the HMMWV. The device in question comprises a screw mechanism which is advanced through a carrier *nut* which, in turn, serves to rotate a number of disks between which ER fluid is sheared. The screw/nut mechanism provides a major reduction in the velocities over which fluid shear is imposed.

The Semiactive Control Strategy

In this section the design of the semiactive control strategy used to implement an ER damper in this project, will be discussed. As stated earlier, the distinction between active and semiactive control lies in the field of force generation. Adjustable damper systems (such as the ER-damper) can only dissipate energy whereas active systems can also generate energy. However, this restriction does not necessarily imply that the performance of semiactive systems is inferior to active suspension systems.

Semiactive suspension control is based on similar control algorithms as applied to active suspension systems. However, the most important difference between active and semiactive systems is that a semiactively damped suspension is only capable of dissipating energy. Since the adjustable damper cannot supply power to the system, the best it can do is to generate no damping force at all when the active solution requires a force that cannot be generated by a damper. In practice this means that the ER-damper is switched to the lowest setting possible.

In a broad, simplified sense, improvement in ride comfort can be obtained simply by softening the suspension. On the one side, the suspension spring can be softened; on the other hand the suspension damper can be altered in such a way that the sprung mass accelerations are reduced. But these steps must be taking within the constraints of

package space and adequate motion control. Semiactive control provides a good means to do this.

The starting-point of semiactive suspension control is active damping based on an ideal actuator, situated between sprung and unsprung mass with actuator force to be specified. The theory of linear quadratic Gaussian (LQG) control has been applied by many authors to determine a state feedback controller for active suspension systems. The LQG theory is based on the minimization of a quadratic performance index. The performance of a quarter-car suspension system can roughly be assessed quantitatively in terms of ride comfort (sprung mass accelerations), road holding (variations of the vertical tire load) and suspension working space. These three criteria can be used to setup a quadratic performance criterion. The relative importance of the different performance parameters can be expressed by weighting factors. After having chosen the weighting factors, the optimal control algorithm will select a state feedback gain matrix such that the quadratic cost function is minimized. This feedback can either be a full state feedback or a partial state feedback. The full state feedback considers all the states of the system (such as displacements and velocities of sprung and unsprung masses) and uses this information to compose an active suspension force applied between axle and vehicle body. On the other hand the limited state feedback looks only at particular states (such as the sprung mass velocity). The limited state feedback is favorable because fewer states have to be measured when the controller is implemented in a real vehicle. Venhovens (1993) has shown that the performance of limited state feedback systems in terms of gain in ride comfort is almost equal for both types of feedback.

The ultimate way to reduce sprung mass accelerations is to apply an actuator force F_{act} which is merely proportional to the sprung mass absolute velocity $\dot{z}_b$ according to

$$F_{act} = k_{sky}\dot{z}_b \tag{1}$$

where k_{sky} represents the so-called skyhook damping constant. Since only the sprung mass absolute vertical velocity is used in equation (1), this type of feedback is an example of limited state feedback. The active skyhook configuration, together with a real skyhook system and a semiactive damper system with skyhook control are shown in figure 2.

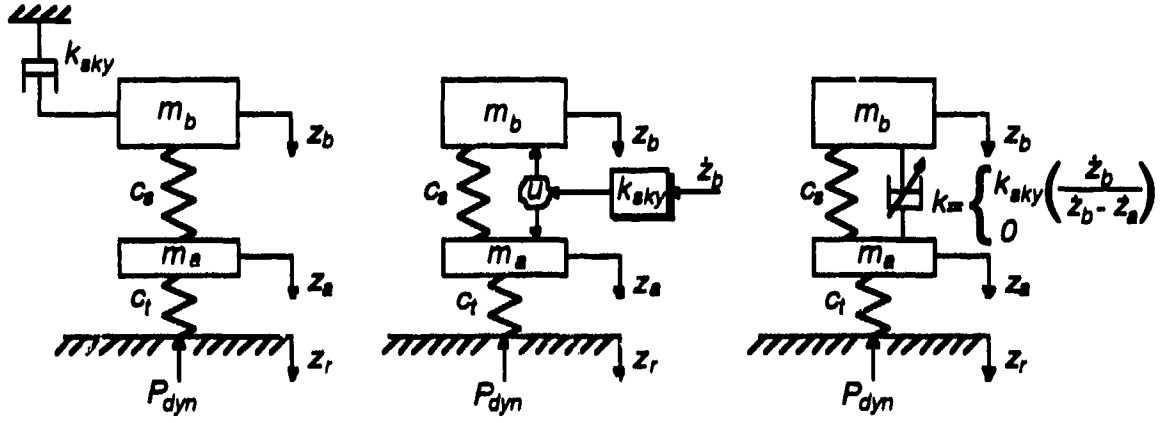

Figure 2. Skyhook control, from active to semiactive

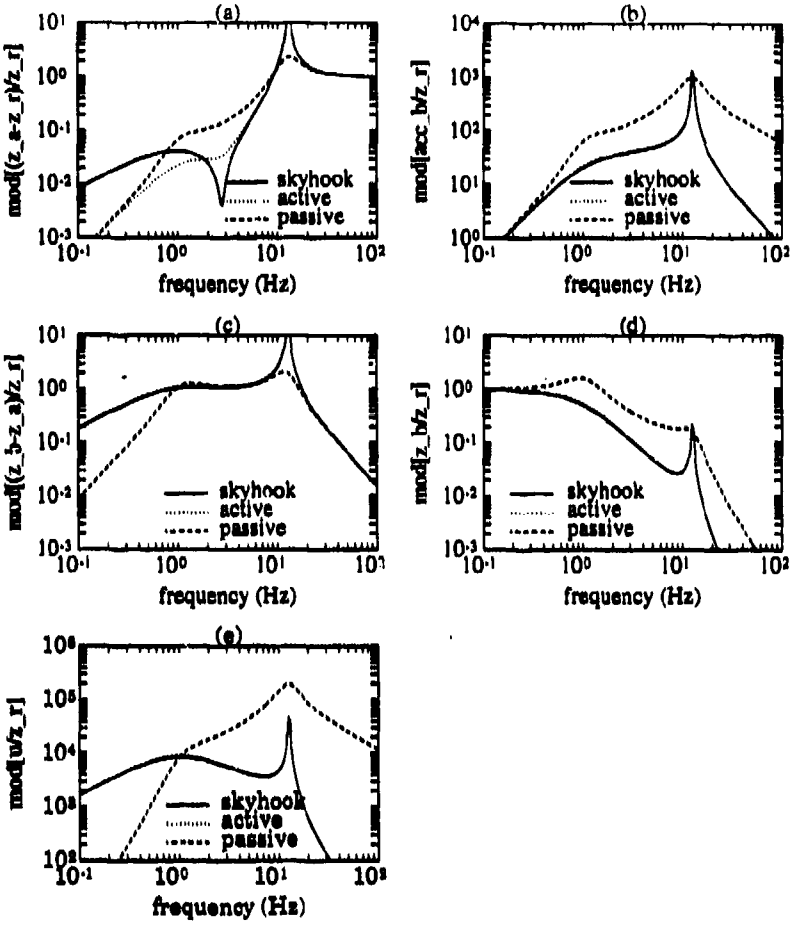

Figure 3. Frequency response functions of three suspension systems
(a) tire deflection (b) sprung mass acceleration
(c) suspension working space (d) sprung mass displacement
(e) actuator/damper force

Although there is a substantial difference between a real skyhook system and the active counterpart (the actively generated force acts on both sprung and unsprung mass; the real skyhook damper force acts only on the sprung mass), the frequency response functions of both systems show great correspondences. The five response functions of interest are plotted in figure 3.

The modulus of the tire-deflection transfer function (figure 3) of the active system with skyhook control differs from the curve valid for a real skyhook system. The reason is the point of action of the damper/actuator force. Not totally unexpected is the presence of a huge resonance peak nearby 12.6 hz (unsprung mass natural frequency). Since the motion of the unsprung mass is not damped properly in case of the skyhook damper or active system with skyhook control, a resonance peak is the result.

A small but not insignificant difference is the height of the resonance peak. In case of the true skyhook system the wheel-hop mode is not damped at all, resulting in an infinite modulus at that specific frequency. The active system with skyhook control however has

a bounded finite amplitude. Although small, the sprung mass velocity is not equal to zero near the wheel-hop natural frequency. This, combined with the fact that the actuator force depends solely on the sprung mass velocity, and that this force acts on both sprung and unsprung masses, results in a finite modulus.

With exception of the area near the unsprung-mass natural frequency, both skyhook versions (true one and active approximation) offer a large improvement in vibration isolation (graph b) over the entire frequency range compared with the passive system with a fixed suspension damping. Anticipating the test result of the quarter-car model with ER-damper, an improvement in ride comfort and low frequent tire load variations is to be expected at the cost of a degradation of tire load variations in the range of the wheel-hop natural frequency.

Generic Design Options and Parameters for the ER Damper

In approaching the design of an ER-based, semiactive suspension control, the ER component can be built as either a flow-mode (figure 4a), mixed-mode (figure 4b), or shear-mode (figure 4c) type of damper. The configurations illustrated in figure 4 are essentially generic concepts that contain simplified features to facilitate the design analysis. In practical hardware, for example, the cylinder is likely to be single-ended, rather than double-ended, and the ER control valve or area is likely to be comprised of multiple parallel or concentric plates. Among the three conceptual modes, the flow-mode damper is most similar to the traditional shock absorber except that it replaces the conventional orifice with an ER control gap or valve. The source of the damping force in this mode is exclusively from flow-induced pressure drop across the piston. The ER valve can be placed outside the cylinder (as in figure 4a) or within the piston component. For the sake of compact packaging, the external approach could be implemented by forming a flow chamber along the outside of the cylinder wall (Petek, 1992).

In the mixed-mode damper, the ER control is realized in the gap between the piston side-wall and the cylinder liner. The fluid shear stress at the shear surface also contributes to the damping force, while the flow-induced pressure drop is still present as a force component on the piston.

If a large by-pass port is cut through the piston of a mixed-mode damper, the device becomes a simple shear-mode element. Since the fluid can flow freely through the by-pass, the pressure drop across the piston becomes negligible and only shear stresses developed along the wall contribute to the damping force.

Our analysis (see appendix A) indicates that the shear-mode damper achieves better dynamic response and more effective control than the flow- or mixed-mode types. Because certain principles in ER design support the prospect of a package that is mechanically simple, durable, low in cost, and exhibits a broad bandwidth, it appears that an ER semiactive suspension may be superior to conventional types of semiactive and active suspensions for automotive applications. Although the fluid's behavior is complex, it has also been sufficiently well defined at this point that its codification on cheap and reliable memory devices is straightforward. Improvement in mechanical strength of the

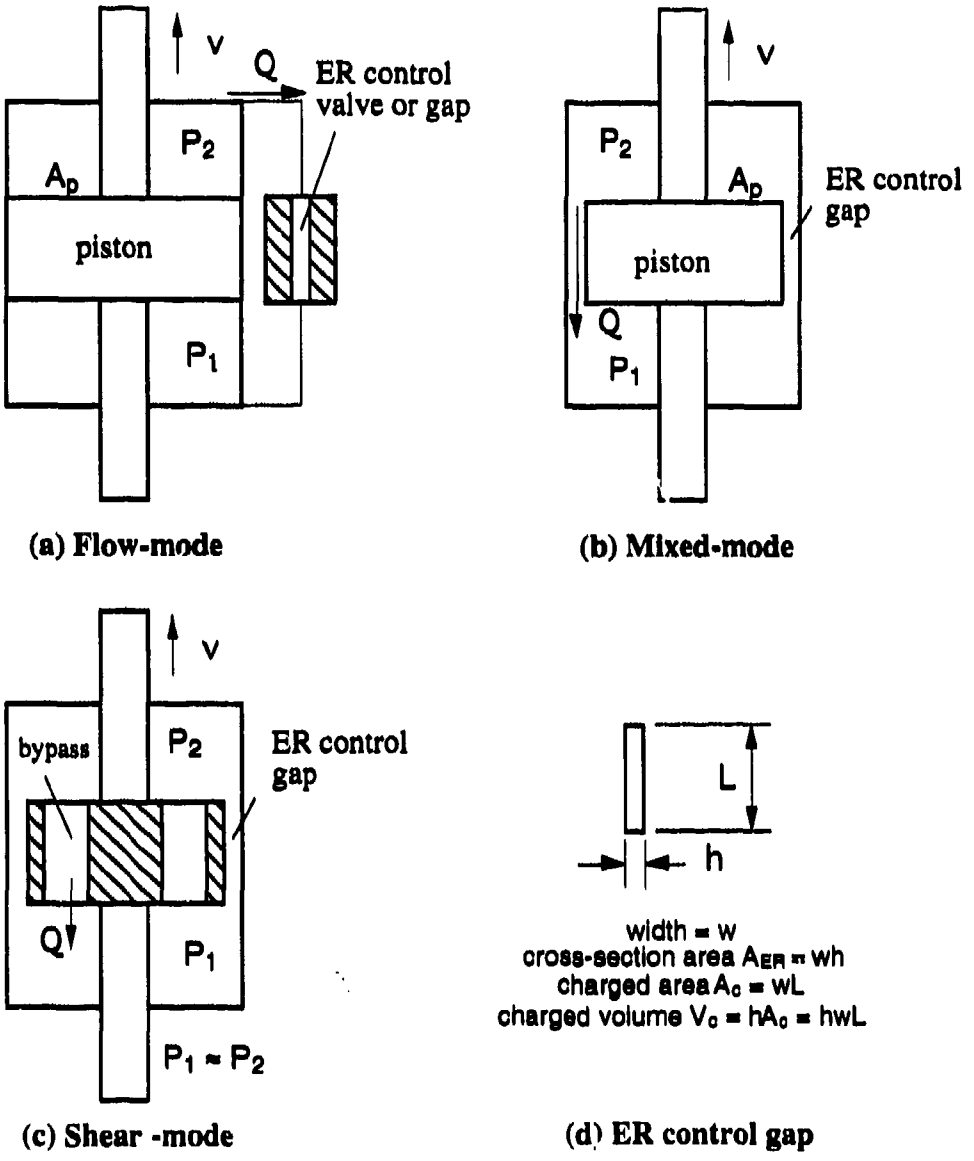

Figure 4. The generic concepts of the three modes of electrorheological dampers

fluid's energized, shear-stress response remains the most important factor in determining whether or not ER devices will become practical in this application.

Selected Design of the ER Shock Absorber

A shear-mode damper, as indicated in the above section, achieves better dynamic response and more effective control than the flow- or mixed-mode types and is thus selected as the damper mode for this project. The general concept of the proposed design is shown in figure 5. The control in the ER damper is realized through a medium of an ER fluid. The shear-mode damper uses, instead of translational plates, a plurality of rotational shearing disks (hot electrodes and cold electrodes), which form a total control

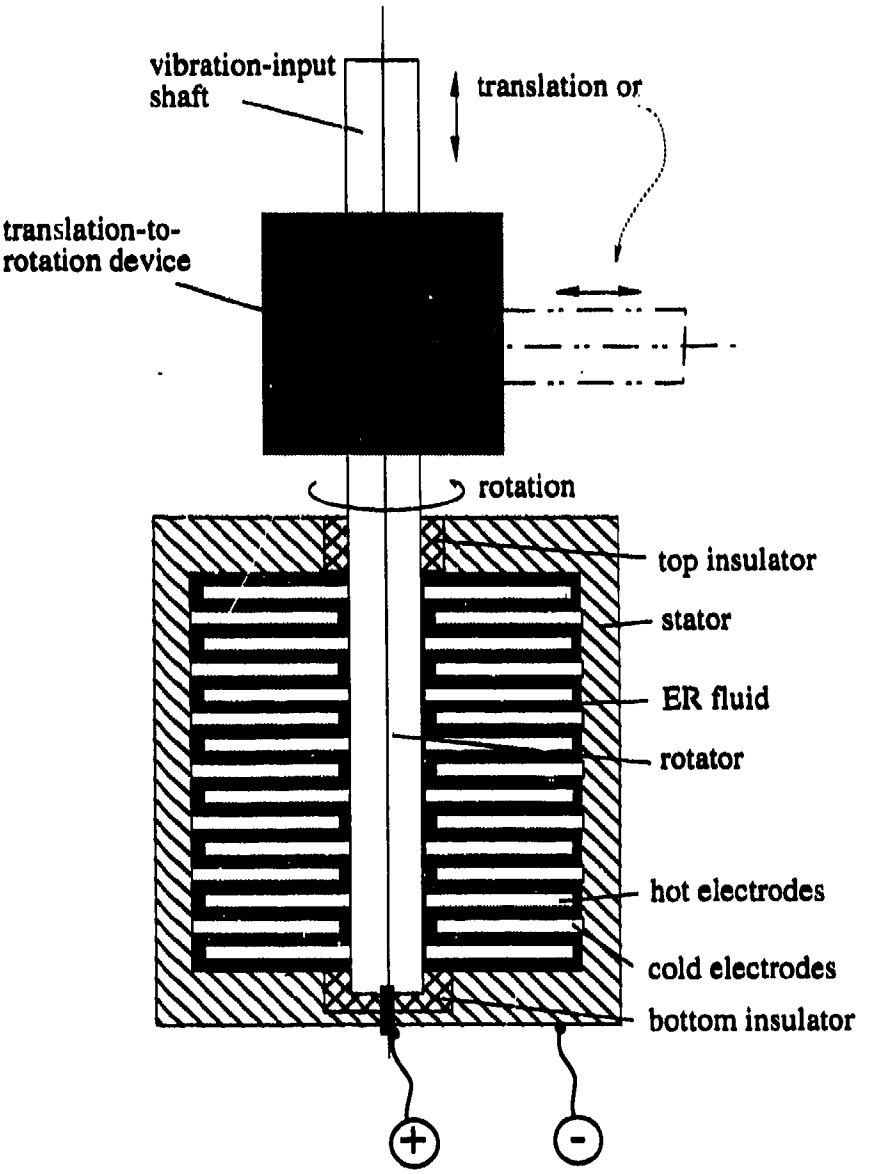

Figure 5. The general concept of the proposed design

(or shearing) surface area that is constant and independent of the relative position of the actuator, resulting in a good control and a compact size. A translation-to-rotation device converts the translational motion of the vehicle vibration into the rotational motion of the shear-mode damper, and vice versa.

The actual ER damper developed in this project is show in figure 6. The specific design of this device is illustrated in figure 7. In this design, thirty-nine ground electrodes, separated from each other by spacers, are mechanically fixed and electrically connected to a stator through stator feather keys. The stator is grounded electrically and fixed rigidly onto the unsprung mass. Forty elevated-voltage, or "hot," electrodes, also

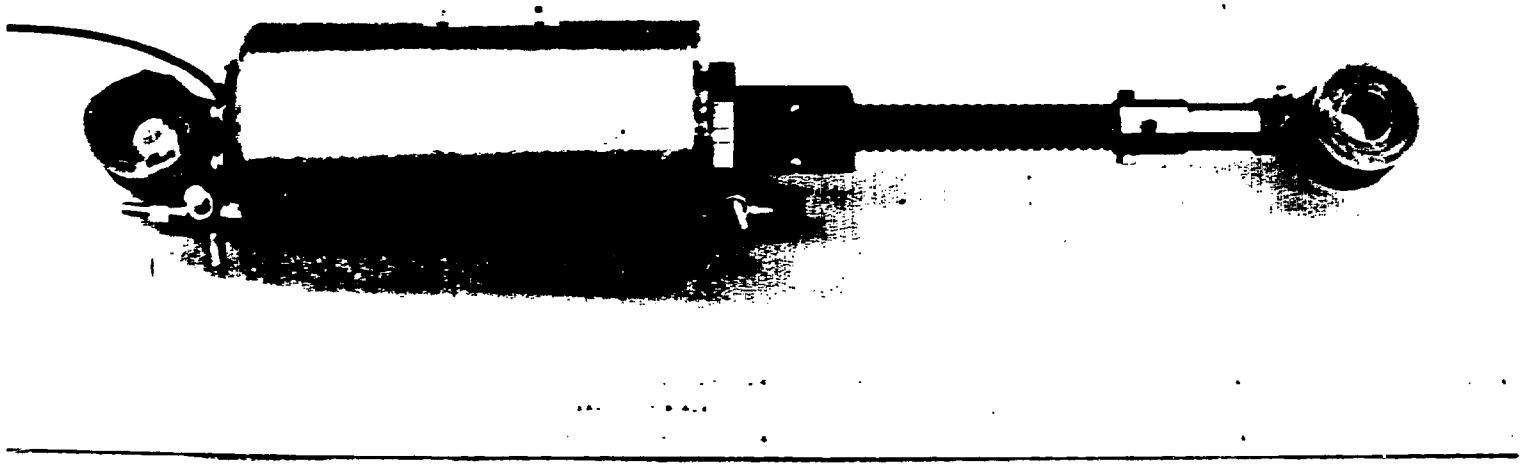

Figure 6. The ER damper developed for the HMMWV

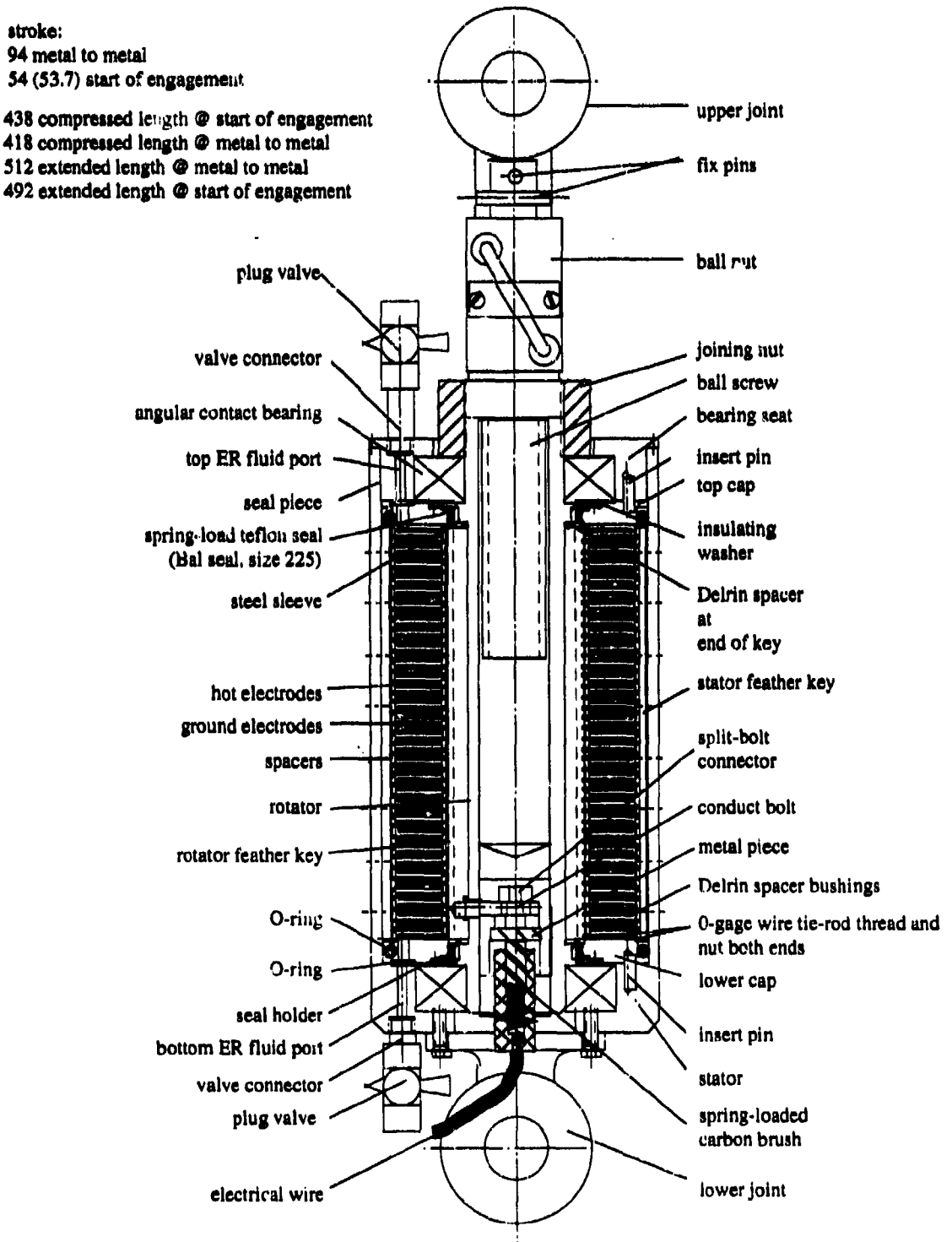

Figure 7. Assembly of the ER damper

separated from each other by spacers, are mechanically attached to a rotator through rotator feather keys, and electrically connected to the high voltage through a spring-loaded carbon brush. The rotator is mechanically supported by top and bottom bearings that can sustain both radial and axial loads. The rotator is made from glass epoxy G-11, a dielectric material with high mechanical strength. Interelectrode gaps are filled with an ER fluid through top and bottom ports.

The translational relative motion is converted through a ball screw mechanism, which is tightly connected on top of the rotator with a joining nut. The use of the ball screw renders smooth power and motion transmission. The elevated voltage can be supplied to the rotator through a carbon brush at the bottom instead of the fixed connection at the top as shown in figure 5. The complete set of drawings of the ER damper is contained in appendix B.

Target Parameters for ER Shock of TACOM

A conventional, rear suspension system of the HMMWV is illustrated in figure 8. A shock absorber, made by the Monroe Auto Equipment Company, is mounted inside a coil spring. To make minimum changes to the existing suspension system, the ER damper is also situated inside the mechanical spring, and its outer diameter is therefore limited by the inner diameter of the spring, which varies between 11.5 cm (near the bottom seat of the spring) and 12.6 cm along the axis. The selection of the outer diameter of the ER damper (equal to the outer diameter of the stator) is further influenced by the spring buckling and some misalignment between the spring and shock center lines. The outer diameter of the Monroe shock is 6.985 cm (2.75 in). For a quarter-HMMWV, the sprung and unsprung masses are 803 kg (1769 lbs) and 98 kg (217 lbs), respectively. The suspension spring stiffness measured at the wheel spindle is 63,528 N/m (4,356 lbs/ft or

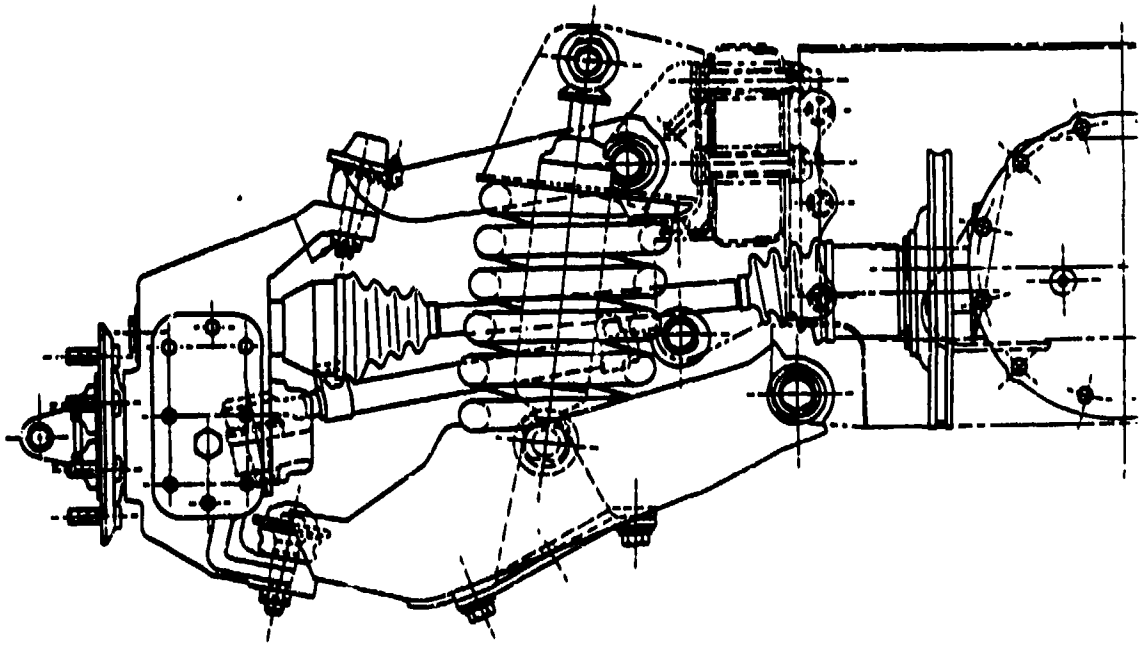

Figure 8. The conventional rear suspension system of an HMMWV

363 lbs/in). The tire spring stiffness is 204,394 N/m (14,015 lbs/ft). The vehicle heave natural frequency is 1.3 hz, while the wheelhop frequency is 7.9 hz. The vehicle pitch natural frequency is 1.8 hz, which is ignored here because only a quarter car model is considered.

The metal-to-metal length of the Monroe shock is 32.72 - 32.11 to 42.16 - 41.55 cm (12.88 - 12.64 to 16.60 -16.36 in), and the metal-to-metal stroke is 9.4488 cm (3.72 in). The overall stroke is 5.3 cm (2.1 in). The length of the body of the shock absorber is about 21.3 cm (8.38 in). Because of the geometric layout, the displacement and force at the wheel centerplane (X_{wheel} and F_{wheel}) are related to those at the shock absorber (X_{shock} and F_{shock}) approximately in the following way:

$$X_{shock} = 0.48\, X_{wheel} \tag{2}$$

$$F_{shock} = 2.08\, F_{wheel} \tag{3}$$

A conventional shock has bilinear characteristics. It offers more damping during extension than during compression. Also, the shock has a pressure relief feature which limits the damping force to a maximum value when the relative velocity creates a certain relief pressure. Some of the base data are presented in table 1. Relief velocities and limit damping forces at the wheel spindle were taken directly from the vehicle test data sheet from TACOM. Using the above two equations, the spindle velocities and forces were extrapolated to the shock velocities and forces, which do not always agree with the shock data provided by Monroe. Also damping forces are far from linear within the limit velocities and, thus, their corresponding damping coefficients are not constant. Their simple arithmetic average values were calculated. Damping ratios were also calculated, using the sprung mass, the spring constant, and the average damping coefficients. As expected, the damping ratio for extension (= 0.74) is higher than the damping ratio for compression (= 0.25).

Based on the above data, we chose 15,000 N (3,374 lbf) as the target design damping force in the ER damper.

Number of Electrode Plates

The influence of the inertia force is small in a shear-mode damper, such that the damping force in the strut can be approximated with a Newtonian damping force (F_{dN}) and an ER damping force (F_{dER}), corresponding to the effects of the plastic viscosity (η) and the yield shear stress (τ_y), respectively, in the Bingham model. The two damping forces are derived as

$$F_{dN} = \frac{4\pi n\eta(r_o^4 - r_i^4)}{ehD_p^2\tan^2\lambda}\,\Delta v \tag{4}$$

and

$$F_{dER} = \frac{\Delta v}{|\Delta v|}\,\frac{8\pi n(r_o^3 - r_i^3)}{3eD_p\tan\lambda}\,\tau_y \tag{5}$$

with

Table 1. Basic parameters of the HMMWV shock absorbers

	Compression		*Extension*	
	At the wheel	*At the shock*	*At the wheel*	*At the shock*
Relief velocity	0.76 m/s 2.48 ft/s	0.36 m/s .19 ft/s	0.76 m/s 2.48 ft/s	0.36 m/s 1.19 ft/s
Limit damping force at and beyond relief velocity	2,667 N 600 lbf	5,547 N 1,248 lbf	8,001 N 1,800 lbf	16,643 N 3,744 lbf
Damping coefficient range	2,348 to 4,696 N s/m 161 to 322 lbf s/ft		10,209 to 10,923 N s/m 700 to 749 lbf s/ft	
Average damping coefficient	3,522 N s/m 242 lbf s/ft		10,566 N s/m 725 lbf s/ft	
Average damping	0.25		0.74	
Monroe shock limit damping force and velocity		1,190 - 714 lbf at 1.11 ft/s		2,608 -1,564 lbf at 1.11 ft/s

$$\Delta v = \frac{dx_U}{dt} - \frac{dx_S}{dt} \tag{6}$$

$$e = \frac{\cos\phi - \frac{f}{\tan\lambda}}{f\tan\lambda + \cos\phi} \tag{7}$$

where n is the number of hot electrodes, h (= 0.001 m) the gap size between the electrodes, t the time, Δv the strut deflection velocity, x_S the sprung mass displacement, x_U the unsprung mass displacement, r_o (= 0.0483 m) and r_i (= 0.0285 m) the outer and inner radii of the effective shearing surface of the electrodes, respectively. The parameter D_p (= 0.0254 m) is the pitch diameter, ϕ (standard at 29 degrees) the thread angle , λ (= 17.657 degrees) the lead angle, e (= 90 percent) the ball screw efficiency, and f (= .033) the friction coefficient for the screw-nut mechanism. The variables v_S and v_U are the sprung and unsprung mass velocities, respectively, and Δv is the strut deflection velocity. The Newtonian and ER damping forces here are completely uncoupled and additive. While this approach provides only a first-order estimation, it is convenient and insightful for a preliminary parametric study. However, a complete solution of the problem will demand a full solution of the fluid flow problem (Lou *et al.*, 1993).

If F_{dER} alone is to reach 15,000 N and if τ_y = 6,895 Pa (1 psi), n must be 21 according to equation (6). If τ_y = 0.5 psi, then, n = 42. In the current design, 40 hot electrodes are chosen.

Damping torque on the rotator T_d is related to the damping force (F_d) as follows

$$T_d = e\frac{D_p}{2}\tan \lambda F_d \tag{8}$$

where $F_d = 15{,}000$ N, $T_d = 54.57$ N-m.

Material of the Rotator

The material used for the rotator must satisfy both mechanical and electrical constraints. The maximum shear stress is

$$S_v = \frac{16T_dD}{\pi(D^4 - d^4)} \tag{9}$$

where D and d are the outer and inner diameters of the rotator, respectively. In this design, D = 39.7 mm and d = 27.99 mm. Therefore,

$$S_v = 5.9 \times 10^6 \text{ N/m}^2 \tag{10}$$

The peak intensity of the electric field requires that the rotator be able to withstand an 8 kv/mm field condition. To satisfy the combined requirements, a glass epoxy G-11 was selected. This material provides a shear strength of 1.517×10^8 N/m^2 (22,000 psi) and an electric strength of 35.4 kV/mm (900 V/mil).

Rotator Feather Key

According to moment balance,

$$T_d = r_k \sigma t_d t_k n_k n \tag{11}$$

where n_k is inner radius of the hot electrode plate (= 1.877 in = 0.0477 m); s, shear stress, t_d, the hot electrode plate thickness (= 0.001 m); t_k, the depth of the rotator key (= 0.197 in = 0.005); n_k, the number of the keys (= 2). The maximum imposed torque results in a shear stress on the key of:

$$\sigma = T_d/r_k t_d t_k n_k n = 2.86 \times 10^6 \text{ N/m}^2 \tag{12}$$

Stator Feather Key

Each stator key is fixed by eight screws for easy manufacturing. Each screw will bear a shear stresses according to the relationship:

$$T_d = 8r_s\sigma_s n_s \pi d_s^2/4 \tag{13}$$

where r_s is the outer radius of the ground electrode plate (= 4.13 in = 0.105 m); n_s, the number of the stator keys (= 2); d_s, the screw diameter (= 0.112 in = 0.00284 m). The maximum shear stress on each stator key, σ_s, is calculated to be 5.39×10^6 N/m^2, which is smaller than the allowed stress of 35×10^6 N/m^2.

Filling the Damper with ER Fluid

In order to avoid arcing when high voltages are applied across the plates of the damper, it is important to insure that little or no air is entrained in the ER fluid. Therefore, a special effort was undertaken to fill the damper with fluid.

The fluid sample was first put into a closed vessel and subjected to a 29-in hg. vacuum for a period of twenty-four hours. Still under a vacuum, the fluid was agitated to insure an even distribution of the particulate material. The fluid was then immediately forced into the damper under three to five psi pressure. In this process, the fluid was withdrawn from the bottom of the external vessel and fed into the damper through its bottom port so that air was not drawn into the system. Air was simultaneously evacuated from the damper through the top port.

In all of the subsequent operations of the damper, the internal fluid space of the damper was plumbed to a small bladder-accumulator containing the same ER fluid. By this means, ER fluid was maintained at about three psi gage pressure. Thus, the fluid in the damper was maintained at a positive pressure, preventing air ingestion through the seals of the damper while permitting expansion and contraction with heating and cooling.

Whenever the damper was not active, the sealed system of damper and external accumulator was removed from the testing apparatus and placed in a tumbler in order to prevent settling of the particulates in the ER fluid. (The tumbler was simply a tube lined with foam padding, turning slowly in a lathe.)

6. Testing the ER Fluid Damper

Three types of tests were conducted on the semiactive ER damper developed by UMTRI. The initial tests involved a very simple series of static measurements to quantify the force-to-voltage behavior of the new damper. These tests were followed by two series of more sophisticated dynamics tests. In one, the damper was tested alone in order to verify its basic properties. The third, more elaborate set of tests was conducted with the damper installed in a quarter-HMMWV dynamic test facility. These tests measured the ride isolation properties of the HMMWV suspension using both the semiactive ER damper and the conventional damper normally used in the HMMWV suspension.

This chapter is divided into four sections which cover (1) the static test series, (2) the dynamic test facility, (3) dynamic tests of the damper alone, and (4) the quarter-HMMWV series of tests.

Static Tests of the ER Damper

The static tests were done simply to measure the relationship between applied control voltage and the static force developed by the damper. As noted previously, the primary quality of the shear-mode type of damper is that it produces a force in response to control voltage (i.e., the Bingham shear response) but is rather insensitive to stroke velocity (i.e., the viscous shear response). It follows that a static characterization of the control voltage-to-force relationship of the device can serve as a primary description of the behavior of the device.

The static tests were very simple. The body of the damper was fixed on the test bench and a control voltage was applied. A torque wrench was then used to rotate the ball-screw nut. The measured torque was converted to an equivalent force for the ball-screw assuming one hundred percent mechanical efficiency. The process was repeated at several voltages.

The results of two repeats of this simple test are shown in figure 9. Two characteristics of this plot are significant. Firstly, the damper exhibits a coulomb friction response of about 50 pounds force with no voltage applied. This force derives exclusively from the rotational friction of the fluid seals amplified by the mechanical gain of the ball-screw hardware. Secondly, the force response of the system is approximately proportional to the 2.5 power of the applied voltage. This is similar to previous observations of the behavior of ER fluid systems (Lou, 1990).

The data of figure 9 have been fitted with two curves. One curve is a quite good fit which reflects the coulomb friction quality of the system as well as the voltage response. The second is a poorer fit in that it ignores the friction response and approximates only the voltage response. (That is, this curve passes through the origin of the plot.) This latter function was used as a basis for the semiactive control algorithm in the quarter-HMMWV test series.

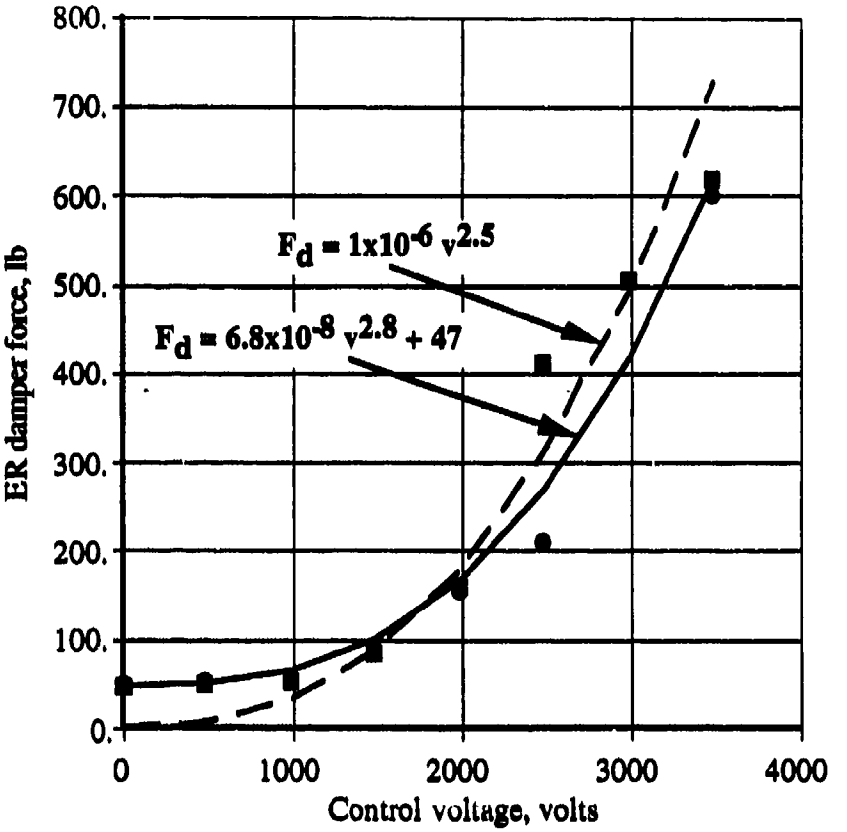

Figure 9. The static response of the ER damper

The Dynamic Test Facility

In order to conduct in situ dynamic tests of the ER damper as a semiactive shock absorber, UMTRI constructed a quarter-HMMWV dynamic road simulator facility. TACOM provided the necessary HMMWV suspension and frame components. These, along with the necessary supports, instrumentation, and electrohydraulic servo road surface exciter, made up the quarter-HMMWV road simulator. The facility was used to measure the ride response of the quarter-HMMWV to road profiles provided by TACOM. Test were conducted with the standard damper used on the HMMWV as well as with the ER damper.

In addition to using this equipment for full scale quarter-HMMWV tests, a subset of the servo actuator and instrument systems were used for a small series of dynamic tests on the ER damper alone. The servo actuator was used to stroke the damper in a controlled manner. Tests were conducted to determine the response of the damper to stroke velocity and to step changes in control voltage.

The remainder of this section will describe the dynamic test facility. The dynamic tests themselves will be discussed in sections to follow.

The Mechanical Facility

The quarter-HMMWV road simulator facility is pictured in figure 10. Figure 11 is a sketch of the facility in which many of the items mentioned in the following discussion are labeled for the reader's convenience.

The facility is based on a small bed plate. Two pairs of channel-section uprights are mounted on the plate. The shorter pair, immediately fore and aft of the HMMWV tire, support the vertical linear bearings, which guide the motion of the simulated road surface. The taller pair of uprights support the vertical guide bearings for the motion of the vehicle sprung mass.

This "vehicle" is one rear quarter of an HMMWV. The tire, wheel, hub, and suspension members (except for the modified shock bracket) are all standard HMMWV parts. The suspension is attached to a shortened HMMWV frame rail and standard frame cross members. (All the standard HMMWV parts in figure 10 are painted black.) A gray colored ballast frame is mounted on the standard frame members. This frame supports three 500-pound iron blocks, bringing the total mass of the quarter-HMMWV to 2,490 pounds, thus simulating a fully loaded HMMWV. Note that the ballast iron is mounted directly above the tire. This helps locate the center of gravity of the simulated vehicle closer to the wheel plane, greatly reducing the overturning moment applied to the linear bearings, which provide the vertical guidance for the sprung mass.

The dynamic road simulator is located beneath the HMMWV tire. The road surface plate is mounted on linear bearings, which accommodate the lateral motion of the HMMWV tire. (Because of compromises forced by ground clearance requirements, the HMMWV suspension geometry produces an unusual amount of lateral motion of the tire when the suspension deflects vertically.) These bearings sit on an intermediate plate, which is guided by the vertical linear bearings mentioned previously.

Vertical support for the road is provided by three cylinders. The outer two are air cylinders, which provide support for the static load of the system. The center cylinder is an hydraulic servo actuator, which provides the dynamic component of the road force. All three cylinders are mounted atop an air manifold.

The air cylinders are plumbed to the air manifold through a large (2-in diameter) hole bored directly down through the cylinder tail block and on into the air manifold. In turn, the manifold is plumbed through a short 2-in pipe to a large air tank. The tank is supplied with pressure-regulated air. This large volume, low-flow-resistance system results in the air cylinders providing a virtually constant force to the road even during large and rapid road motions. The air pressure is adjusted so that this static force is approximately equal to the weight of the quarter-HMMWV.

Because of the air system support, the hydraulic actuator need supply only the dynamic portion of the road forces. Relieving the servo of the static support substantially reduces the *power* requirements of the servo system, allowing higher performance with smaller, less expensive components. The 2-1/2-in diameter hydraulic cylinder was supplied through a pair of parallel plumbed 10-gpm MTS 252-series servo valves. (These are actually modified Moog 76-series valves.) Hydraulic power was provided by

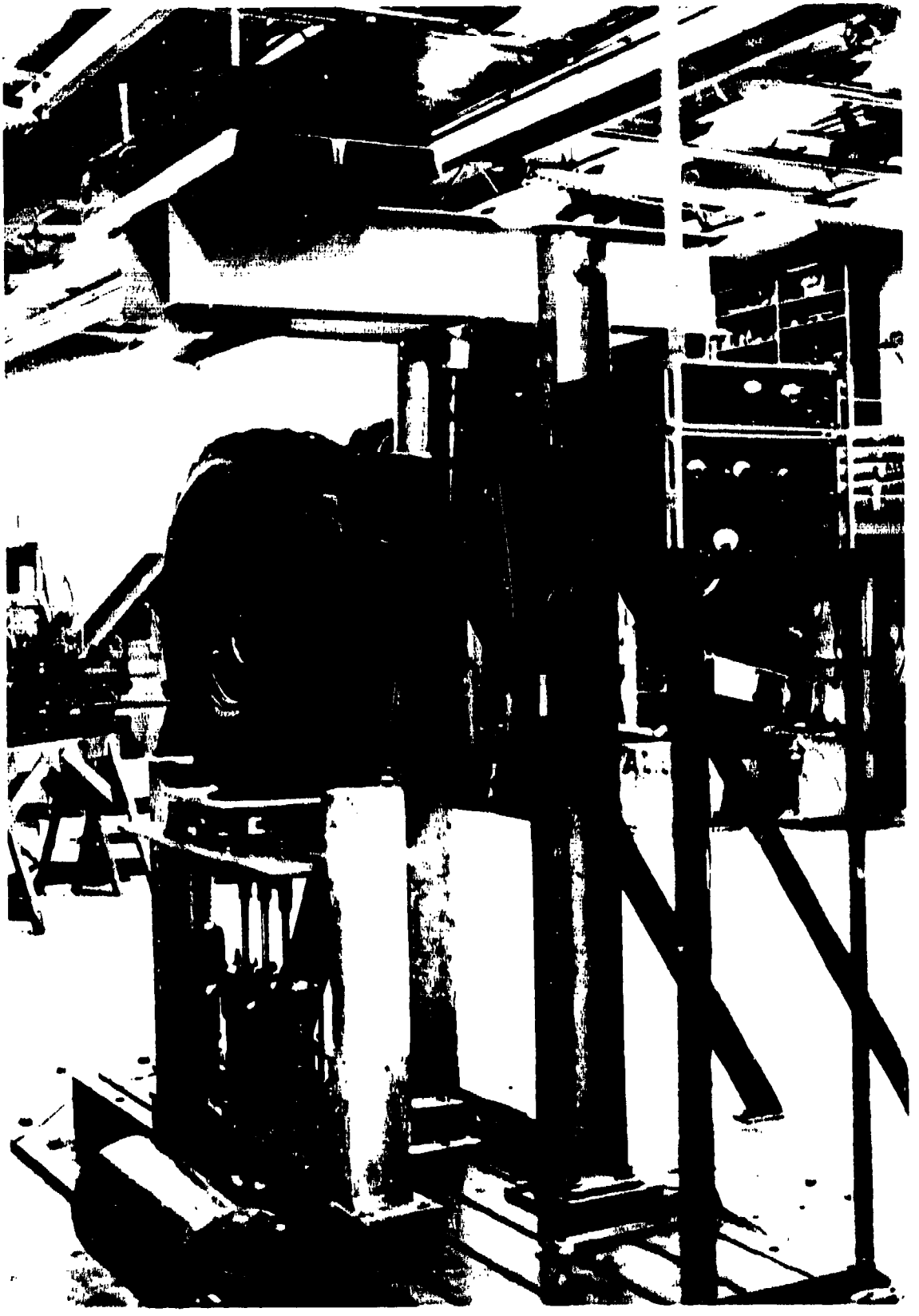

Figure 10. Photograph of the dynamic test facility

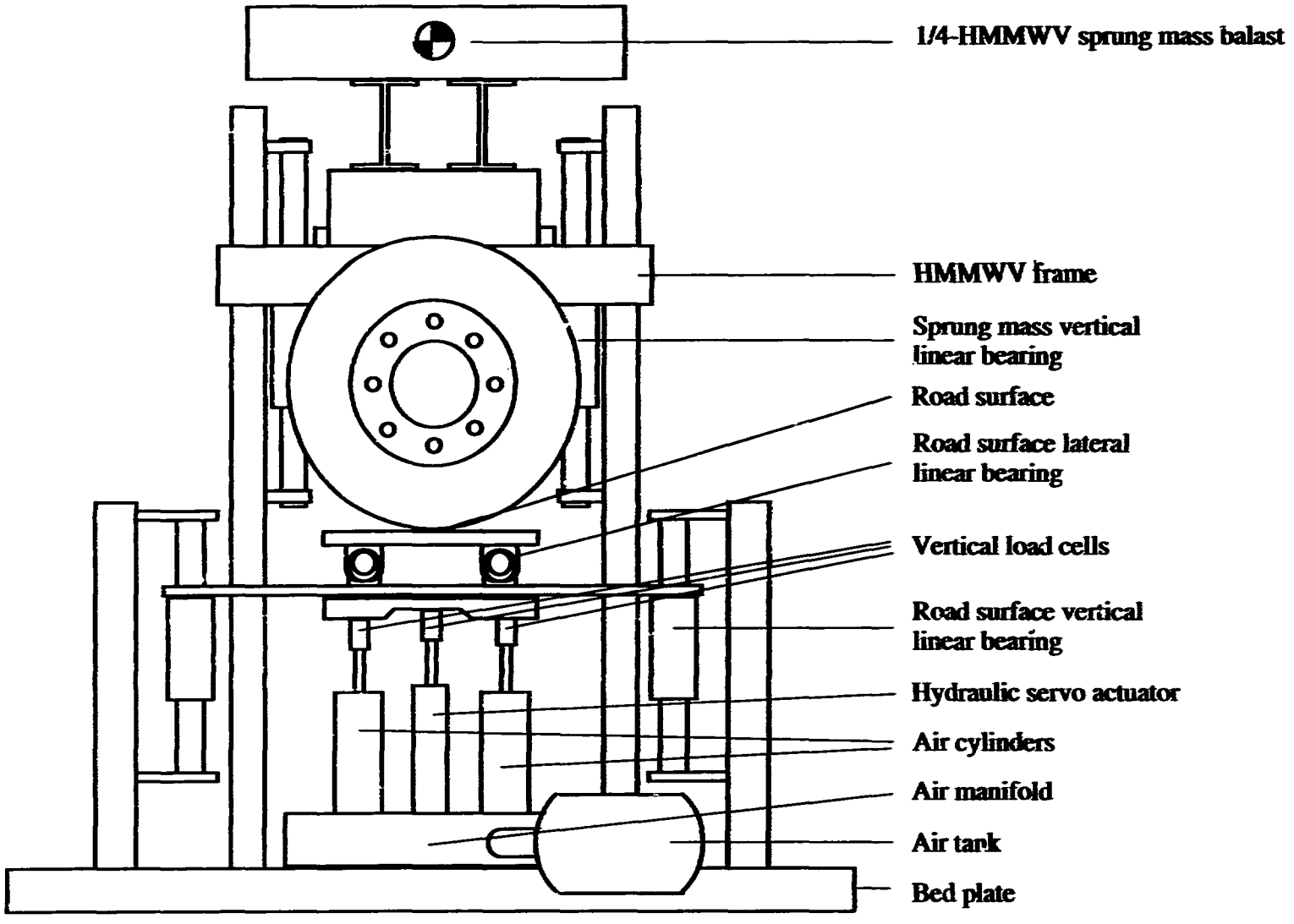

Figure 11. Sketch of the quarter-HMMWV road simulator

a 10-gpm, 3000 psi supply augmented with a 1-1/4-gallon supply accumulator. These components formed a system whose small displacement response was flat to approximately 40 hz. A maximum velocity of 20 in/sec was attainable within the accumulator reserve. Sustainable mean velocity, established by pump rate , was about 18 in/sec.

Instrumentation and Control

Figure 12 presents a block diagram of the instrumentation and control electronics of the quarter-HMMWV road simulator. The system provides for the three basic functions of (1) ER damper control, (2) data acquisition, and (3) road actuator control. The heart of the system was a Macintosh Quadra 800 computer coupled to UMTRI's Engineering Research Division (ERD) data acquisition system. This basic system was augmented with a high-voltage amplifier for generating the kilovolt-level signal required for damper control, high-voltage signal isolators for protecting the computer circuits in case of arcing, a servo amplifier, thermocouple amplifier, and an array of appropriate sensors. Details of these elements, in the context of the three basic functions, are presented in the following three subsections.

ER Fluid Damper Control

The computer controller of the quarter-HMMWV simulator determined the electrical voltage sent to the ER damper. This voltage command (v_c) was recalculated and updated 100 times per second. The calculated command was output by the computer through a high-voltage isolator into a high-voltage amplifier. (See the next section for a discussion of these two elements.) The actual voltage signal (v) — up to 3000 volts — was supplied to the ER damper by this amplifier.

In concept, any of the forces or motions transduced by the many instruments of the simulator could be used by the computer to calculate the desired ER damper voltage. In these tests, only two velocity signals were actually used. These were the absolute vertical velocity of the sprung mass (V_S) and the relative velocity of the sprung and unsprung masses ($V_{(S-U)}$), that is, the damper stroke velocity. These velocities were used in two control algorithms, one which caused the ER damper to behave as a *skyhook damper* and one which caused it to behave as a *conventional shock absorber*.

The skyhook damper was discussed in chapter 5 of this document. To briefly review: The concept is one of a linear damper connected between the sprung mass of the vehicle and an imaginary hook in the sky whose vertical velocity is defined to be zero. Thus, the damping forces are proportional only to the absolute vertical velocity of the sprung mass, not to the relative velocity of the sprung and unsprung masses as is the case with a conventional damper.

In practice, the real damper, which produces these idealized forces, is actually connected between the sprung and unsprung masses. Since the damper is passive (that is, it can produce forces only in opposition to stroke velocity), there are time periods when it is not possible for the damper to generate the desired damping forces. For example, when the sprung mass is moving upward, the desired force is downward, but the damper can apply a force downward on the sprung mass only when the *relative* velocity of the sprung

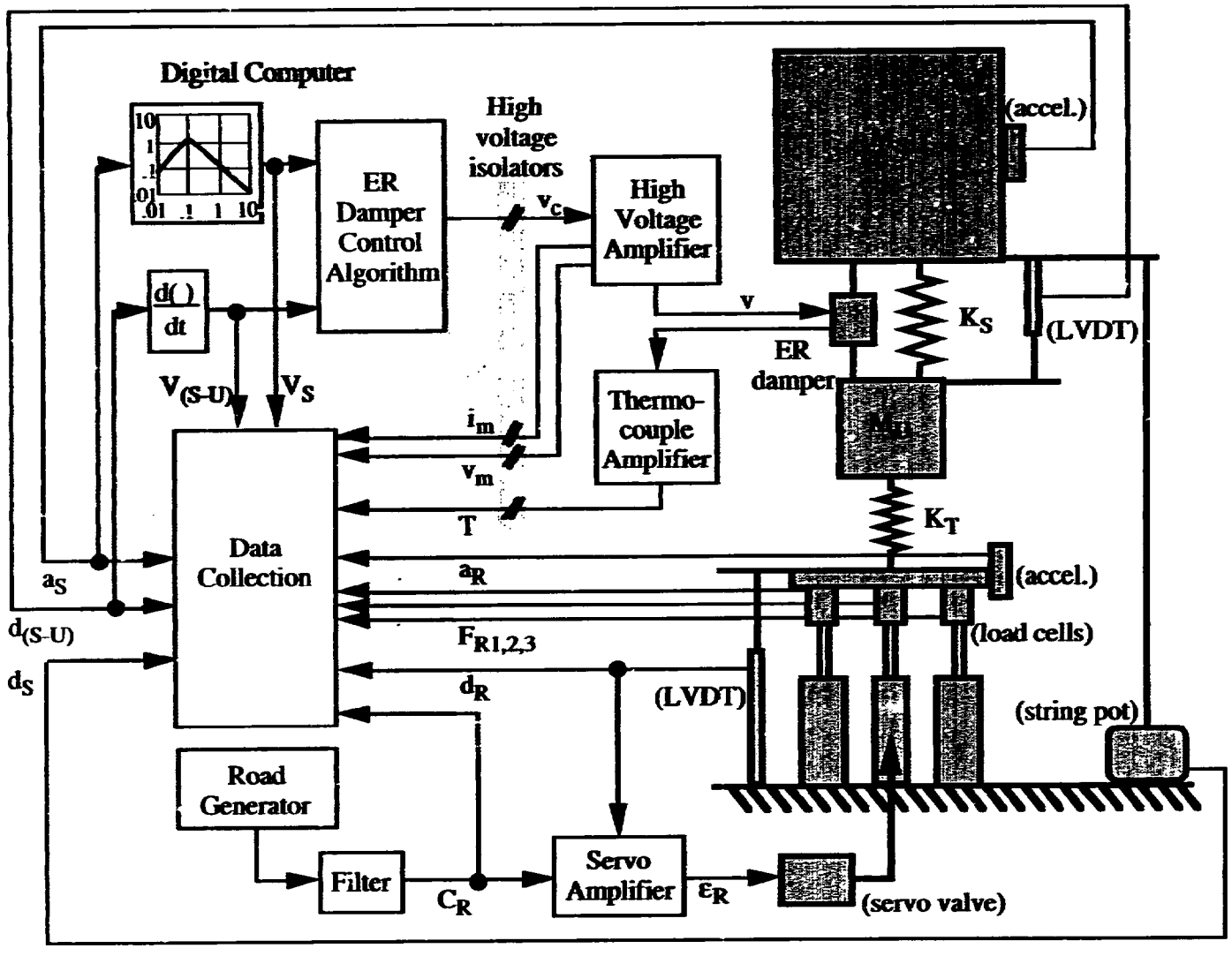

Figure 12. Block diagram of the electronic systems of the quarter-HMMWV road simulator

mass to the unsprung mass is positive (i.e., damper extending). If the unsprung mass happens to be moving upwards faster than the sprung mass, the damper can only apply forces in the wrong direction.

Thus, the damping force (F_d) desired of the ER damper is proportional to V_S whenever V_S and $V_{(S-U)}$ are of the same polarity, but this force is to be zero whenever V_S and $V_{(S-U)}$ are of opposite polarity. In equation form:

$$F_d = c_{sky} V_S \bullet [(V_S \bullet V_{(S-U)} > 0] \tag{14}$$

where c_{sky} is a constant and the logical function $[(V_S \bullet V_{(S-U)} > 0] = 1$ if TRUE and 0 if FALSE.

Equation 14 indicates the desired damping force, but not the ER-damper-command voltage. The previous discussion of the static tests of the damper showed the relationship between damper force and voltage to be:

$$|F_d| = |k_v \, v^{\beta}| \tag{15}$$

where k_v and β are both constants. Combining equations 14 and 15 and solving for the voltage leads to the following expression for the voltage command sent to the high-voltage amplifier:

$$v_c = |k \bullet V_S|^{1/\beta} \bullet [(V_S \bullet V_{(S-U)} > 0] \tag{16}$$

where k is a constant equal to c_{sky}/k_v.

Equation 16 is the skyhook control algorithm for the ER damper used in our testing. From the results of static testing, the chosen value of β was 2.5. By preliminary experimentation, $15 \times 10^6 \, v^{2.5}$ $(in/sec)^{-1}$ was chosen as the value for k.

Figure 13 is a plot of an actual voltage command time history generated by this skyhook control algorithm during a test run in which the quarter-HMMWV was excited with a 1.3 hz sinusoidal road motion. The sinusoidal-like quality of the signal is apparent as is the on/off switching function, which is based on the relative velocity.

The conventional shock absorber algorithm employed only the relative velocity $V_{(S-U)}$. This algorithm was simply a representation of the conventional bilinear behavior of automotive shock absorbers[1] with the addition of the non-linear quality of the ER damper force-to-voltage relationship.

The equations used to simulate a conventional shock were simply:

$$\begin{aligned} v_c &= |k_c \bullet V_{(S-U)}|^{1/\beta} \quad \text{when } V_{(S-U)} < 0 \\ v_c &= |k_t \bullet V_{(S-U)}|^{1/\beta} \quad \text{when } V_{(S-U)} >= 0 \end{aligned} \tag{17}$$

where k_c and k_t are constants for compression and extension, respectively. The constant values actually used in testing were $k_c = 8 \times 10^6 \, v^{2.5}$ $(in/sec)^{-1}$ and $k_t = 16 \times 10^6 \, v^{2.5}$ $(in/sec)^{-1}$.

---

[1] Conventional shock absorbers typically provide stronger resistance to extension than to compression (basically because hitting curbs can generate much higher unsprung mass velocities than falling into holes).

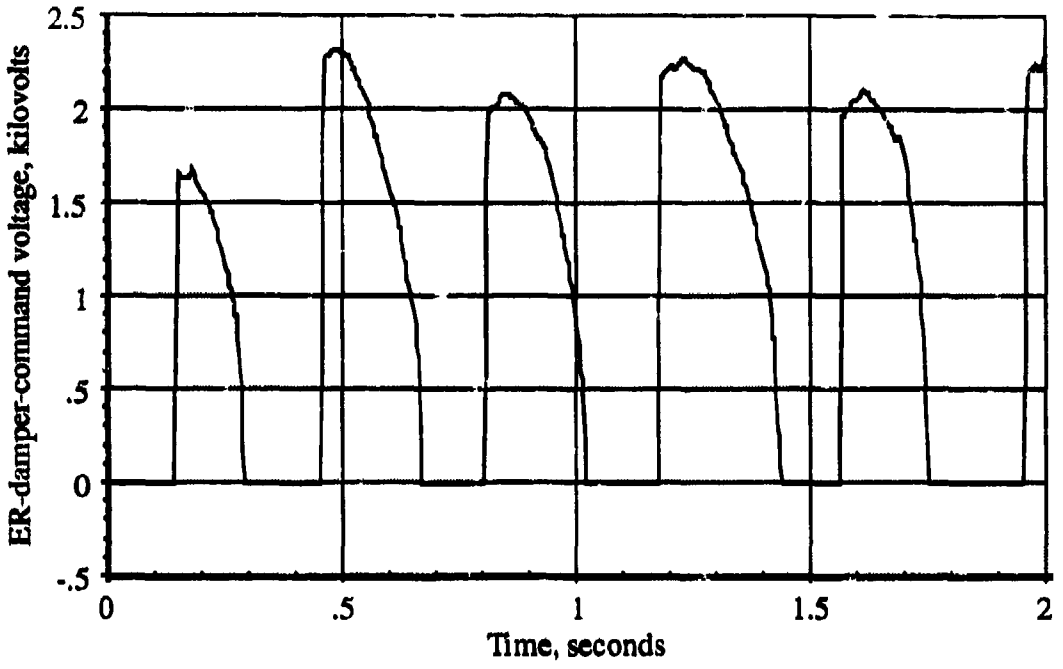

Figure 13. Voltage command to the ER damper using the skyhook algorithm

Before leaving this discussion, consider the source of the velocities used in equations 16 and 17. V_S was determined by integrating the signal provided by the accelerometer mounted on the sprung mass. (On the test rig, we could measure this velocity directly, but in the real world, integration of acceleration is the most reasonable approach.) The frequency domain transfer function shown in the block diagram of figure 12 indicates that the acceleration signal is simultaneously subjected to a high-pass filter to remove any DC component and prevent drift of the calculated velocity. To obtain $V_{(S-U)}$, the signal from a displacement transducer placed in parallel with the damper was differentiated using a simple digital algorithm.

Data Acquisition

Table 2 identifies the 17 data signals collected and stored continuously during testing on the dynamic facility. The table corresponds to many of the signals identified earlier in figure 12. Signals 0 through 11 in the table are derived directly from the instruments listed in the table as the *Signal Source*. Signals 12 through 16 were derived through continuous on line linear or nonlinear transformations of the first 12 signals, and were stored in data files along with the primary data.

As shown in figure 12, signals 9, 10, 11, and 16 were isolated from the computer system using custom designed high-voltage isolation amplifiers. These signals were subject to high-voltage spikes in the event of arcing within the ER shock absorber. The special isolation was necessary to protect the electronic circuits.

The high-voltage amplifier of figure 12 was a Trek Model 640. This amplifier is capable of following a sinusoidal command input of frequencies up to 10 kilohz. It can provide 200 watts of output power at up to ±10 kilovolts.

Table 2. Instrumentation and recorded data signals

No	*Signal Source*	*Signal*	*Symbol*
0	5 klb load cell	Road force 1	F_{R1}
1	10 klb load cell	Road force 2	F_{R2}
2	5 klb load cell	Road force 3	F_{R3}
3	LVDT	Road vertical displacement	d_R
4	Servo accelerometer	Road vertical acceleration	a_R
5	LVDT	Damper displacement	$d_{(S-U)}$
6	Servo accelerometer	Sprung mass acceleration	a_S
7	D/A filtered output	Road vertical displacement command	C_R
8	String pot	Sprung mass vertical displacement	d_S
9	H.V. amplifier output	Instantaneous voltage output	v_m
10	H.V. amplifier output	Instantaneous current output	i_m
11	Thermocouple & amplifier	Internal damper temperature	T
12	Derived data	Tire force	F_T
13	Derived data	Digitally filtered damper displacement	$d_{(S-U)f}$
14	Derived data	Damper velocity	$V_{(S-U)}$
15	Derived data	Sprung mass velocity	V_S
16	Derived data	H.V. amplifier command voltage	v_c

All data signals were collected at a sampling rate of 1700 hz through low-pass, 50 hz, analog filters. The delay between individual channel samples was 10 μsec at the A/D converter. The high acquisition rate was required to ensure enough data for effective filtering of derived damper velocities. Derived data were computed and updated by the controller at its command frequency, 100 hz. These data were subsequently over sampled (by a factor of 17) when the file was saved to produce a uniform 1700 hz data rate for all channels.

The data files contain 12-bit/sample data and conform to a standardized ERD file structure which includes measured amplifier gains and offsets for each channel, as well as channel names, units, and instrumentation notes. Data was reduced using *Split Plus*, a program designed to filter, subsample, and perform linear transformations on ERD data. All channels of all files were digitally filtered at 170 hz and subsampled to 340 hz prior to any analysis to reduce the number of data points (by a factor of 5).

The following linear transformation was performed to produce the tire-vertical-force signal.

$$F_T = (F_{R1} + F_{R2} + F_{R3}) - m^*a_R \qquad (18)$$

where m is the mass of the simulator's road element supported by the load cells. Since this mass lies between the load cell and point of tire-road contact, the last term of equation 18 is necessary to remove that portion of load cell force which is expended in accelerating the road, leaving the normal force at the tire/road interface.

The digitally filtered damper displacement, $d_{(S-U)}$, was computed using a 64-point moving window average.

$$d_{(S-U)f} = 1/64 * \Sigma(\text{last 64 } d_{(S-U)} \text{ samples acquired}) \quad (19)$$

The relative time of the last displacement sample acquired was noted for computation of damper velocity, $V_{(S-U)}$. Velocity was computed in in/sec using the equation:

$$V_{(S-U)} = (d_{(S-U)fn} - d_{(S-U)fn-1}) / (\Delta t) \quad (20)$$

where n is the sampling index and Δt is the time step between data samples.

The sprung mass velocity, V_S, was computed from the sprung mass acceleration, a_S, using the algorithm that combines integrator and high-pass-filter functions and which was discussed in section 3.1. The algorithms used to calculate the command voltage for the high-voltage amplifier were discussed in the previous section.

Power spectral densities (PSD) were computed using *Spectrum*, a program designed by UMTRI to convert time-sampled data to frequency domain forms. All road data were transformed to PSDs covering the frequency range of 0 to 15 hz in steps of 0.050 hz. The exceptions are CHV 01, CHV 06, and the sinusoidal tests, which could only be transformed in steps of 0.10 hz due to the limited length of the data files.

Transfer function gains were also found using *Spectrum*. Gains were computed for the road acceleration as an input and sprung mass acceleration or tire force as an output. All gain function results were subsequently window filtered with a window length of 0.20 hz prior to plotting.

Road Actuator Control

The road profiles were generated by the same computer that provided the data collection service. The profile was output as a waveform by a hardware-controlled D/A converter. The profiles were stored as columnar files, each value in a file representing a road vertical displacement in inches. Files could contain measured profiles of actual roads or idealized profiles such as sine waves, ramp functions, step waveforms, etc. Vertical displacement values were available at 4-in intervals longitudinally (three data points per foot). The speed at which values were output to the road servo depended on the speed of desired "travel" over the road.

Vertical displacement values were converted from in to integer values to drive a 12-bit D/A converter at a gain of ±2047/±5 in. (Values exceeding 5 in were clipped.) A self-recycling clock with a 10 μsec update time was loaded with the proper timing count to output values at equal time intervals. At each update interval, the next value in the profile was sent to the D/A converter. The analog output of the converter was filtered using a 1 khz, single-pole, low-pass filter prior to being passed to the servo amplifier. The filtered data was redigitized and collected as the road vertical displacement command, C_R.

Several preliminary tests were conducted using sinusoidal wave forms to drive the road simulator. The majority of testing, however, used road profiles provided by TACOM and modified by UMTRI to fit the limits of the road simulator.

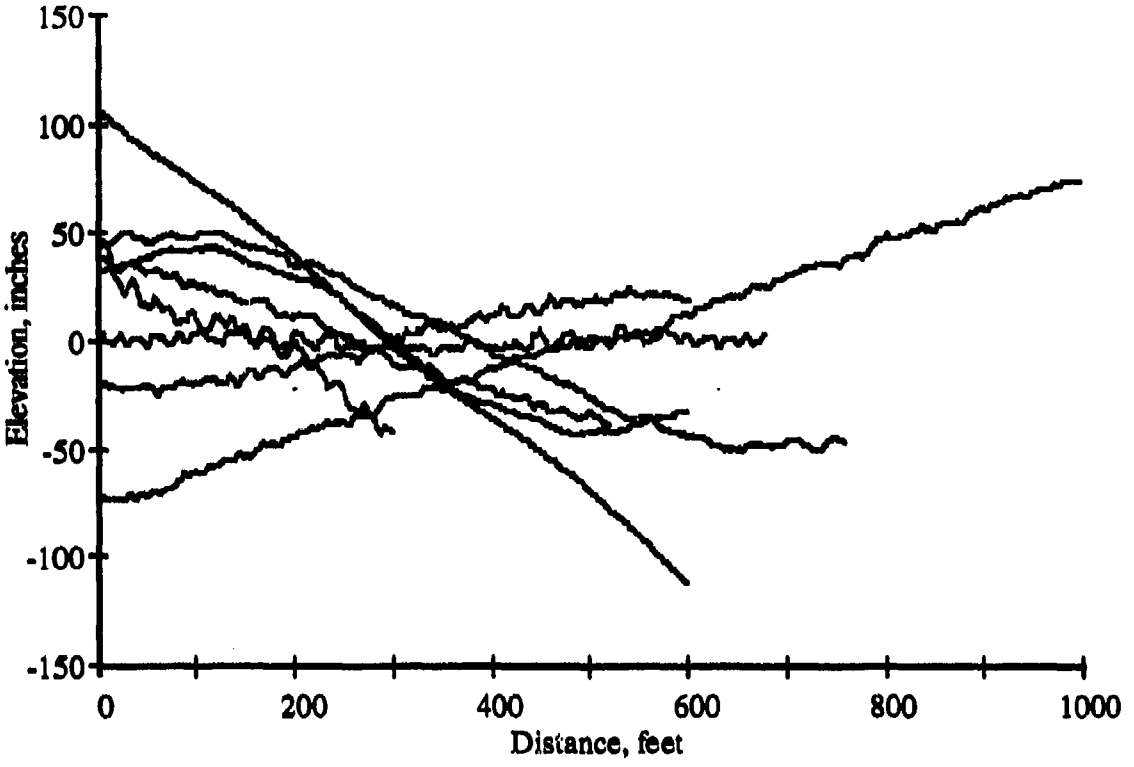

Figure 14. Road profiles provided by TACOM

Figure 14 shows the eight road profiles provided by TACOM. We understand the road profiles are of proving grounds courses at Aberdeen, Fort Knox, and elsewhere. The eight profiles provided are designated by TACOM as follows:

APG 09	CHV 01	FTKN 31	LET 5
APG 29	CHV 06	FTKN 34	
APG 37			

UMTRI modified these road profiles simply by subjecting them to high-pass filtering as required to constrain the total displacement to 10 in—the limit of the road simulator. This essentially means we removed the hills but left the bumps. The start and end of the individual road profiles were also trimmed to allow continuous repetitive running of the segment with a reasonable transition at the end-to-start interface. One example of the final form of a profile (derived from the longest profile of figure 14) is shown in figure 15. All of the road profiles used in testing are presented in appendix D.

The road simulator was not sufficiently powerful to follow these rough roads at any speed. The limitation was essentially the flow capability of the pump and was reflected in the maximum simulated forward speed. At higher speeds, the displacement command would have had to be attenuated in order to stay within the capability of the system. The theoretical relationship between simulated vehicle speed and the required displacement gain to allow continual running is show in figure 16. In practice, somewhat better continuous performance was attainable, and substantial improvement could be obtained

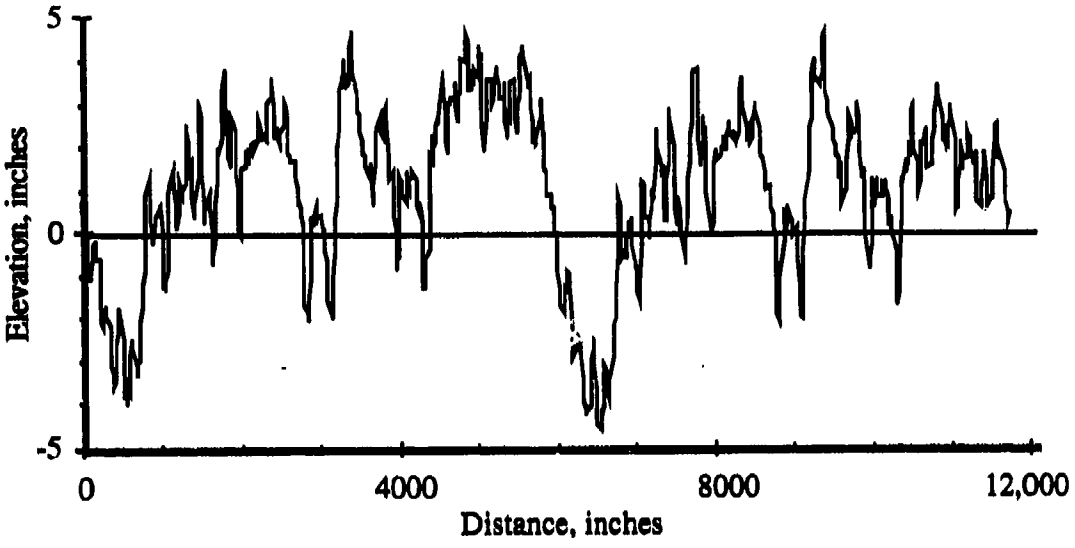

Figure 15. Modified road profile FTKN 31

for limited periods through consumption of accumulated fluid. The gain and speed conditions actually used in the test program are shown in table 3.

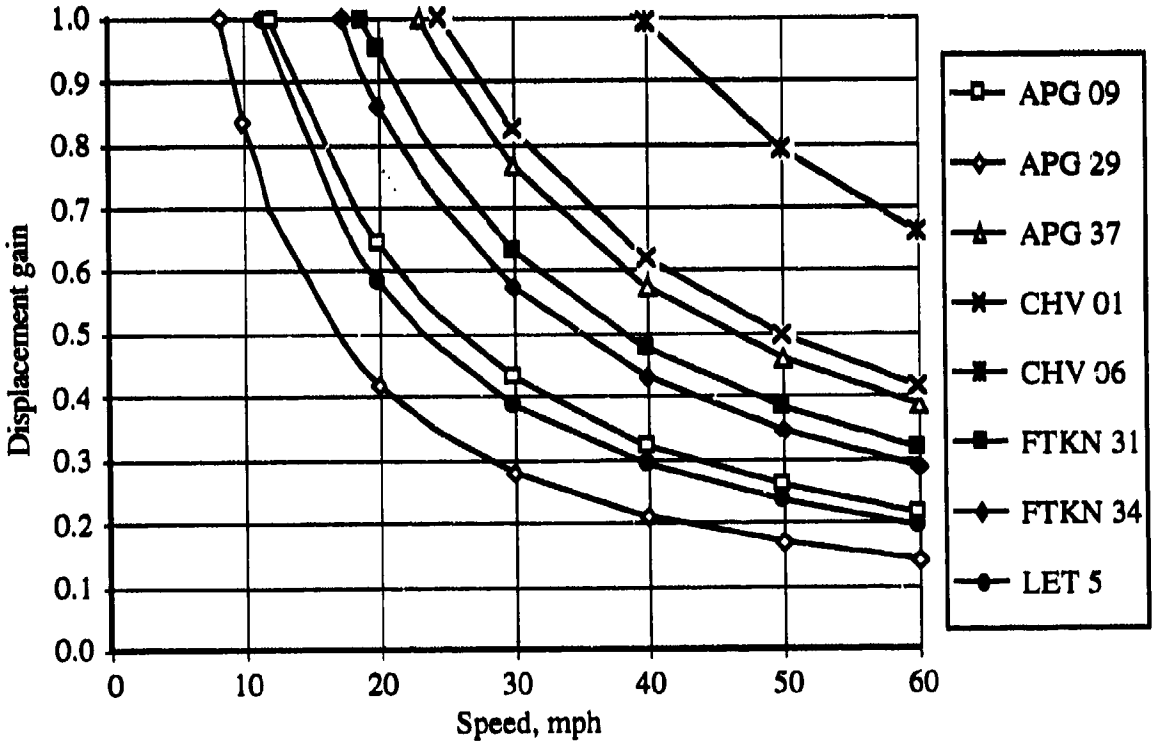

Figure 16. Continuous operation performance limits of the road simulator as a function of speed and road profile

Table 3. Road displacement gains and simulated velocities used in testing

Road Profile	APG 09	APG 29	APG 37	CHV 01	CHV 06	FTKN 31	FTKN 34	LET 5
Gain	0.7	0.7	0.7	0.7	0.7	0.7	0.7	0.7
Speed, mph	18	13	33	36	57	28	26	17

Dynamic Tests of the ER Damper Alone

A short series of dynamic tests were conducted on the ER damper to determine its coulomb and viscous friction response and to characterize the response time of the controlled force to applied voltage.

Figure 17 is a photograph of the test arrangement. The servo actuator used for the road simulator and the ER damper were arranged in line on the bed plate. The actuator was used to drive the damper directly through a load cell, which measured the damper rod force. An LVDT was used to measure the damper stroke.

Tests were conducted with three voltage wave forms: (1) $v_c = 0$ v for a complete run; (2) $v_c = 500$ v for a complete run; (3) $v_c = 500$ v at $t = 0$, stepping up to 2,500 volts at one third of the compression stroke and returning to 0 volts at two thirds of the compression stoke. For each wave form, four tests were run with the stroke speeds of 2, 4, 6 and 8 in/s, respectively. Data were used from the compression stroke only because the special plastic fittings used to isolate the ER shock electrically from the load cell were not strong enough in tension to resist the larger loads.

Tests conducted with the first wave form ($v_c = 0$ v) were intended to characterize the viscous behavior of the shock. The intent was to measure the steady-state response of the ER shock at the four velocity levels. Test results showed, however, that fairly large mechanical vibrations existed throughout the stroke. An example of the time history of shock force during one such test is shown in figure 18. After some informal experiments, the second test series using a command voltage of 500 volts was added with the hope of providing less noisy data. This was not particularly successful. In the end, steady state results were derived from both of these test series simply by processing the time histories through the appropriate low-pass filters. The processed data corresponding to the example of figure 18 are shown in figure 19.

The third test series involved step changes in command voltage from 500 volts to 2500 volts and back to 0 volts during the stroke. The resulting time histories of shock force were (1) low-pass filtered to obtain the steady-state response at 2500 volts, and (2) examined to characterize the response quality of the ER shock.

The steady-state results from the three test series are summarized in figure 20. This figure also includes the appropriate (i.e., at 0, 500, and 2500 volts) zero velocity data shown previously in figure 9. These static values from the earlier tests are generally below the trend shown by the steady-state values. The static values are the sum of the shock forces produces by coulomb friction (at zero volts) and the so-called Bingham yield stress of the ER fluid.

Figure 17. Photograph of the ER damper being tested alone.

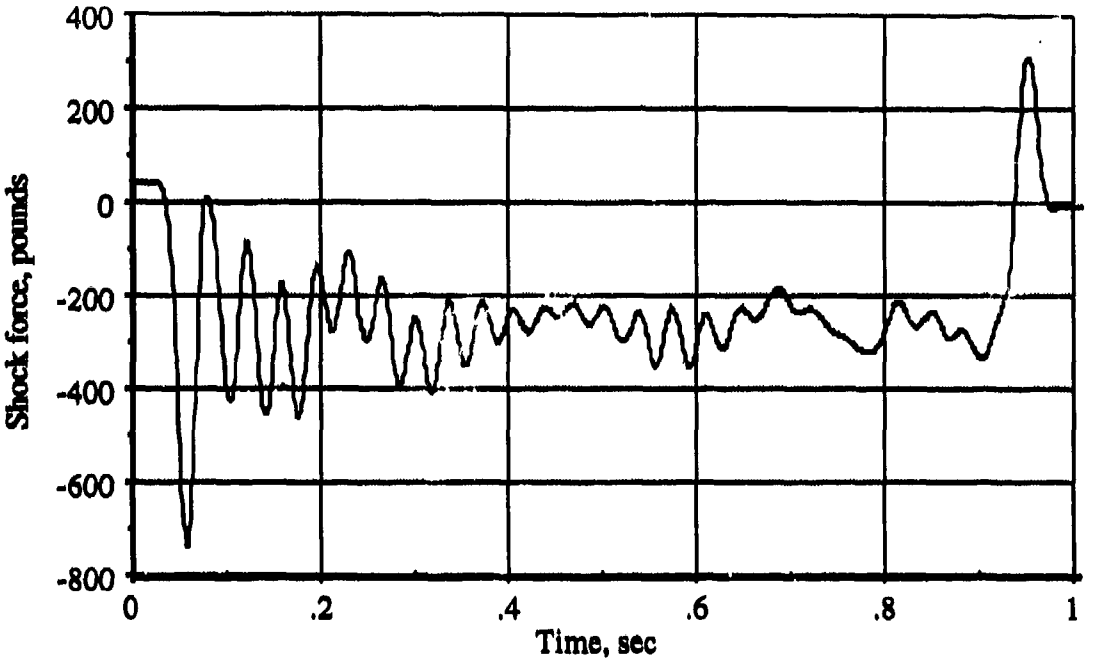

Figure 18. An example time history of ER shock force during a steady state test (4 inches per sec, 0 volts)

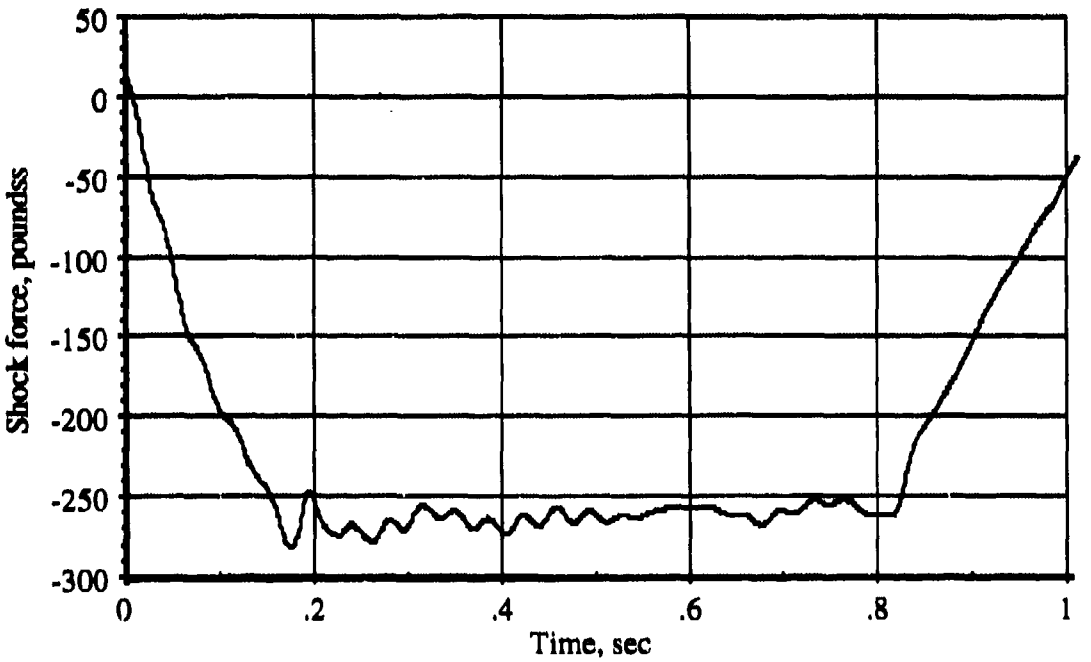

Figure 19. An example of a heavily filtered time history of ER shock force during a steady state test (4 in/sec, 0 volts)

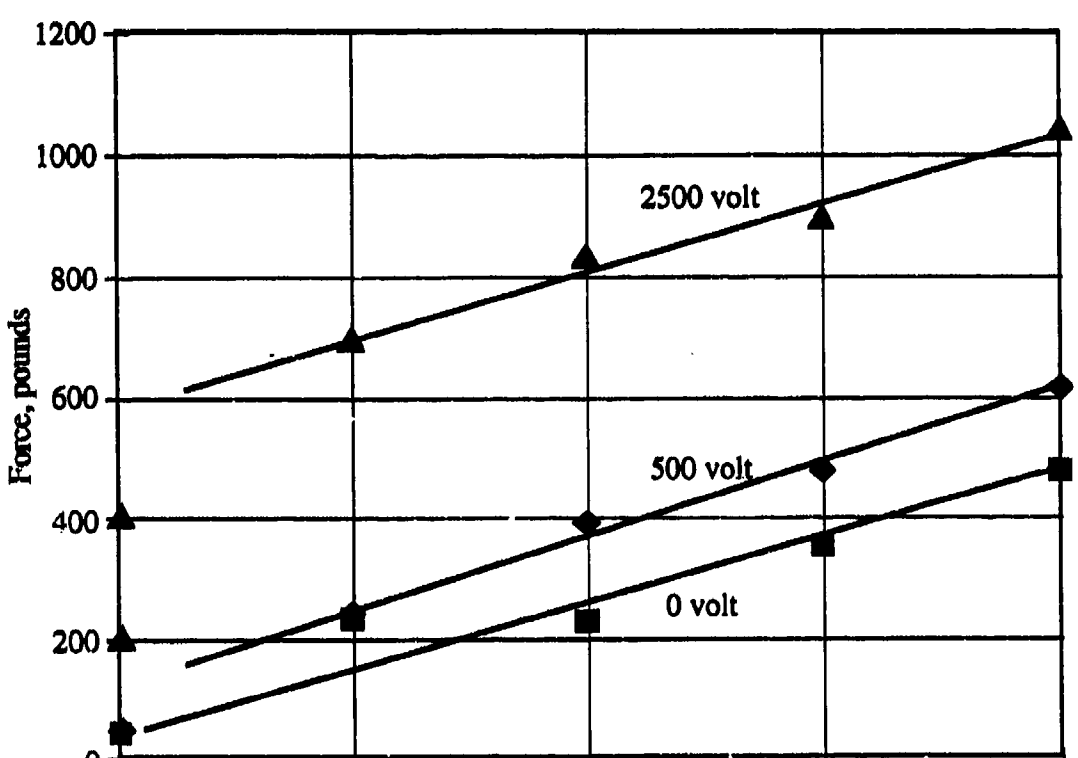

Figure 20. Summary of the steady-state test results

Among the steady-state data, the shock force at 2 in/sec and 0 volts deviates from the trend and almost coincides with the shock force at 2 in/sec and 500 volts. If this point is removed from the plot, a line fitted to the 0-volt line will be nearly parallel to the lines fitted to the 500- and 2500-volt data, respectively.

The slope of these fitted lines is indicative of the viscous response of the shock. The viscous damping forces are substantial, and larger than we had intended within the original design. This result is largely because the base fluid finally employed was transformer oil. Transformer oil has a higher viscosity than kerosene, which was originally expected to be used as the base fluid.

The vertical separation of the lines in figure 20 is related to the ER behavior of the shock. The shock forces at 2,500 volts are roughly two times higher than the zero-field forces. The shock forces at 4,500 volts, if achievable without arcing, would be approximately 4 times those at 2,500 volts (i.e., approximately 4,000 pounds) according to the 2.5^{th} power law (see equation 15).

The dynamic response of the ER shock absorber is illustrated in the time histories of figures 21 and 22. Each figure includes the time history of control voltage and current and the resulting shock force. Figure 21 shows the portion of a single test when

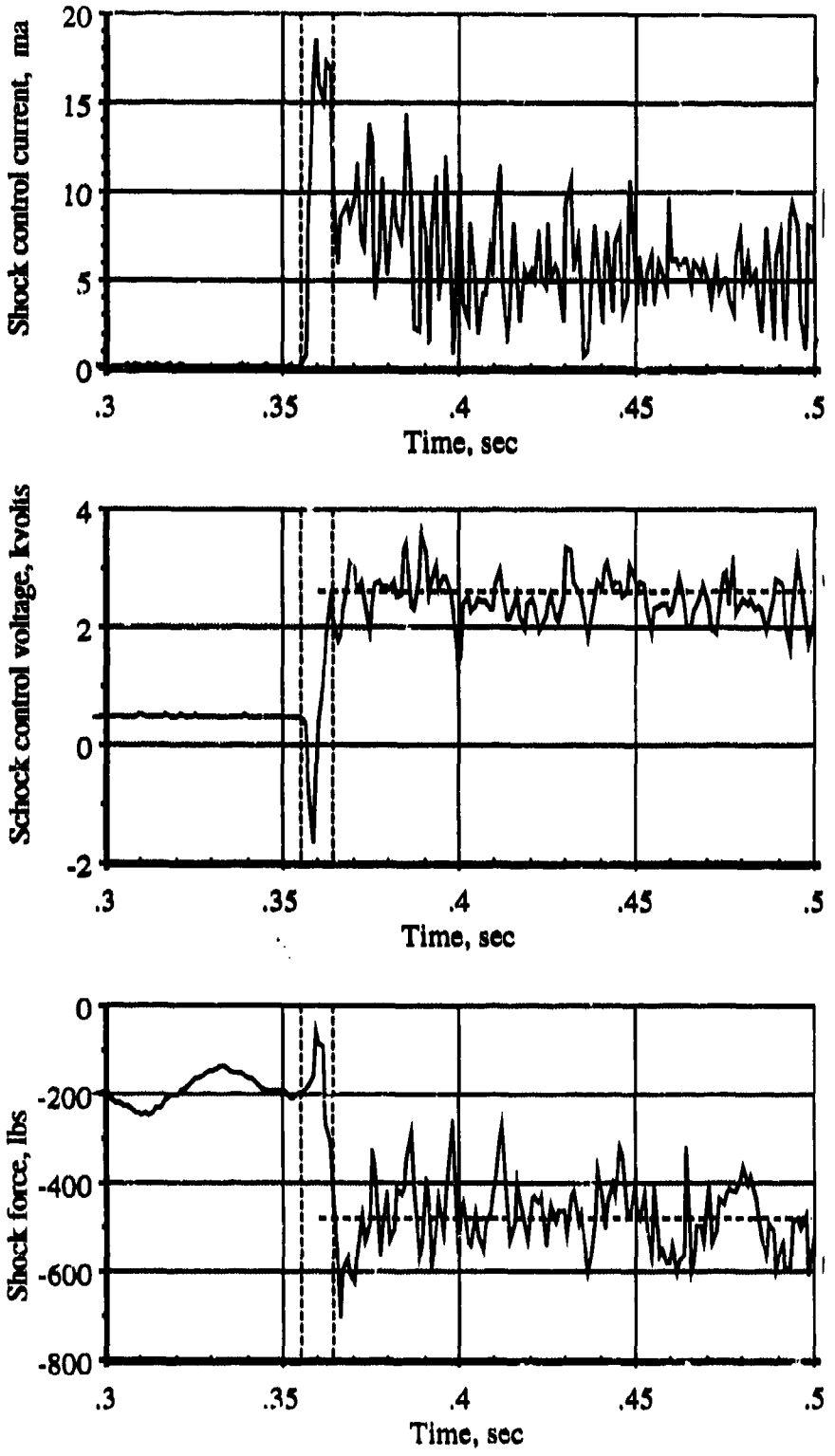

Figure 21. Timing of the ER shock control current and voltage, and shock force upon a step change of voltage command from 500 volts to 2500 volts

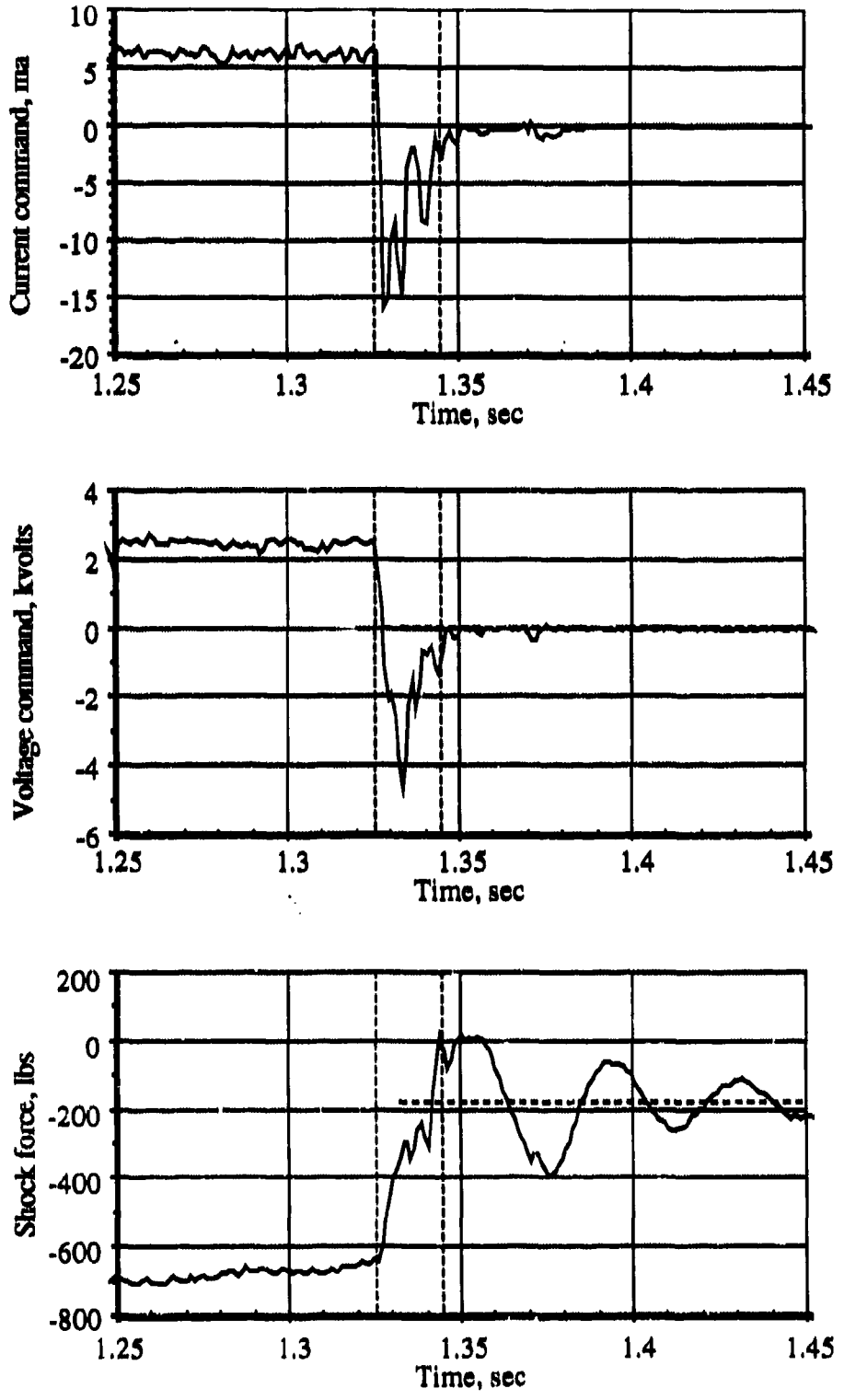

Figure 22. Timing of the ER shock control current and voltage, and shock force upon a step change of voltage command from 2500 volts to 0 volts

voltage stepped from 500 to 2500 volts. Figure 22 is from the same test at the time when the command voltage was stepped back down to 0 volts.

These time histories seem to show that when the step change in command voltage is requested, the change in current flow is very rapid, but the change in actual voltage lags slightly due to the need to charge the plates inside the ER shock. The force appears to develop virtually in phase with control voltage. Thus, it appears that the dynamic response of this system is limited by the response of the high-voltage amplifier, and the force responds to the voltage without appreciable lag.

Quarter-HMMWV Road Simulator Testing

The principal test series conducted on the road simulator involved analysis of the ride performance of the quarter-HMMWV over the road profiles provide by TACOM. However, a few preliminary tests to determine some fundamental system properties were done with pure sinusoidal road displacements.

The first of the sinusoidal tests were conducted with *no* damper installed. These tests were done at essentially the largest amplitude of road acceleration that did not cause the tire to leave the road surface at the resonant frequencies. (Relatively strong nonlinear qualities make the results discussed somewhat sensitive to magnitude.) These tests showed the sprung mass resonant frequency to be 1.5 to 1.6 hz and the unsprung mass resonance to be at 9 to 10 hz. Linkage friction and tire damping resulted in the sprung-mass mode being damped at about 0.1 of critical.

The ER damper was then installed in the quarter-HMMWV and sinusoidal tests in the frequency range of the sprung mass resonance were repeated with no control voltage applied. The results showed the resonant frequency to be in the 1.3 to 1.4 hz range and the equivalent damping to be about 0.25 of critical. It was thus apparent that the coulomb friction of the ER damper was appreciable in this system.

In the main series of tests, the quarter-HMMWV was exercised over each of the eight road profiles with four different damper conditions. These conditions were (1) ER damper with $v_c = 0$; ER damper with the skyhook control algorithm; ER damper with the conventional shock absorber control algorithm; and the standard HMMWV shock absorber.

The results of all of these tests were analyzed in the frequency domain. The transfer function between vertical acceleration of the road surface and vertical acceleration of the sprung mass was determined for each test condition. Additional analyses were performed to examine the transfer function between vertical acceleration of the road surface and tire-to-road normal force.

Figure 23 presents an example of the spectral analysis process undertaken for each test run. These data are from the run over surface APG 29 with the ER damper and zero control voltage. The top graph in this figure is a plot of the power spectral density (PSD) of the vertical acceleration of the road surface, that is, the spectral content of the input to the quarter-HMMWV. The middle graph is a plot of the PSD of the resulting vertical acceleration of the sprung mass—the output of the system. While the spectral content of

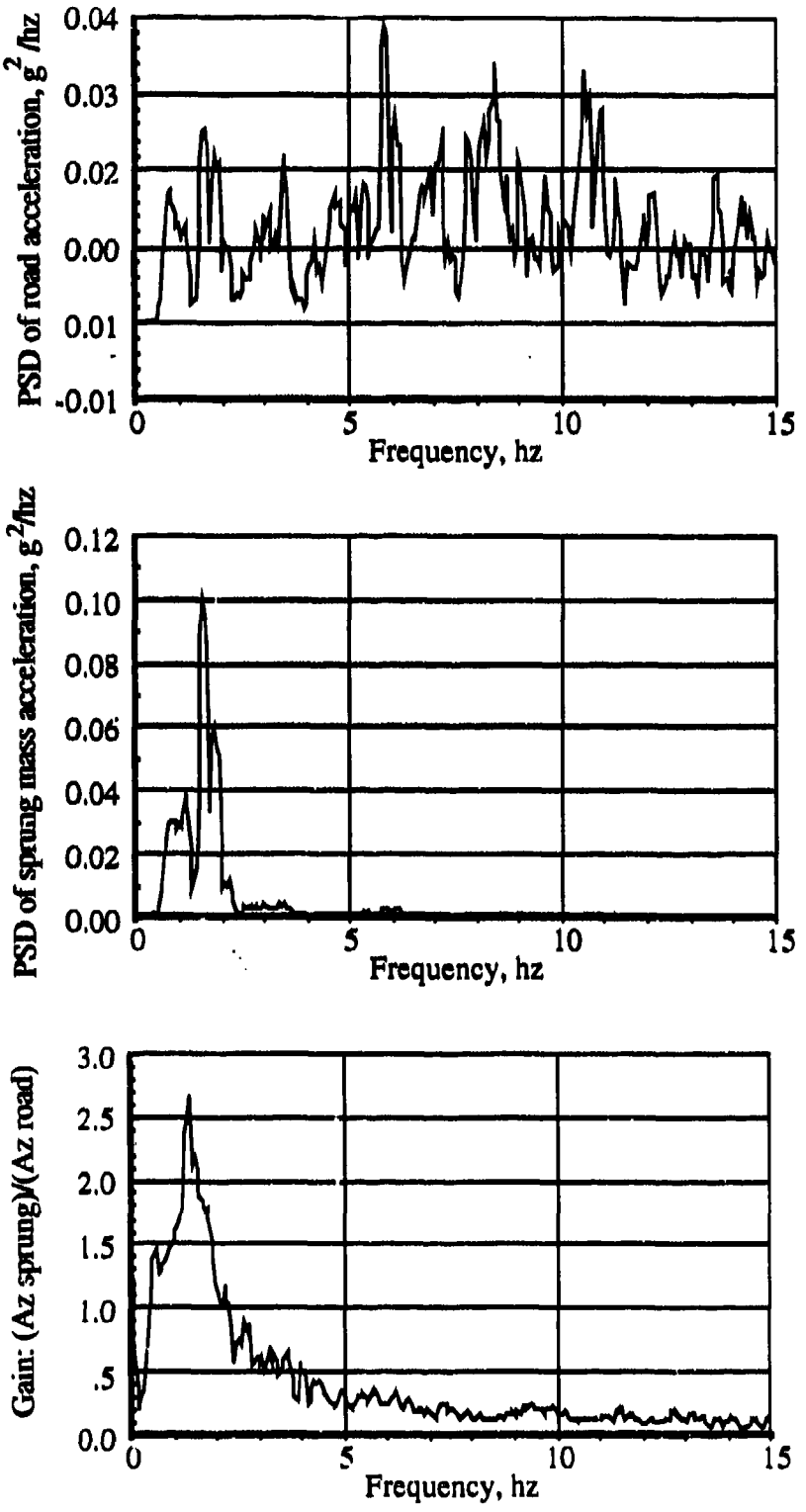

Figure 23. Example of spectral analysis data processing for APG 09, K=0

the input is relatively uniform, the content of the output is concentrated in the vicinity of 1.5 hz. This, of course, is because this is the natural frequency of the sprung-mass mode of the system, and the system resonates at this frequency. The bottom graph is a plot of the transfer function of the system. This plot is more-or-less (but not exactly), the square root of the PSD of the output divided by the PSD of the input, evaluated at each frequency. The plot is, in fact, the gain of the system as a function of frequency. This plot shows again that this system resonates, or amplifies the input, in the vicinity of the natural frequency of the sprung mass. At this frequency, the gain is greater than unity. However, the system effectively attenuates the input at frequencies above the sprung mass resonance. Note also, that there is a very mild rise in the gain at the unsprung mass resonance — around 9 hz. (This effect is small here, and might appear insignificant, but a similar rise of one amount or another is present around 9 hz in virtually all of the frequency domain data plots produced in this study.)

An ideal gain function for good ride quality would be one that strongly attenuates the dynamic response of the sprung mass at all frequencies. Practically, the goal of improved ride is to reduce the gain appreciably at the sprung-mass resonance without substantially increasing gain at the unsprung-mass resonance.

Figure 24 shows the system gain (similar to the bottom plot of figure 23) measured on APG 29 with three different damper conditions. The upper plot shows the gain with the ER damper installed but with no voltage command. The center plot shows the system gain with the ER damper operating as a skyhook damper. The bottom plot is for the system with the standard HMMWV shock absorber installed. These data clearly show the ER damper in the skyhook control mode to be more effective at reducing the amplification of acceleration at the sprung mass resonance than the standard shock absorber. A small increase in response for the system with the skyhook damper is noted in the mid range frequencies from 5 to 10 hz.

Figures 25 and 26 address two other ancillary issues, again with example data from APG 29. Figure 25 compares the system gain with the standard shock absorber (bottom plot) to the gain when the ER damper is operated with the conventional shock absorber control algorithm. It is apparent that with the control constants chosen ($k_c = 8x10^6$ v[in/sec]$^{-0.4}$ and $k_t = 16x10^6$ v[in/sec]$^{-0.4}$) , the two shocks are quite sirnilar. The point to be made is that the control constant used in the skyhook algorithm ($k = 15x10^6$ v[in/sec]$^{-0.4}$) is of a similar magnitude and will generate forces of generally the same or smaller[2] magnitude then the conventional shock absorber. The improved performance of the skyhook approach can thus be seen to result from the strategic advantage of the semiactive control approach.

Figure 26 is similar to figure 24, but the gains shown are of tire-to-road normal force with respect to road acceleration. This gain is of interest because low levels of dynamic components of the tire-to-road contact force are desirable for enhanced road holding.

---

[2] Sky hook damper forces can be expected to be smaller than forces developed by a conventional shock absorber with similar properties because the applied velocities are smaller. The sky hook damper is subject only to sprung mass velocities. The conventional damper is also subject to the velocity of the unsprung mass which moves faster.

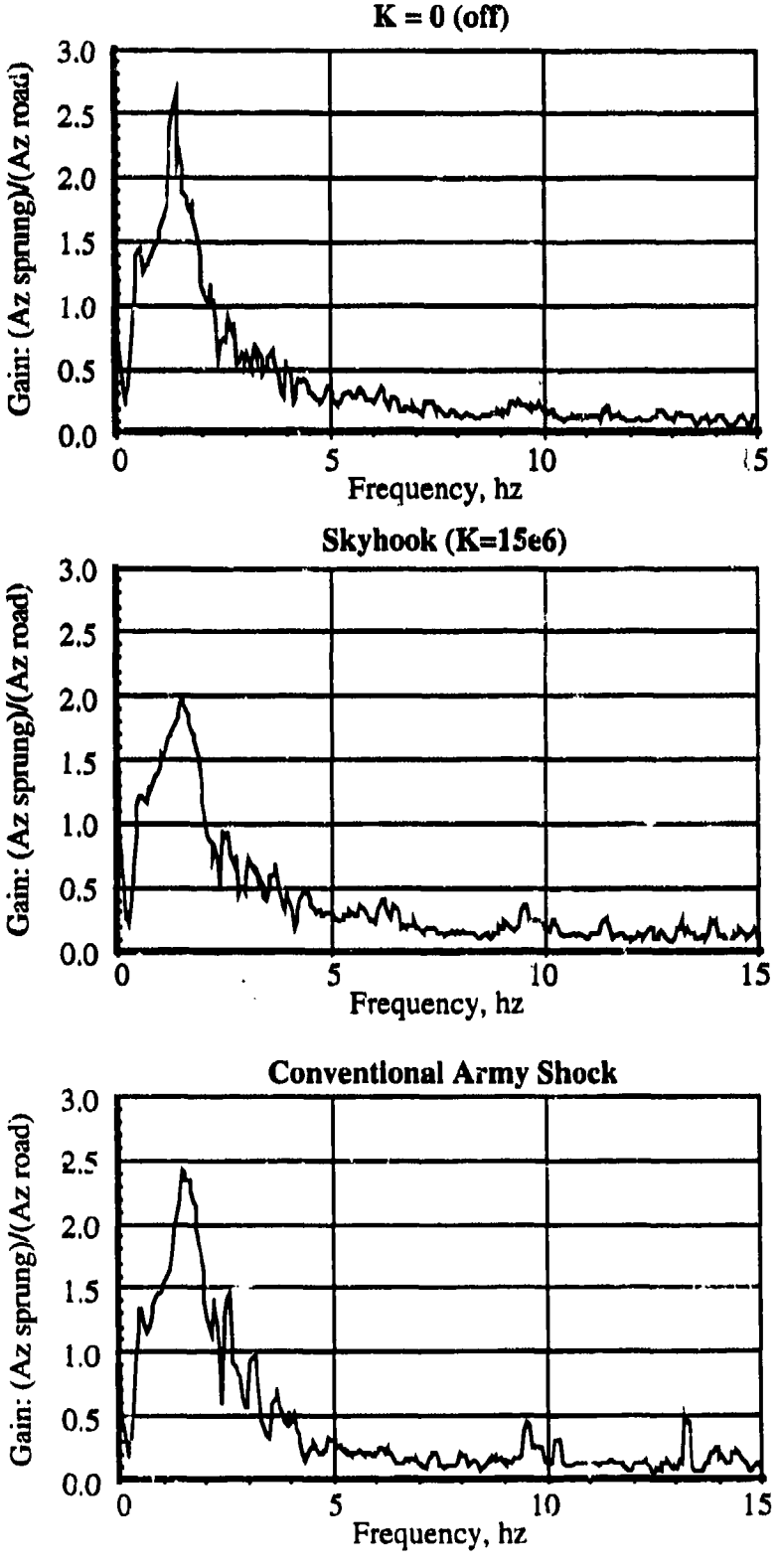

Figure 24. Example sprung mass acceleration gains measured with three different shock absorber conditions for APG 29

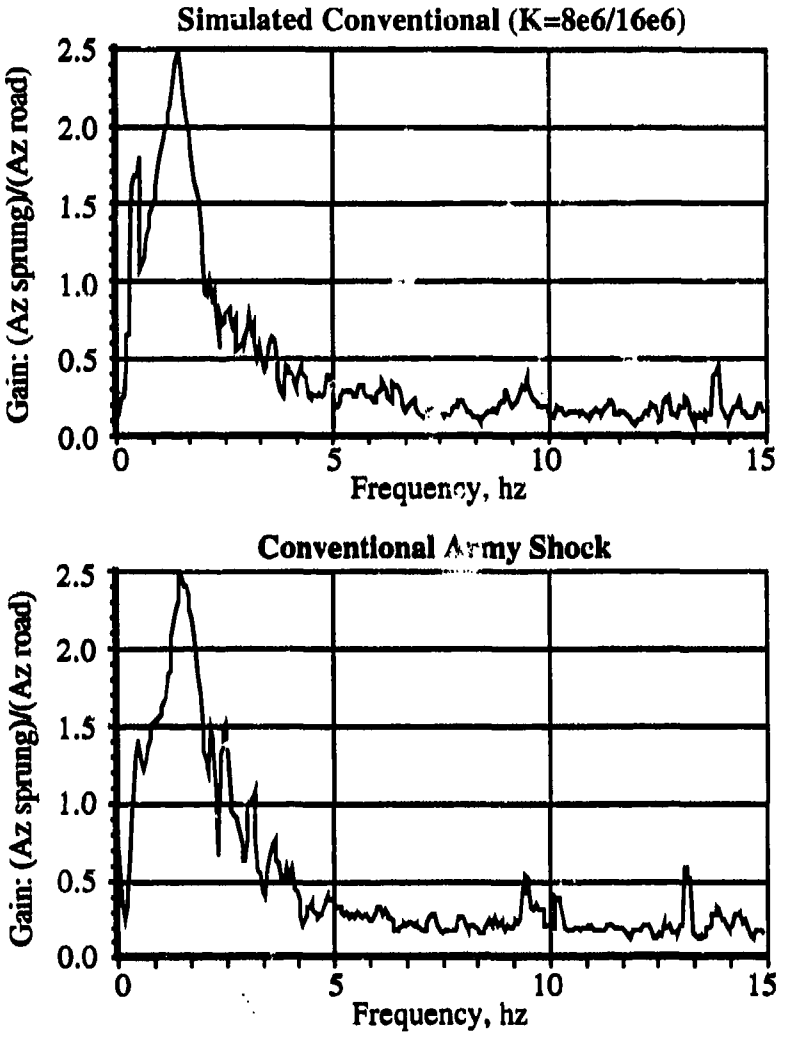

Figure 25. Example sprung mass acceleration gains measured with simulated and actual conventional shock absorber for APG 29

Although the magnitudes of this gain are quite different from those of figure 24, the relative performance of the three types of shocks is similar to that which prevailed in the earlier figure.

The example data presented here all came from test runs using the APG 29 road profile. Measured gain functions for all of the road profiles are presented in appendix D. If the vehicle systems were linear, the gain functions would all appear the same regardless of the road. However, this system contains substantial non-linear elements. We have seen that coulomb friction in the linkages and the ER damper is significant. All of the shock absorbers have significant nonlinear qualities. The conventional shocks (standard shock or the conventional algorithm applied to the ER damper) are nonlinear due to different compression and extension rates. The logical switching function of the skyhook algorithm is very nonlinear. Finally, the large displacement road profiles cause

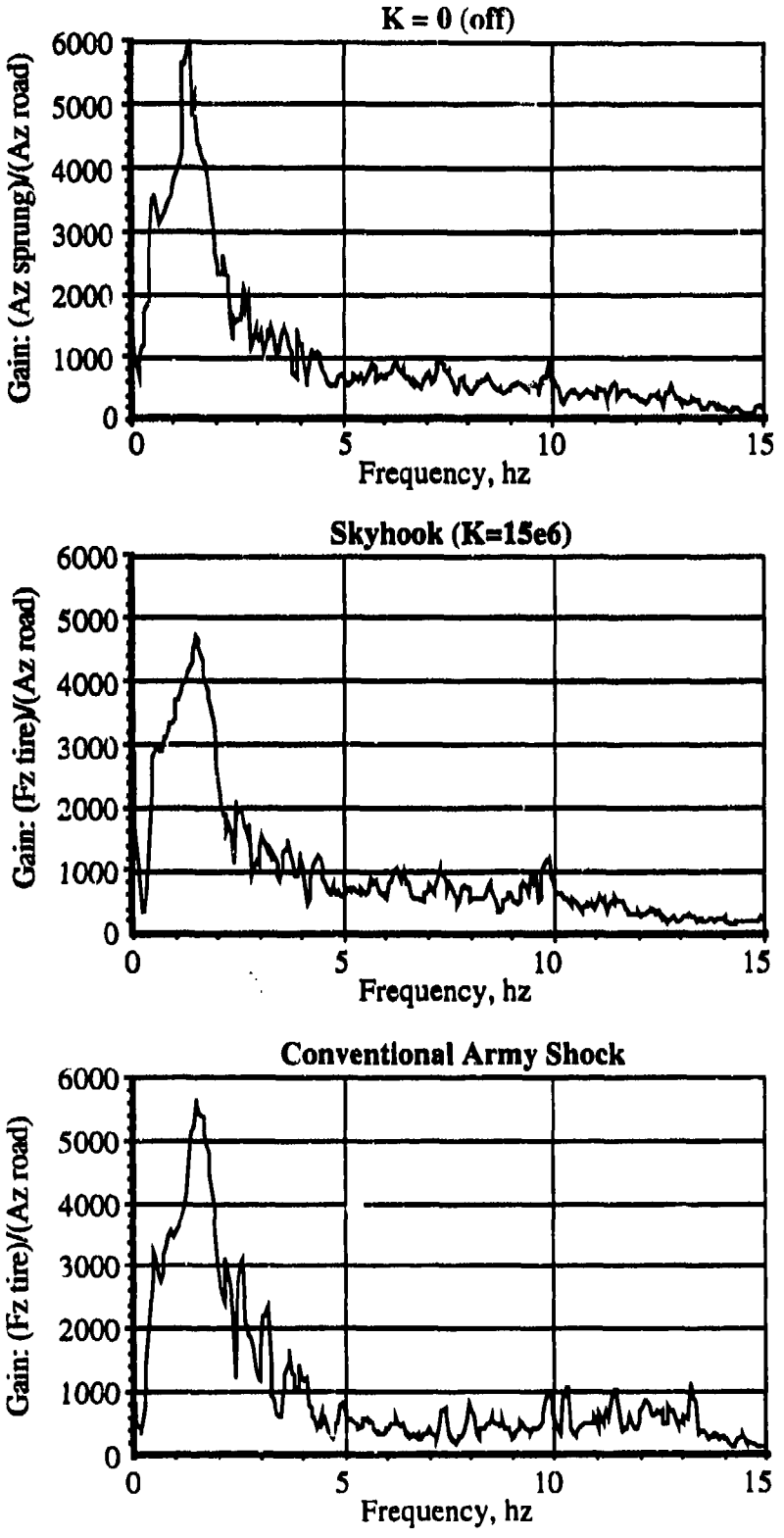

Figure 26. Example tire force gains measured with three different shock absorber conditions for APG 29

the tire to operate in its nonlinear range (including tire lift). Thus, the results from different roads are indeed different, but they virtually all maintain the same relative performance relationships observed in the examples presented here. Thus, we conclude that this testing program has successfully demonstrated the potential effectiveness of ER fluid technology in intelligent suspension control applications.

7. Quarter-Car Model of the System

For this study, the semiactive system was simulated using the quarter model as shown in figure 7.4. The complete simulation is provided as a computer program listing in appendix C. A review of the simulation and brief discussion of calculation results is presented in this section.

The momentum equation for the sprung mass is simplified as

$$M_S \frac{dx_S^2}{dt^2} = F_d + K_S(x_U - x_S) \tag{21}$$

where M_S is the sprung mass, K_S the spring constant, F_d the damping force (positive during compression), t the time, x_S the sprung mass displacement, x_U the unsprung mass displacement.

The momentum equation for the unsprung mass is

$$M_U \frac{dx_U^2}{dt^2} = -F_d - K_S(x_U - x_S) + K_T(x_G - x_U) \tag{22}$$

where M_U is the unsprung mass, K_T the tire spring constant, and x_G the ground displacement.

In a shear-mode damper, the influence of the inertia force is relatively small, and the damping force in the strut F_d can be approximated with a Newtonian damping force F_{dN} and an ER damping force F_{dER}, corresponding to the effects of the plastic viscosity (η) and the yield shear stress (τ_y), respectively, in the Bingham model (Lou *et al.*, 1992). (See equations 4 and 5 in chapter 5.) The Newtonian and ER damping forces here are completely uncoupled and additive. However, a complete solution of the problem demands a full solution of the fluid flow problem (Lou *et al.*, 1993).

From equations 14, 15, and 16 (chapter 6), one can derive that the damping coefficient for the ER damper is equal to $k_v k$. With $k = 15 \times 10^6 \ volt^{2.5}(in/\sec) = 590.55 \times 10^6 \ volts^{2.5}(m/\sec)$ and $k_v = 4.445 \times 10^6 \ N/volt^{2.5}$, the ER damping coefficient is 2,625 N/(m/s). If one uses a sprung mass of 998 kg and a spring constant of 0.1633×10^6 N/m, the ER damping ratio is 0.1028.

The viscosity of the ER fluid at zero-field was not directly measured. From the slope of the 0-volt line in figure 20, it was calculated that the zero-field viscosity $\eta = 222$ cP or $0.222 \ Ns/m$.

Similarly, the viscosity variation of the ER fluid as a function of the electric field was not directly calibrated in this study. The value of β in equation 15 which was 2.5, is based on the data in figure 9. These data show only the static response of the ER damper. The steady-state data in figure 20 may better represent the ER effect. The related

information from figure 20 is listed in table 4. The relationship between the yield stress and the electric field is almost linear. The disagreement between the static and steady-state data are thus significant. Both cases may contain errors. ER fluids are known to have erratic behaviors at zero or low shear rates. The existence of the static yield shear stress is the subject of scientific debate. Only two elevated voltage values are available in the steady-state data, and it is therefore difficult to rely on these data to derive the ER law. The approach in the numerical simulation is a compromised one. We chose a β value of 2, which falls between 1.0 (steady-state case) and 2.5 (static case). We have

$$\tau_y = 95 \times 10^{-6} V^2 \tag{23}$$

where V is the voltage, and the constant 95×10^{-6} is derived based on the yield stress at 2,500 volts. Data at 500 volts were ignored because of the proximity between 500 and 0 volts and the dominance of the ER behavior at 2,500 volts.

Table 4. Information from figure 20

voltage	*ER damping force* F_{dER}	*ER yield stress* τ_y
500	591 N (133 lbf)	140 Pa (0.020 psi)
2500	2,504 N (563 lbf)	594 Pa (0.086 psi)

The steady-state data were obtained and analyzed after the dynamic tests of the ER damper, where the 2.5th power law was used in controlling the voltage applied to the damper. In order to compare the numerical results with the dynamic test results, the voltage in the simulation will be controlled in the same manner, that is, according to the 2.5th power law. However, the ER response to the electric field is based on the 2nd power law, which is believed to be also governing the ER response during the dynamic tests.

During the dynamic tests, the maximum cutoff voltage was set 3,000 volt, which is also used in the numerical simulation. Based on the 2nd power law and the ER yield stress value at 2,500 v, the ER yield stress at 3,000 volts is about 855 Pa (0.124 psi), which is far from ideal. With the zero-field viscosity $\eta = 222$ cP or 0.222 Ns/m, the Newtonian shear stress reaches 855 Pa if the shear rate is at 3,851 s^{-1}.

Although ER fluids respond to the field variation rapidly, the response is not instant. The voltage across a capacitive ER damper has a delay of its own. These two delays are simply lumped together in a delay time constant τ_{delay} in the following equation,

$$\frac{\partial \tau_y}{\partial t} = \frac{1}{\tau_{delay}} (95 \times 10^{-6} V^2 - \tau_y) \tag{24}$$

The ER damper is simulated in any one of the following three control types, as described in chapter 5,

(1) Passive damper (i.e., no ER control). The electric field is set at zero, and only Newtonian viscosity is left to damp the relative motion.

(2) The skyhook damper. The electric field is regulated to damp the absolute vertical velocity of the sprung mass.

(3) Simulated conventional damper. The electric field is regulated in such a way that the damper behaves like a conventional bilinear shock absorber.

A computer code is developed using the mathematical model and control strategies discussed above. The momentum equations are integrated over the time domain.

At time zero, both the sprung and unsprung masses are set motionless, and the ground displacement is zero. A sinusoidal vertical displacement is then imposed at the ground, and the simulation continues with many cycles until a stable periodic motion is achieved by the sprung mass. More specifically, the simulation is stable when the normalized deviation between the sprung mass acceleration amplitudes of two consecutive cycles is within 0.01 percent. For most runs of the simulation, stable solutions are obtained within 10 cycles. Simulation output from the last cycle is used for portraying the results.

Each sinusoidal cycle is divided into a finite number of time steps of equal step-size. For runs presented in this study, there are 360 steps in each cycle, with the step-size being one degree out of a 360-degree cycle. At each time-step, the numerical integration is implemented with an explicit finite-difference scheme. The accelerations of the sprung and unsprung masses are iterated with a relaxation factor, which is equal to 0.2 in the runs presented in this report. The iteration stops when the normalized convergence of the sprung mass acceleration is within 0.1 percent.

The quarter-car model was simulated with each of the three control types (i.e., no ER control, skyhook, and simulated conventional). For each control type, a spectrum of 25 frequencies are tested, at the values of 0.1, 0.2, 0.5, 0.8, 1.0, 1.5, 1.8, 1.9, 2.0, 2.5, 3.0, 4.0, 6.0, 7.0, 8.0, 8.5, 9.0, 9.5, 10, 14, 16, 18, 20, and 25 hz. Other major parameters used in the simulation are listed in table 5. There are 40 hot electrodes, i.e., 40 pairs of hot and ground electrodes facing each other. The gap between each pair of electrodes is 1 mm. The outer radius of the shear surface is equal to the outer radius of the hot electrodes, i.e., 4.83 cm. The inner radius of the shear surface is equal to the inner radius of the ground electrodes, that is, 2.95 cm. kg/m^3. The ER fluid mass density is chosen to be 1,000 kg/m^3. The Newtonian viscosity is equal to 222 cP, which is derived from the steady-state data as discussed earlier. The sprung and unsprung masses and spring stiffnesses are effective values, i.e., their equivalent values for the quarter car model. The tire spring stiffness is 0.4638×10^6N/m, and damping in the tire is neglected. The skyhook command constant is 5.9055×10^8 volt$^{2.5}$s/m. For the simulated conventional damper, the command constants for compression and extension are 3.1500×10^8 and 6.3000×10^8 volt$^{2.5}$s/m, respectively. The time delay constant is 0.2 ms, which is more or less arbitrary but not critical for the frequency range of the simulation. The peak voltage, which the control voltage is not allowed to exceed, is 3,000 volts. The ball screw has a lead angle of 17.66 degrees and a pitch diameter of 2.54 cm. Its frictional coefficient is 0.03, which, in combination with other parameters, results in an efficiency of 90 percent given by the manufacturer.

Table 5. Parameters used in the simulation

Parameters	*Values*
Number of hot electrodes n	40
Gap between electrodes h	1 mm
Shear surface outer radius r_o	4.83 cm
Shear surface inner radius r_i	2.95 cm
ER fluid density ρ	1,000 kg / m^3
Newtonian viscosity η	0.222 Ns/m^2 (222 cP)
Effective sprung mass M_S	998 kg
Effective unsprung mass M_U	181 kg
Effective spring stiffness K_s	0.1633×10^6 N / m
Tire spring stiffness K_T	0.4638×10^6 N / m
Skyhook command constant k	5.9055×10^8 $Volt^{2.5} s / m$
Conventional compression const k_c	3.1500×10^8 $Volt^{2.5} s / m$
Conventional extension constant k_t	6.3000×10^8 $Volt^{2.5} s / m$
Delay time constant τ_{delay}	0.0002 second
Peak voltage	3,000 v
Ground wave amplitude	1 cm
Ball screw lead angle λ	17.66 degrees
Ball screw pitch diameter D_p	2.54 cm
Ball screw frictional coefficient f	0.033, along with other parameters, to give an efficiency of 90 percent.

Time histories of the sprung mass velocity V_S, the sprung-unsprung mass velocity difference $V_{(S-U)}$, Newtonian damping force F_{dN}, and ER damping force F_{dER} at an excitation frequency of 1.5 hz and under the skyhook control strategy are presented in figure 27. For the ease of presentation, V_S and $V_{(S-U)}$ are normalized by the amplitude of the ground velocity, and F_{dN} and F_{dER} are scaled down by a factor of 1000. The Newtonian damping force F_{dN} responds linearly (with an opposite polarity) to the relative velocity $V_{(S-U)}$. The ER damping force F_{dER} is linearly proportional to the negative sprung mass velocity (- V_S) when V_S and $V_{(S-U)}$ are of the same polarity (approximately between 0 and 120 degrees and between 180 and 300 degrees in figure 27) and equal to zero when V_S and $V_{(S-U)}$ are of the opposite polarities (approximately between 120 and 180 degrees and between 300 and 360 degrees in figure 27). For this

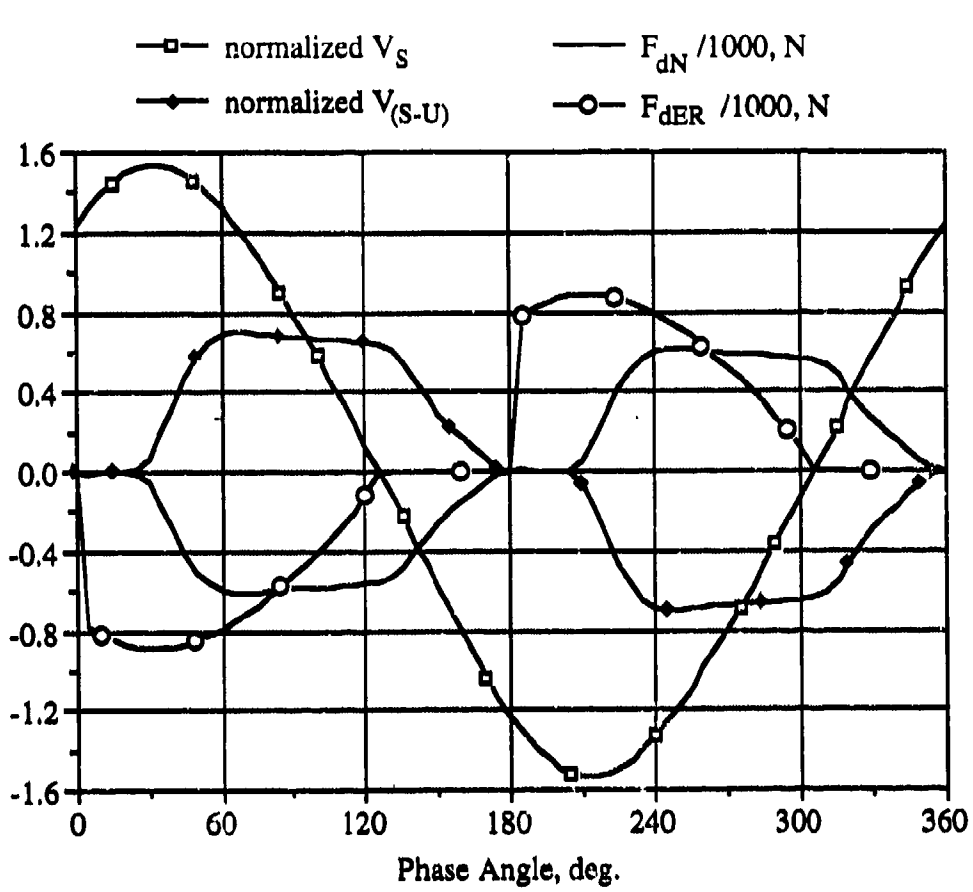

Figure 27. Time histories of the sprung mass velocity V_S, the sprung-unsprung mass velocity difference $V_{(S-U)}$, Newtonian damping force F_{dN}, and ER damping force F_{dER} at an excitation frequency of 1.5 hz and under the skyhook control strategy

particular case, the peak ER damping force is about twice the peak Newtonian damping force.

Time histories of the sprung mass displacement, velocity, and acceleration and the unsprung mass displacement, velocity, and acceleration for the same run are plotted in figure 28. The velocities are again normalized by the amplitude of the ground velocity. The displacements and accelerations are normalized by the amplitudes of the ground displacement and acceleration, respectively. The variables of the unsprung mass have generally more high-frequency components than those of the sprung mass because of its small mass. The unsprung mass is more or less "pushed around" by the sprung mass. The gain of the sprung mass, that is, the sprung mass acceleration normalized by the ground acceleration amplitude, is 1.393.

The gain of the sprung mass under (1) no-ER control, (2) skyhook control, and (3) simulated conventional control are presented in figure 29. The skyhook control is generally better, in terms of reducing the gain, than the simulated conventional control, which is in turn better than no ER control. In the vicinity of 2 hz, the gains of no-ER control, skyhook control, and simulated conventional control are 2.7, 1.5 and 2.1,

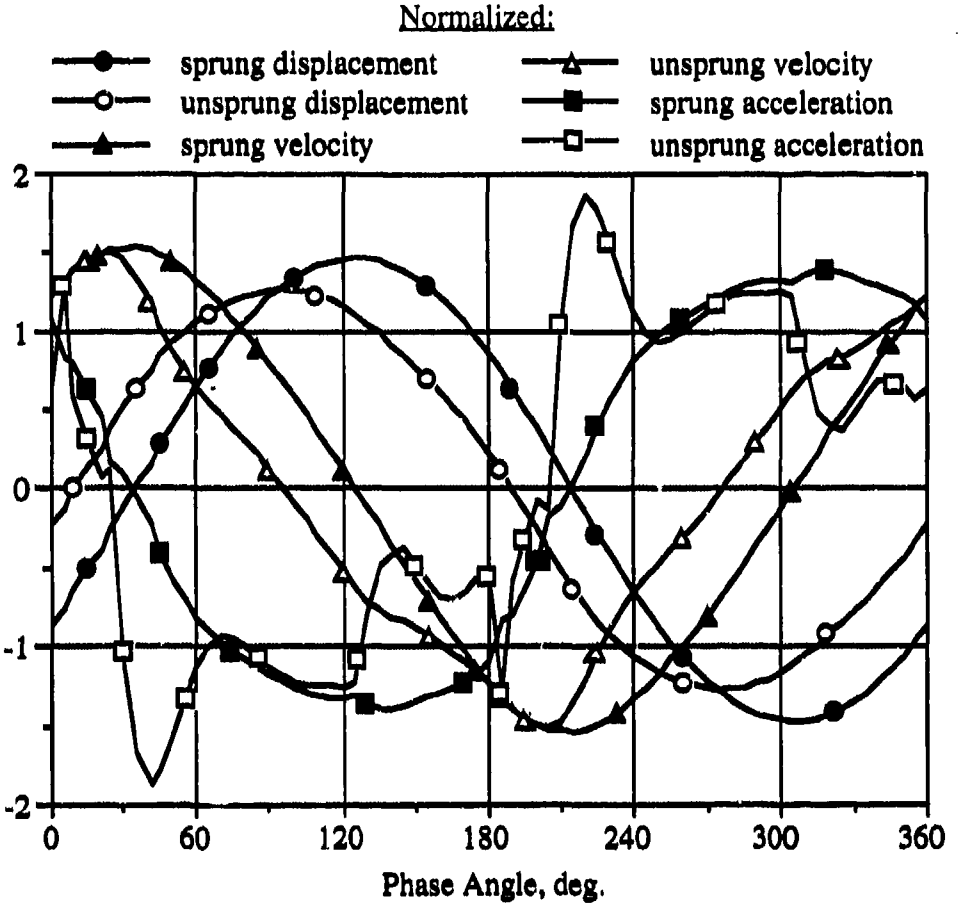

Figure 28. Time histories of the sprung mass displacement, velocity, and acceleration and the unsprung mass displacement, velocity, and acceleration at an excitation frequency of 1.5 hz and under the skyhook control strategy

respectively. The corresponding gains in the experiments (figures 24 and 25) are 2.7, 2.0, and 2.5, respectively. The numerical simulation results generally agree with the experimental results. In particular, the gain values do not show notable increases in the vicinity of the wheel-hop frequency, 9 hz.

The frequency responses of the unsprung mass gain under (1) no ER control, (2) skyhook control, and (3) simulated conventional control are plotted in figure 30. For the unsprung mass, the gain at the vehicle resonance frequency is higher under the skyhook control than under either no ER control or simulated conventional shock. The unsprung mass is again "pushed around" by the sprung mass, whose damping is the dominant priority of the skyhook control scheme.

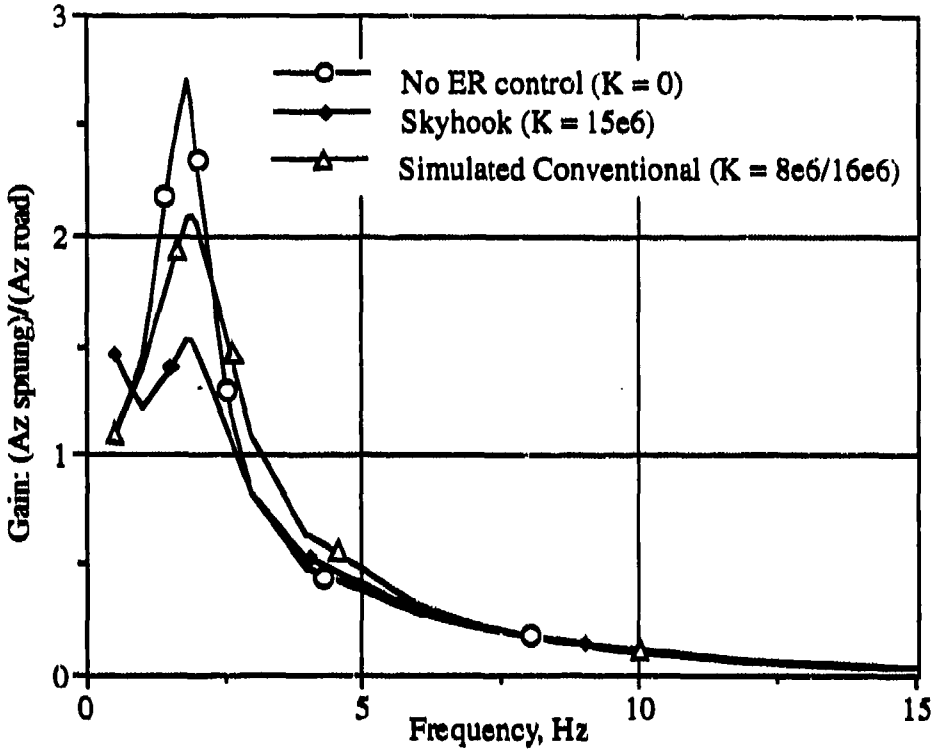

Figure 29. The frequency responses of the sprung mass gain under (1) no ER control, (2) skyhook control, and (3) simulated conventional control

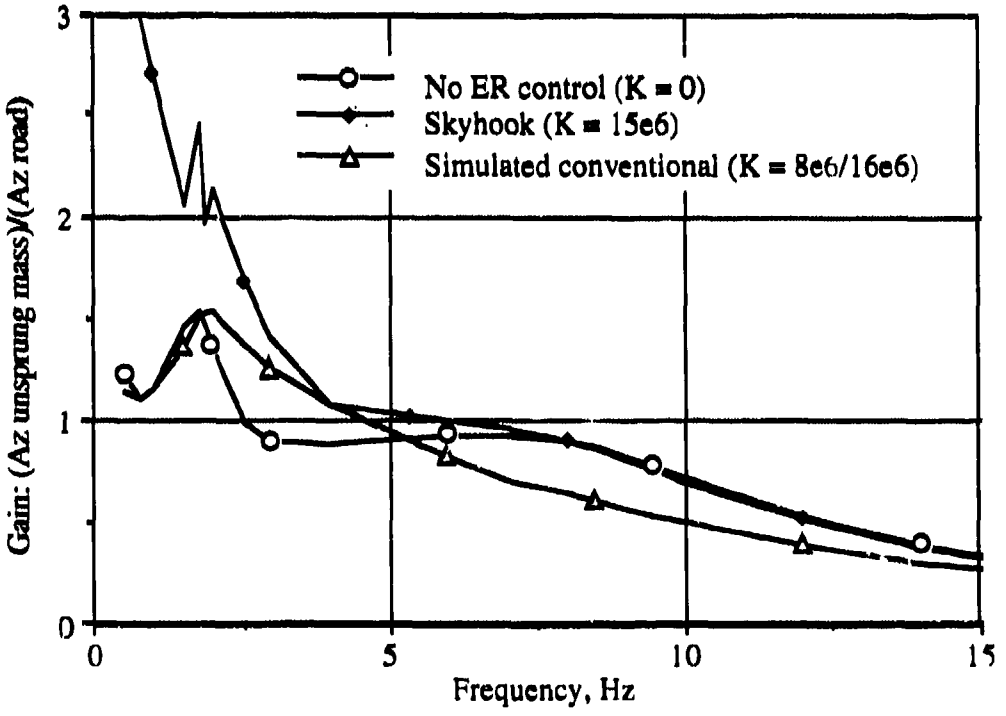

Figure 30. The frequency responses of the unsprung mass gain under (1) no ER control, (2) skyhook control, and (3) simulated conventional control

8. Conclusions

The working prototype of an electrorheological damper has been developed and demonstrated. This device has shown a level of suspension control that is superior to that of conventional shock-absorber damping. This demonstration is significant primarily because it illustrates the system-level capability of ER technology. That is, it is more or less straigh*forward at the present time to configure an ER device to control force or moment over a broad bandwidth of responses in certain classes of automotive devices. On the other hand, the project has also documented that performance limitations continue to constrain the range of achievement with ER devices.

As the project concludes in early 1994, it is also apparent that parallel advancements in ER fluid technology are offering to extend the fluid performance range and to make possible entirely different design approaches for configuring an automotive suspension damper. For example, an American chemical supplier is advertising ER fluids with 1.0 pounds per square inch shear strength capability. The fluids are comprised of cross-linked polyurethane particles in silicone oil. If such a fluid was found to exhibit other suitable attributes, it would allow the design of a purely rotary damper that would avoid the relatively high complexity and weight of the ER damper that was prototyped in this study. A rotary damper of this type could be fitted along the centerline of the inboard pivot of either the lower or upper control arm of the HMMWV suspension.

The test methodology shown in this study is also instructive of practices that are suited to the measurement of the performance of ER suspension controllers. In particular, the study employed certain novel optical isolators which protect equipment from the high-frequency voltage spikes which may attend inadvertent arcing within the ER device. Believing that arcing will be inevitable in any developmental setup with ER fluids (operating at kilovolt levels of excitation) such protection is axiomatic. Also, the ability to produce displacements of a simulated road surface which follow either analytic waveforms or actual road profiles is useful for combining clinical studies of damper behavior with realistic assessments of overall performance. A quarter-car mockup such as employed here seems entirely suited to all initial examinations of ER suspension dampers.

Finally, while this study borrowed from the extensive literature on semiactive suspension control, it did serve to illustrate the merits of the broad bandwidth capability of ER technology for the implementation of one of the more attractive semiactive suspension algorithms, skyhook damping. The very high speed response of ER fluids does, indeed, offer a powerful mechanism for implementing the rapid switching within individual cycles which skyhook damping requires.

9. References

Alanoly, J., and Sankar, S., 1987, "A new concept in semiactive vibration isolation," *Journal of Mechanisms, Transmissions, and Automation in Design*, Vol. 109, pp. 242-247.

Cho, D., and Hedrick, J. K., 1985, "Pneumatic actuators for vehicle active suspension applications," *Journal of Dynamic Systems, Measurement and Control*, Vol. 107, pp. 67-72.

Coulter, J. P., 1993, "An investigation of electrorheological material based controllable damping devices," *The Fluids Engineering Conference: Electrorheological Flows -1993*, Siginer, D. A., Kim, J. H., and Bajura, R. A., ed., FED-Vol. 164, ASME, New York, pp. 143-156.

Crolla, D. A., Horton, D. N. L., Pitcher, R. H., and Lines, J. A., 1987, "Active suspension control for an off-road vehicle," *Proceedings of Institution of Mechanical Engineers*, Vol. 201, pp. 1-10.

Hamilton, J. M., 1985, "Computer optimized adaptive suspension technology (COAST)," *IEEE Transaction on Industrial Electronics*, Vol. IE-32, pp. 355-363.

Hrovat, D., Hubbard, M., and Margolis, D. L., 1980, "Suboptimal semiactive vehicle suspensions," *Proceedings of Joint Automatic Control Conference*, pp. WA10-H.

Inagaki, S., Inoue, H., Sato, S., Tabata, M., and Kokubo, K., 1992, "Development of feedforward control algorithms for active suspension," Paper No. 920270, SAE, Inc., Warrendale, PA.

Karnopp, D., 1987, 'Force generation in semiactive suspensions using modulated dissipative elements," *Vehicle System Dynamics*, Vol. 16, pp. 333-343.

Karnopp, D., 1990, "Design principles for vibration control systems using semiactive dampers," *Journal of Dynamic Systems, Measurement and Control*, Vol. 112, pp. 448-55.

Karnopp, D., Crosky, M. J., and Harwood, R. A., 1974, "Vibration control using semiactive force generators," *Journal of Engineering for Industry, Transactions of the American Society of Mechanical Engineers*, no. 96, pp. 619-626.

Karnopp, D., and Heess, G., 1991, "Electronically controllable vehicle suspensions," *Vehicle System Dynamics*, Vol. 20, pp. 207-217.

Katsuda, T., Hiraiwa, N., Doi, S., and Yasuda, E., 1992, "Improvement of ride comfort by continuously controlled damper," Paper No. 920276, SAE, Inc., Warrendale, PA.

Kimbrough, S., 1986, "Bilinear modelling and regulation of variable component suspensions," *ASME Monograph*, Vol. AMD-80, DSC-2.

Krasnicki, E. J., 1980a, "Comparison of analytical and experimental results for a semiactive vibration isolator," The Shock and Vibration Bulletin, Vol. 50, The Shock and Vibration Information Center, Naval Research Laboratory, Washington D.C.

Krasnicki, E. J., 1980b, "The experimental performance of an 'on-off' active damper," *The Shock and Vibration Bulletin*, Vol. 51, The Shock and Vibration Information Center, Naval Research Laboratory, Washington D.C.

Lou, Z., Ervin, R. D., and Filisko, F. E., 1990, "The feasibility of using electro-rheological fluids in aircraft flight controls-Phase 1 report," UMTRI-90-10, The University of Michigan Transportation Research Institute, Ann Arbor.

Lou, Z., Ervin, R. D., and Filisko, F. E., 1992, "Behaviors of electrorheological valves and bridges," *Proceedings of the International Conference on Electrorheological Fluids: Mechanism, Properties, Structure, Technology, and Applications*, Tao, R., ed., World Scientific, River Edge, NJ, pp. 398-423.

Lou, Z., Ervin, R. D., and Filisko, F. E., 1993, "The influence of viscometer dynamics on the characterization of an electrorheological fluid under sinusoidal electric excitation," *Journal of Rheology*, Vol. 37, pp. 55-70.

Margolis, D. L., 1982, "Semiactive heave and pitch control for ground vehicles," *Vehicle System Dynamics*, Vol. 11, pp. 31-42.

Margolis, D. L., 1983, "Semiactive control of wheel hop in ground vehicles," *Vehicle System Dynamics*, Vol. 12, pp. 317-330.

Margolis, D. L., and Goshtasbpour, M., 1984, "The chatter of semiactive on-off suspensions and its cure," *Vehicle System Dynamics*, Vol. 13, pp. 129-144.

Mizuguchi, M., Suda, T., Chikamori, S., and Kobayashi, K., 1984, "Chassis electronic control systems for the Mitsubishi 1984 Galant," Paper No. 840341, SAE, Inc., Warrendale, PA.

Petek, N. K., 1992, "An electronically controlled shock absorber using electrorheological fluid," Paper No. 920275, SAE, Inc., Warrendale, PA.

Pinkos, A., Shtarkman, E. M., and Fitzgerald, T., 1993, "An actively damped passenger car suspension system with low voltage electro-rheological magnetic fluid," SAE Paper No. 930268, SAE, Inc., Warrendale, PA.

Pollard, M. G., and Simons, N. J. A., 1984, "Passenger comfort-the role of active suspensions," *Proceedings of Institution of Mechanical Engineers*, Vol. 198D, pp. 1-15.

Redfield, R. C., 1991, "Performance of low-bandwidth, semiactive damping concepts for suspension control," *Vehicle System Dynamics*, Vol. 20, pp. 245-267.

Sharp, R. S., and Crolla, D. A., 1987a, "Intelligent suspensions for road vehicles - current and future developments," *Procedings of the European Automobile Engineers Cooperation. International Conference on New Developments in Power Train and Chassis Engineering*, Vol 2, pp. 579-601.

Sharp, R. S., and Crolla, D. A., 1987b, "Road vehicle suspension system design - a review," *Vehicle System Dynamics*, Vol. 16, pp. 167-192.

Venhovens, Paul J. Th., 1994, "Optimal control of vehicle suspensions," PhD thesis, Delft University of Technology, Faculty of Mechanical Engineering, pp. 69-84.

APPENDIX A:
An Analysis of Electrorheological Dampers

This appendix is a is a reprint of a paper entitled "A preliminary parametric study of electrorheological dampers" presented by Lou, Ervin and Filisko at the 1993 summer meeting of the American Society of Mechanical Engineers in Washington, D.C. It presents the analysis which shows the superiority of the shear mode of ER fluid operation in the automotive damper application.

A PRELIMINARY PARAMETRIC STUDY OF ELECTRORHEOLOGICAL DAMPERS

Zheng Lou*, Robert D. Ervin*, and Frank E. Filisko**

*Transportation Research Institute
The University of Michigan, Ann Arbor, MI 48109

** Material Science and Engineering Department
The University of Michigan, Ann Arbor, MI 48109

ABSTRACT

In approaching the design of an electrorheology-based, semi-active suspension, the electrorheological component (ER damper) can be built as either a flow-mode, shear-mode, or mixed-mode type of damper. The source of damping force in the flow-mode is exclusively from flow-induced pressure drop across a valve, while that in the shear-mode is purely from the shear stress on a sliding surface. The dynamics of the fluid flow is included in the derivation of the zero-field damping forces. The control effectiveness is found to be strongly related to the dynamic constant (which is proportional to the square root of the vibration frequency) and, for shear- and flow-mode dampers, the ratio of the piston area to the cross-section of the ER control gap. To achieve the same performance, a flow-mode ER damper is not as compact and efficient as a shear-mode ER damper. With the same ER damping force, a mixed-mode damper is more compact than a shear-mode damper. However, the mixed-mode damper does not have as a low zero-field damping force as the shear-mode damper.

NOMENCLATURE

A_c charged area.
A_{cf}, A_{cm}, and A_{cs} the flow-, mixed-, and shear-mode charged areas.
A_{ER} cross-section area of an ER valve.
A_p cross-section area of a piston.
A_1, A_2, A_3, A_4, A_{1um}, A_{2um}, A_{1om}, and A_{2om} some intermediate variables.
C the electric capacitance of a damper.
C_d the electric current density of an ER fluid.
C_h: an intermediate variable.
D_h: an intermediate variable.
E_p peak electric field strength.
F_{om} the total zero-field damping force in a mixed-mode damper.
F_{ERf} the ER damping force in a flow-mode damper.
F_{ERm} the ER damping force in a mixed-mode damper.
F_{ERs} the ER damping force in a shear-mode damper.
F_u the zero-field (upper-plate) damping force in a shear-mode damper.
f_{of} the zero-field factor of a flow-mode damper.
f_{om} the zero-field factor of a mixed-mode damper.
f_{os} the zero-field factor of a shear-mode damper.

g_l the dynamic factor of the lower-plate stress of a shear-mode damper.

g_m the dynamic factor of Δp_m

g_o the dynamic factor of a flow-mode damper

g_{om} the dynamic factor of a mixed-mode damper

g_u the dynamic factor of (the upper-plate stress of) a shear-mode damper.

g_{um} the dynamic factor of the upper-plate stress of a mixed-mode damper.

g_w the dynamic factor of Δp_w.

h the gap size of an ER valve or gap.

h^* the dynamic constant.

L the length of an ER valve or gap.

P_{cp} the peak capacitive electric power.

P_{rp} the peak resistive electric power.

t the time.

V_c charged volume.

V_{cf}, V_{cm}, and V_{cs} the flow-, mixed-, and shear-mode charged volumes.

v the piston velocity.

v_p the amplitude of v.

w the width of an ER valve or gap.

x_p the amplitude of the piston displacement.

Δp_{ER} the ER pressure drop.

Δp_m the pressure drop component induced by fluid inertia.

Δp_o the zero-field pressure drop in a flow-mode damper.

Δp_s the zero-field pressure drop for an equivalent steady flow of the same flow amplitude.

Δp_w the pressure drop component induced by the wall shear stress.

ε the dielectric constant of an ER fluid.

ϕ_l the phase advance of the lower-plate stress of a shear-mode damper.

ϕ_o the phase advance of a flow-mode damper.

ϕ_{om} the phase advance of a mixed-mode damper.

ϕ_u the phase advance of (the upper-plate stress of) a shear-mode damper.

ϕ_{um} the phase advance of the upper-plate stress of a mixed-mode damper.

ϕ_w the phase advance of Δp_w.

η the zero-field or plastic viscosity.

ρ the density of an ER fluid.

τ_l the lower-plate shear stress of a shear-mode damper.

τ_o equivalent to the zero-field shear stress between two parallel plates, with one of them fixed and the other plate moving at a constant velocity v_p.

τ_u the upper-plate shear stress of a shear-mode damper.

τ_{um} the upper-plate shear stress of a mixed-mode damper.

τ_y the yield stress.

τ_y^* the dimensionless yield stress.

ω the angular velocity of the input vibration.

INTRODUCTION

An electrorheological (ER) damper is a device that is able to generate a controllable damping force by employing an ER fluid. An ER fluid can change its rheological properties, most notably its effective viscosity, within one millisecond when exposed to an electric field. There have been numerous designs of and studies on ER dampers (Brooks, 1989; Bullough and Foxon, 1978; Duclos, 1988; Hartsock *et al.*, 1991; Morishita and Mitsui, 1992; Petek, 1992; Shul'man *et al.*, 1987; Stanway *et al.*, 1989; Stanway *et al.*, 1987; Stevens *et al.*, 1984). The wide range and the high bandwidth of the effective viscosity variation of ER fluids are two of the primary factors that have caused intense research and development activities in ER dampers.

Despite the appearance of various new rheological models of ER fluids (Gamota and Filisko, 1991; Jordan *et al.*, 1992; Rajagopal and Wineman, 1992), the Bingham model remains attractive

owing to its simplicity and effectiveness (without significant loss in accuracy) in describing macroscopic engineering problems. Viscoelastic fluid model has also been used in modeling ER dampers (Shul'man *et al.*, 1987).

Based on the Bingham model, Stevens *et al.* (1984) and Stanway *et al.* (1987) assigned two terms to the damping force of an ER damper, with one of them (a linear viscous damping) associated with the plastic viscosity and the other (a Coulomb friction) with the Bingham or yield stress. This Coulomb friction approach did not quite fit experimental data, and a power law model was developed later (Stanway *et al.*, 1989). In the power law model, the amplitude of the damping force is proportional to the absolute value of the damper velocity to the n^{th} power. The results were still not satisfactory even with the proportional coefficient and exponent being adjustable.

The ER damper studies so far have generally ignored the influence of the fluid dynamics, i.e., the unsteady nature of the fluid velocity, shear rates, and thus the damping force, which are all induced by the inertia of the fluid. Lou *et al.* (1992) have shown that the fluid inertia can limit the bandwidth of an ER valve to a level far below that the bandwidth of the rheological variation of an ER fluid. Similar influence exists in ER dampers, many of which contain ER valves.

Electrorheological dampers can be classified as: flow-mode (Fig. 1a), mixed-mode (Fig. 1b), and shear-mode (Fig. 1c). The configurations illustrated in Fig. 1 are essentially generic concepts that contain simplified features to facilitate the design analysis. In practical hardware, for example, the cylinder is likely to be single, rather than double-ended, and the ER control valve or area is likely to be comprised of multiple parallel or concentric plates. Among the three conceptual modes, the flow-mode damper is most similar to the traditional shock absorber except that it replaces the conventional orifice with an ER control gap or valve. The source of the damping force in this mode is exclusively from flow-induced pressure drop across the piston. The ER valve can be placed outside the cylinder (as in Fig. 1a) or within the piston component. For the sake of compact packaging, the external approach could be implemented by forming a flow chamber along the outside of the cylinder wall (Petek, 1992).

In the mixed-mode damper, the ER control is realized in the gap between the piston sidewall and the cylinder liner. The fluid shear stress at the shear surface also contributes to the damping force, while the flow-induced pressure drop is still present as a force component on the piston.

If a large by-pass port is cut through the piston of a mixed-mode damper, the device becomes a simple shear-mode element. Since the fluid can flow freely through the by-pass, the pressure drop across the piston becomes negligible and only shear stresses developed along the wall contribute to the damping force.

The purpose of this study is to systematically analyze the dynamic performances of all three modes of ER dampers. Special attention is paid to (a) the relative magnitudes of the zero-field and ER components of the damping force under dynamic situation and (b) and their implication in the sizing and selection of the damping mode. For simplicity, ER fluids are assumed to be Bingham plastic. In cases where ER fluids are not of Bingham type, the assumption here will not result in significant errors for practical dampers that far out-stroke the elastic strain range and/or the low shear rate range.

ANALYSIS

Flow-Mode Dampers

If the vibration of the piston (Fig. 1a) can be described as

$$v = v_p \sin \omega t = \omega x_p \sin \omega t \tag{1}$$

where v is the piston velocity, v_p the amplitude of v, ω the angular velocity, t the time, and x_p the amplitude of the piston displacement. From continuity, the amplitude of the (space-wise) mean velocity of the ER fluid in the ER valve is $(A_P/A_{ER})x_p\omega$, where A_P is the cross-section area of the piston, and A_{ER} is the cross-section area of the ER valve. The zero-field (i.e., with electrical field strength equal to zero) pressure drop for an equivalent steady flow of the same flow amplitude is

$$\Delta p_s = 12\eta \frac{L}{h^2} \frac{A_P}{A_{ER}} x_p \omega \tag{2}$$

where L and h are the length and gap size of the ER valve, respectively. The parameter η is the zero-field or plastic viscosity, which is assumed to be Newtonian although certain non-Newtonian behavior has been reported (Lou *et al.*, 1990). This pressure drop, frequently used in the literature, does not account for the effect of the dynamics of a sinusoidal flow.

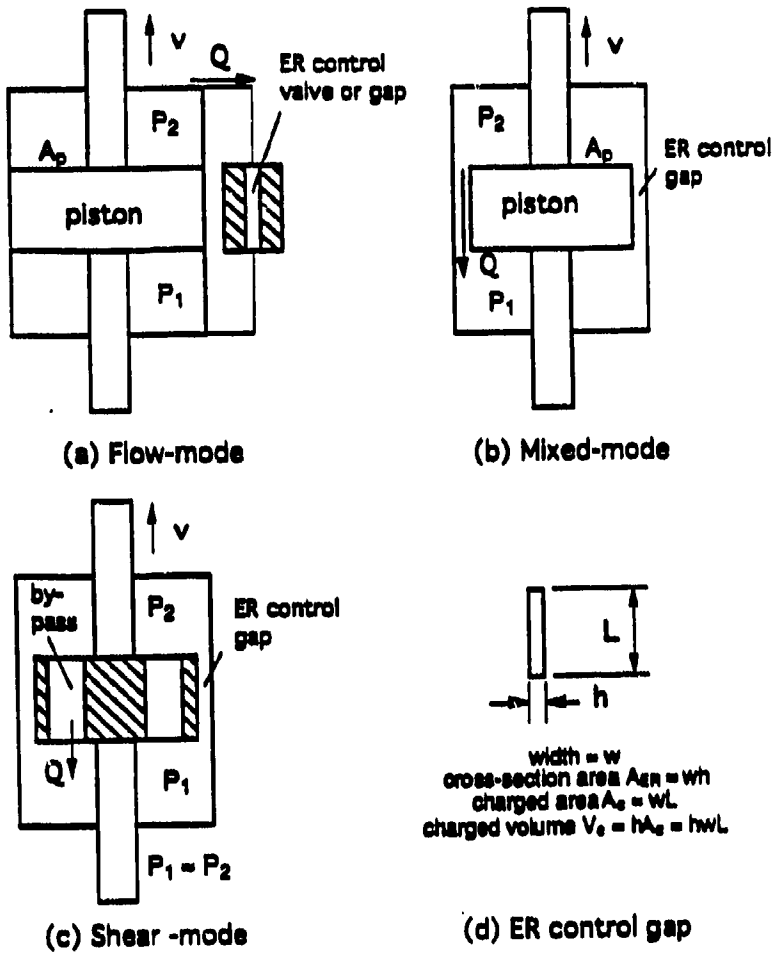

Fig. 1. The generic concepts of the three modes of electrorheological dampers.

A dynamic pressure drop has a component induced by fluid inertia:

$$\Delta p_m = g_m \Delta p_s \sin(\omega t + \frac{\pi}{2}) \tag{3}$$

with

$$g_m = \frac{2}{3} h^{*2} \tag{4}$$

$$h^* = \frac{h}{2}\sqrt{\frac{\rho\omega}{2\eta}} \tag{5}$$

where ρ is the density of the ER fluid. The dimensionless parameter h^* is, if ignoring the constant $2\sqrt{2}$, the ratio of the gap size h to the parameter group $\sqrt{\eta/\rho\omega}$. The latter has the dimensions of length. It is related to the location of an overshoot in the mean velocity of an oscillatory flow in a flow-mode damper or to the penetration depth of an oscillatory shear flow in a shear-mode damper. One can thus consider h^* as a dimensionless gap size. The parameter h^* and its variations are called, in the literature, the Womersley number or dynamic constant or dimensionless frequency because of the existence of the frequency ω. They are also related to the ratio of the time constant of the flow (which depends on the gap size and the fluid kinematic viscosity) to the period of the forcing function (Lou and Yang, 1993). In this study, h^* is to be called the dynamic constant instead of the

dimensionless gap size because (a) the parameter appears only in a dynamic situation, (b) the practical gap size is generally in a narrow range around 1 mm, and (c) the frequency ω changes greatly in most ER fluid applications.

The function g_m, called the dynamic factor of Δp_m, is 0 at $h^* = 0$ and rises proportionally with h^{*2} (or with ω if other parameters in h^* is fixed). Physically, the ratio of the amplitude of the inertia component of the dynamic pressure to the equivalent steady pressure drop is proportional to the frequency.

The dynamic pressure drop has another component that is induced by the wall shear stress:

$$\Delta p_w = g_w \Delta p_s \sin(\omega t + \phi_w) \tag{6}$$

with

$$g_w = \frac{2}{3} h^* \frac{[(2C_h - C_h^2 - D_h^2)^2 + 4D_h^2]^{1/2}}{(2 - C_h)^2 + D_h^2} \tag{7}$$

$$\phi_w = \frac{\pi}{2} + \tan^{-1}[2D_h/(2C_h - C_h^2 - D_h^2)] \tag{8}$$

$$C_h = \frac{\sin h^* \cos h^* + \sinh h^* \cosh h^*}{h^*[(\cosh h^* \cos h^*)^2 + (\sinh h^* \sin h^*)^2]} \tag{9}$$

$$D_h = \frac{\sin h^* \cos h^* - \sinh h^* \cosh h^*}{h^*[(\cosh h^* \cos h^*)^2 + (\sinh h^* \sin h^*)^2]} \tag{10}$$

The function g_w, called the dynamic factor of Δp_w, starts from 1.0 at $h^* = 0$, increases with h^* slightly until about $h^* = 1$, and, then, rises almost proportionally with h^* (or with $\sqrt{\omega}$ if other parameters in h^* is fixed). Physically, the amplitude of the dynamic wall shear stress is approximately equal to that of the equivalent steady shear stress at low frequencies and grows larger at high frequencies.

The zero-field dynamic pressure drop, the summation of its two components Δp_w and Δp_m, is:

$$\Delta p_o = g_o \Delta p_s \sin(\omega t + \phi_o) \tag{11}$$

with

$$g_o = \frac{4h^{*2}}{3[(2 - C_h)^2 + D_h^2]^{1/2}} \tag{12}$$

$$\phi_o = \frac{\pi}{2} + \tan^{-1}[D_h/(2 - C_h)] \tag{13}$$

where g_o and ϕ_o are the dynamic factor and the phase advance of the flow-mode damper, respectively. The primary value of g_o is from g_w at low frequencies and from g_m at high frequencies. The factor g_o remains close to one at low frequencies and rises proportionally with h^{*2} (Fig. 2). Physically, the zero-field dynamic pressure drop is mainly to overcome the wall stress and the fluid inertia at low and high frequencies, respectively. The phase advance ϕ_o is 0 at $h^* = 0$ (steady state), 45° at about $h^* = 1$, and 90° as h^* approaches infinite.

The above analysis has been for the zero-field situation. With the application of an electric field, an yield stress is induced in the ER fluid. For a steady Couette flow within a narrow gap, the yield stress and the zero-field shear stress can be superposed. The linear summation is no longer valid under dynamic conditions and a precise solution can be obtained only by solving the fluid dynamic equation (Lou *et al.*, 1993a). Analytical solutions for a dynamic Bingham fluid flow are not readily available, while numerical solutions are generally time-consuming and not as insightful. For a preliminary engineering parametric study, a simplified, linear analytical approach is adopted here.

The ER pressure drop Δp_{ER} is estimated to be

$$\Delta p_{ER} = 2\frac{L}{h}\tau_y \tag{14}$$

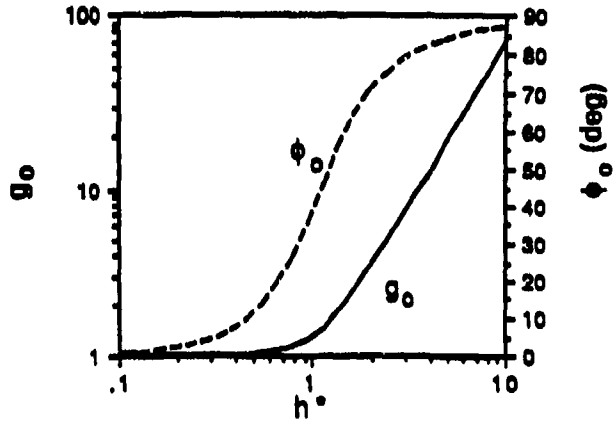

Fig. 2. The dynamic factor g_o and the phase advance ϕ_o of the zero-field pressure drop versus the dynamic constant h^*.

where τ_y is the yield stress. The ratio of the zero-field pressure drop to the ER pressure drop is derived as

$$\frac{\Delta p_o}{\Delta p_{ER}} = f_{of} \sin(\omega t + \phi_o) \tag{15}$$

with

$$f_{of} = 6 \frac{A_p}{A_{ER}} \frac{g_o}{\tau_y^*} \tag{16}$$

$$\tau_y^* = \frac{\tau_y}{\tau_o} \tag{17}$$

$$\tau_o = \eta \frac{v_p}{h} \tag{18}$$

where f_{of} is the zero-field factor of the flow-mode damper, which is a relative measure of the zero-field pressure drop. For the ER damper to be effective, the zero-field factor f_{of} has to be much less than one. The new parameter τ_y^* is a dimensionless yield stress; τ_o is equivalent to the zero-field shear stress between two parallel plates, with one of them fixed and the other plate moving at a constant velocity v_p.

The ER damping force on the piston of the flow-mode damper is calculated as

$$F_{ERf} = 2 \frac{L}{h} A_p \tau_y \tag{19}$$

and it has to be able match the designed peak damping force of the damper. The compactness and efficiency of the device are important as well. The charged area A_c (where the charged electrodes face each other) is calculated as

$$A_c = wL \tag{20}$$

where w is the width of the ER valve. The charged volume V_c (i.e., the volume between the charged electrodes) is calculated as

$$V_c = hA_c = wLh. \tag{21}$$

The charged area A_c is related to the electric capacitance of the damper C by the equation

$$C = \varepsilon \frac{A_c}{h} \tag{22}$$

where ε is the dielectric constant of the ER fluid. Assuming a sinusoidal electric field strength with a peak value of E_p, one obtains the following peak capacitive electric power P_{cp} and peak resistive electric power P_{rp}, respectively,

$$P_{cp} = \frac{1}{2}\varepsilon\omega E_p^2 V_e \tag{23}$$

and

$$P_{rp} = C_d E_p V_e \tag{24}$$

where C_d is the electric current density.

Shear-Mode Dampers

A practical shear-mode damper has a narrow gap whether it has a concentric or parallel arrangement of its electrodes. The fluid flow in a small gap can be approximated with an one-dimensional flow between two infinite parallel plates, with one plate (denoted arbitrarily as the lower-plate here) fixed and the other plate (the upper-plate) oscillating in its plane with a velocity

$$v = v_p \sin \omega t \tag{25}$$

Adapting the solutions from the literature (Schrag *et al.*, 1965) to the current arrangement and a Newtonian fluid (i.e. with zero-field), the shear stress at the upper-plate τ_u is derived as

$$\tau_u = g_u \tau_o \sin(\omega t + \phi_u) \tag{26}$$

with

$$g_u = 2\sqrt{2}h^* \frac{\sqrt{A_1^2 + A_2^2}}{\sqrt{A_3^2 + A_4^2}}, \tag{27}$$

$$\phi_u = \frac{\pi}{4} + \tan^{-1}(A_2/A_1) - \tan^{-1}(A_4/A_3), \tag{28}$$

$$A_1 = \cosh 2h^* \cos 2h^*, \quad A_2 = \sinh 2h^* \sin 2h^*,$$
$$A_3 = \sinh 2h^* \cos 2h^*, \quad \text{and} \quad A_4 = \cosh 2h^* \sin 2h^* \tag{29}$$

where g_u and ϕ_u are the dynamic factor and the phase advance of (the upper-plate stress of) the shear-mode damper, respectively. The dynamic factor g_u is approximately equal to 1 when $h^* < 0.5$ and equal to $2\sqrt{2}\ h^*$ when $h^* > 0.5$ (Fig. 3). Therefore, the upper-plate shear stress increases with the dynamic constant h^*.

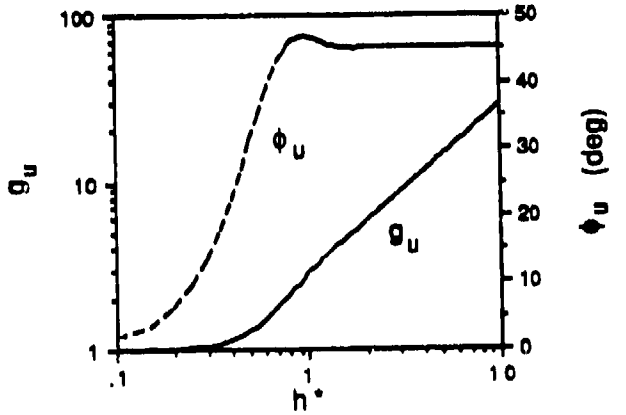

Fig. 3. The dynamic factor (g_u) and the phase advance (ϕ_u) of the upper-plate shear stress of the shear-mode damper.

The lower-plate shear stress τ_l is derived as

$$\tau_l = g_l \tau_o \sin(\omega t + \phi_l) \tag{30}$$

with

$$g_l = 2\sqrt{2}h^* \frac{1}{\sqrt{A_3^2 + A_4^2}} \tag{31}$$

$$\phi_l = \frac{\pi}{4} - \tan^{-1}(A_4/A_3) \tag{32}$$

where g_l and ϕ_l are the dynamic factor and the phase advance of the lower-plate stress of the shear-mode damper, respectively. The dynamic factor g_l is approximately equal to 1 when $h^* < 0.5$ and approaches 0 at high h^* values (Fig. 4). Therefore, the lower-plate shear stress decreases with the dynamic constant h^*. During a high-frequency oscillation, the shear wave does not fully reaches the lower-plate, and the majority of the energy is dissipated in the fluid volume immediately below to the upper-plate.

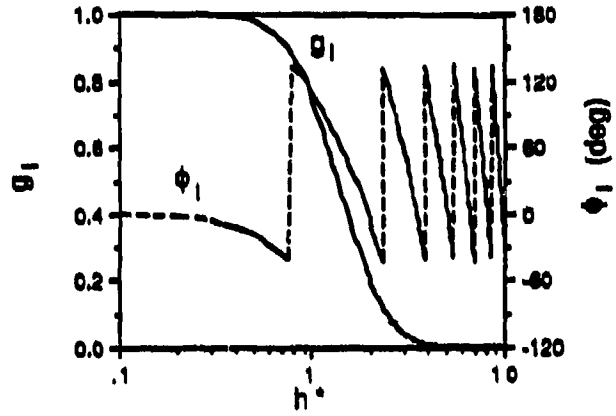

Fig. 4. The dynamic factor (g_l) and the phase advance (ϕ_l) of the lower-plate shear stress of the shear-mode damper.

Analytical solutions for dynamic flow of a Bingham fluid induced by an oscillating plate are not available. Again as in the analysis of the flow-mode damper, a simplified, linear analytical approach is adopted. In the shear-mode damper, no pressure drop is involved, and the damping force is directly related to the shear force on the upper-plate. The ER damping force in the shear-mode damper F_{ERs} is estimated as

$$F_{ERs} = A_{cs}\tau_y. \tag{33}$$

where A_{cs} is the charged area of the shear-mode damper. The zero-field (upper-plate) damping force is

$$F_u = A_{cs}\tau_o g_u \sin(\omega t + \phi_u) \tag{34}$$

The ER damping force F_{ERs} has to be able to match the desired damping force of the system, and the zero-field damping force F_u has to be relatively small. The ratio of the zero-field damping force to the ER damping force is

$$\frac{F_u}{F_{ERs}} = f_{os} \sin(\omega t + \phi_u) \tag{35}$$

with

$$f_{os} = \frac{g_u}{\tau_y^*} \tag{36}$$

where f_{os} is the zero-field factor of the shear-mode damper. For the damper to be effective, f_{os} has to be much less than one.

Shear-mode dampers can be further divided into rotary and translational types, either of which can have its own variations in the way electrodes are arranged.

The damper in Fig. 1c is only one possible version of the translational type of shear-mode dampers, where the electrodes are arranged concentrically. Electrodes can also be parallel plates. Multiple electrodes are generally used to achieve a compact design. Because of the translational motion, the cylinder in Fig. 1c has to be longer than the piston to keep a constant charged area. This results in a significant amount of idling surface on the cylinder at any moment.

A rotary-type shear-mode damper is able to reduce the extra surface area by having all the surface area engaged all the time. One possible version is to have a plurality of rotational shearing disks along the rotation axis (Lou *et al.*, 1993b). An alternative is to have multiple concentric electrodes around the rotation axis. A translation-to-rotation device is needed if the motion to be damped is translational.

Mixed-Mode Dampers

Because of the linear nature of the flow of a Newtonian fluid between two parallel plates, the velocity between the electrodes of a mixed-mode damper can be obtained by superposing those of the corresponding shear- and flow-mode dampers. The shear stress on the upper-plate of a mixed-mode damper τ_{um} is the summation of the shear stresses induced by Couette and Poiseuille flows:

$$\tau_{um} = \tau_o g_{um} \sin(\omega t + \phi_{um}) \tag{37}$$

with

$$g_{um} = \sqrt{A_{1um}^2 + A_{2um}^2} \tag{38}$$

$$\phi_{um} = \tan^{-1}\frac{A_{2um}}{A_{1um}} \tag{39}$$

$$A_{1um} = g_u \cos\phi_u + 6\frac{A_p}{A_{ER}} g_w \cos\phi_w \quad \text{and} \quad A_{2um} = g_u \sin\phi_u + 6\frac{A_p}{A_{ER}} g_w \sin\phi_w. \tag{40}$$

where g_{um} and ϕ_{um} are the dynamic factor and the phase advance of τ_{um}, respectively.

The total zero-field damping force F_{om} is derived as

$$F_{om} = A_p g_o \Delta p_s \sin(\omega t + \phi_o) + A_c g_{um} \tau_o \sin(\omega t + \phi_{um}) \tag{41}$$

and the ER control force F_{ERm} is as follows

$$F_{ERm} = 2\frac{L}{h} A_p \tau_y + A_c \tau_y \tag{42}$$

In either of equations (41) and (42), the first term on the right hand side is the force from the pressure drop, while the second term represent the force on the shearing surface.

The combination of equations (41) and (42) gives

$$\frac{F_{om}}{F_{ERm}} = f_{om} \sin(\omega t + \phi_{om}) \tag{43}$$

with

$$f_{om} = \frac{g_{om}}{\tau_y^*} \tag{44}$$

$$g_{om} = \frac{\sqrt{A_{1om}^2 + A_{2om}^2}}{[2(A_p/A_{ER}) + 1]} \tag{45}$$

$$\phi_{om} = \tan^{-1}\frac{A_{2om}}{A_{1om}} \tag{46}$$

$$A_{1om} = 12(A_p/A_{ER})^2 g_o \cos\phi_o + g_{um} \cos\phi_{um} \tag{47}$$

$$A_{2om} = 12(A_p/A_{ER})^2 g_o \sin\phi_o + g_{um} \sin\phi_{um} \tag{48}$$

where f_{om} is the zero-field factor, g_{om} the dynamic factor, and ϕ_{om} the phase advance of the mixed-mode damper. Both g_{om} and ϕ_{om} increase with h^* (Fig. 5). The dynamic factor g_{om} also increases with A_p/A_{ER} because of the rising dominance of the flow action (Fig. 5a). The phase advance ϕ_{om} decreases with A_p/A_{ER} at low h^* and does the opposite at high h^* (Fig. 5b). A mixed-mode damper becomes a shear-mode damper when A_p/A_{ER} approaches zero, i.e., no more piston area.

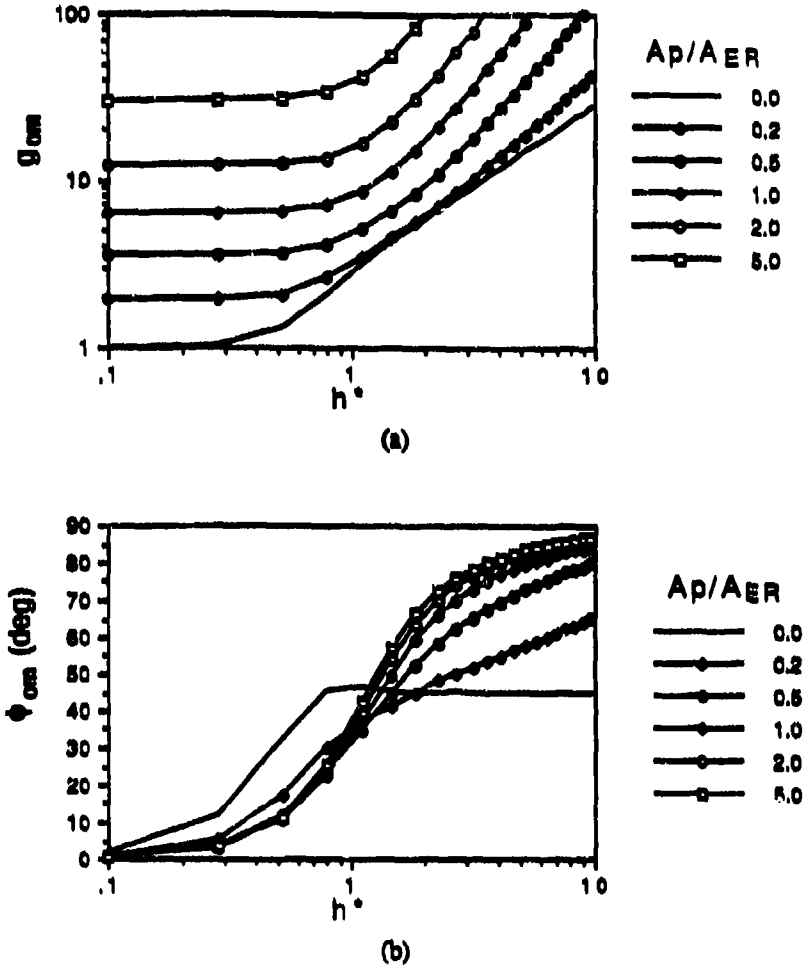

Fig. 5. (a) The dynamic factor g_{om} and (b) the phase advance ϕ_{om} of a mixed-mode damper versus the dynamic constant h^* and the area ratio A_p/A_{ER}.

Flow-mode versus Shear-mode

In active damping control, one likes to generate a large ER damping force and, at the same time, keep the zero-field damping force as small as possible. For the same task, a shear-mode damper and a flow-mode damper therefore should have (a) the same ER damping force and (b) the same zero-field factor value. For the second requirement, one has

$$\frac{f_{of}}{f_{os}} = 1. \tag{49}$$

The substitution of equations (15) and (36) into equation (49) gives

$$A_p = \frac{g_u}{6g_o} A_{ER}. \tag{50}$$

To meet the first requirement, one can derive from equations (19), (20), (33) and (50) the following

$$\frac{V_{cf}}{V_{cs}} = \frac{A_{cf}}{A_{cs}} = \frac{3g_o}{g_u} \tag{51}$$

where V_{cs} is the charged volume of the shear-mode damper, and A_{cf} the charged area of the flow-mode damper. The both dampers are assumed to have the same gap size. The ratio V_{cf}/V_{cs} is a good indicator of relative design merits of the two dampers because the charged volume is directly related to the size (Fig. 1d) and power requirement of a damper as shown in equations (23) and (24). The ratio V_{cf}/V_{cs}, like g_o or g_u, is a function of the dynamic constant h* (see Fig. 6). The ratio V_{cf}/V_{cs} is 3 at $h^* = 0$, decreases gradually to its minimum value of 1.35 around $h^* = 1$, and then increases linearly with h*. To achieve the same performance, the flow-mode ER damper is therefore not as compact and efficient as the shear-mode ER damper.

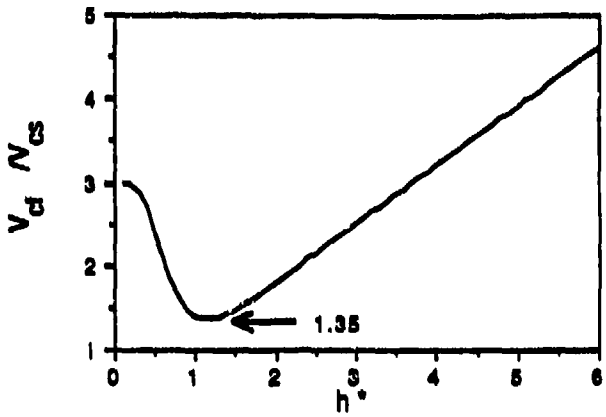

Fig. 6. The ratio of the flow-mode charged volume (V_{cf}) to the shear-mode charged volume (V_{cs}) as a function of the dynamic constant h*.

The significance of the dynamic constant h* is evident in Fig. 6. A practical range of h* is estimated using equation (5) and plotted in Fig. 7, where the fluid density ρ and the gap size h are chosen to be 1000 kg/m^3 and 1 mm, respectively. The frequency ranges from 1 to 1000 Hz, and the plastic viscosity η ranges from 10 to 1000 cP in Fig. 7. In passenger cars, body natural frequencies are 1-2 Hz, the wheelhop frequency is around 15 Hz, and the engine mount natural frequency is 10-20 hz (Morishita and Mitsui, 1992). One thousand hertzs is probably the upper limit of natural frequencies of any practical mechanical system. One hundred centipoises is a middle range value of the zero-field viscosity of ER fluids. For the chosen density and gap size, the dynamic constant h* varies from 0.05 to 5.0. Practical values of ρ and h will not deviate too much from those chosen here, and the range of h* presented in Fig. 7 is fairly representative.

Mixed-mode versus Shear-mode

For the ER damping force of a mixed-mode damper F_{ERm} and that of a shear-mode damper F_{ERs} to be equal, one obtains

$$\frac{V_{cm}}{V_{cs}} = \frac{A_{cm}}{A_{cs}} = \frac{1}{2(A_p/A_{ER}) + 1} \tag{52}$$

where V_{cm} and A_{cm} are the charged volume and area of the mixed-mode damper, respectively. The gap size h is assumed to be the same. With a positive A_p/A_{ER}, the ratio V_{cm}/V_{cs} is less than one. With the same ER damping force, the mixed-mode damper is therefore more compact than the shear-mode damper.

The ratio of the zero-field factor of the mixed-mode damper f_{om} to that of the shear-mode damper f_{os} is equal to g_{om}/g_u because of equations (36) and (44). The ratio f_{om}/f_{os} is a function of the

dynamic constant h* and the area ratio A_p/A_{ER}, and is always greater than one for a positive A_p/A_{ER} (Fig. 8). The mixed-mode damper therefore does not have as a low zero-field damping force as the comparable shear-mode damper.

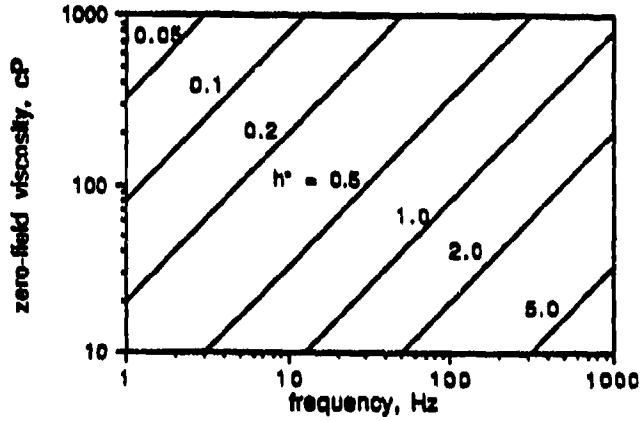

Fig. 7. The dynamic constant h* as a function of the vibration frequency (= $\omega/2\pi$) and the zero-field viscosity (η), with the ER control gap size h = 1 mm and the ER fluid density ρ = 1000 kg/m³.

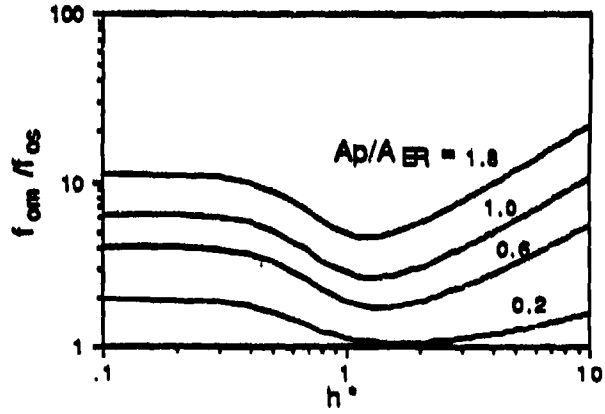

Fig. 8. The ratio of the zero-field factor of the mixed-mode damper f_{om} to that of the shear-mode damper f_{os} as a function of the dynamic constant h* and the area ratio A_p/A_{ER}.

DISCUSSIONS

The primary message from the above analysis is: to avoid the flow-mode and to use the shear-mode. There are two physical reasons for the message. First, with a limited ER induced increase in the shear stress (i.e., τ_y), a device should operate at as a low shear rate as possible to reduce the zero-field damping force and increase its effective control. It is quite often that the yield stress even decreases with the shear rate, which further enhances the need for a low shear rate. Second, the fluid inertia and the unsteady wall shear stress (which is higher than the steady wall shear stress) significantly increase the zero-field damping force. A flow-mode damper generally has higher shear rate and acceleration, especially with a large A_p/A_{ER}, than a shear-mode damper.

In the analysis, the cylinder component of a damper is fixed while the piston component vibrates. Both the components of many practical dampers can move. In most of these cases, there is a large disparity in the amplitudes of the motion for the two components, and the analysis in this study is valid. Otherwise, more appropriate boundary conditions have to be used for a finer analysis although the general conclusion from this study may still apply, at least to the first order accuracy.

For the purpose of generality, the assigned vibration in this study is sinusoidal. Road surface profiles for an automobile damper, for example, is not so. Through the use of the power spectral density function, however, one can present the surface profiles in forms of sine wave.

CONCLUSIONS

In this study, the dynamics of the fluid flow is included in the derivation of the zero-field damping forces of the flow-, shear-, and fixed-mode ER dampers. The main results of the study are as follows:

- The zero-field pressure drop in a flow-mode damper is mainly to overcome the wall shear stress at low frequencies. At high frequencies (with the dynamic constant h^* greater than one), the zero-field pressure counters primarily the fluid inertia, and it increases with the frequency or h^{*2}. It also has a significant phase advance relative to the vibration at high frequencies. The level of ER control decreases with the ratio of the piston area to the ER valve cross-section A_p/A_{ER}.
- The zero-field pressure drop in a shear-mode damper also has to counter the fluid inertia at high frequencies. When the dynamic constant h^* is greater than 0.5, the zero-field pressure increases with h^* or the square root of the frequency.
- The behavior of the zero-field pressure drop in a mixed-mode damper is between those of a shear- and a flow-mode damper, and it is a function of the area ratio A_p/A_{ER}. The mixed-mode damper becomes a shear-mode damper when the ratio A_p/A_{ER} approaches zero.
- To achieve the same performance, a flow-mode ER damper is not as compact and efficient as a shear-mode ER damper.
- With the same ER damping force, a mixed-mode damper is more compact than a shear-mode damper. However, the mixed-mode damper does not have as a low zero-field damping force as the shear-mode damper.

ACKNOWLEDGMENTS

The authors wish to acknowledge the financial support from the NASA-Langley Research Center, the U.S. Army Tank-Automotive Command (TACOM), Aeroquip Corporation, BASF, Chrysler Corporation, Ford Motor Company, Monroe Automotive Equipment Co., Naval Underwater Systems Center, Nissan Motors, and Tremec Trading Company.

REFERENCES

Brooks, D., 1989, "Fluids get tough," *Physics World*, Vol. 2, pp. 35-38.

Bullough, W. A., and Foxon, M. B., 1978, "A proportionate Coulomb and viscously damped isolation system," *Journal of Sound and Vibration*, Vol. 56, pp. 35-44.

Duclos, T. G., 1988, "Design of devices using electrorheological fluids," No.881134, SAE, Warrendale, PA.

Gamota, D., and Filisko, F. E., 1991, "Dynamic mechanical studies of electrorheological materials: Moderate frequencies," *Journal of Rheology*, Vol. 35, pp. 399-425.

Hartsock, D. L., Novak, R. F., and Chaundy, G. J., 1991, "ER fluid requirements for automotive devices," *Journal of Rheology*, Vol. 35, pp. 1305-1326.

Jordan, T. C., Shaw, M. T., and McLeish, T. C. B., 1992, "Viscoelastic response of electrorheolgoical fluids. II. Field strength and strain dependence," *Journal of Rheology*, Vol. 36, pp. 441-464.

Lou, Z., Ervin, R. D., and Filisko, F. E., 1990, "The feasibility of using electro-rheological fluids in aircraft flight controls-Phase 1 report," UMTRI-90-10, The University of Michigan Transportation Research Institute.

Lou, Z., Ervin, R. D., and Filisko, F. E., 1992, "Behaviors of electrorheological valves and bridges," *Proceedings of the International Conference on Electrorheological Fluids: Mechanism, Properties, Structure, Technology, and Applications*, Tao, R., ed., World Scientific, River Edge, NJ, pp. 398-423.

Lou, Z., Ervin, R. D., and Filisko, F. E., 1993a, "The influence of viscometer dynamics on the characterization of an electrorheological fluid under sinusoidal electric excitation," *Journal of Rheology*, Vol. 37, pp. 55-70.

Lou, Z., Ervin, R. D., Filisko, F. E., and Winkler, C. B., 1993b, "An electrorheologically controlled semi-active landing gear," SAE Technical Paper Series (in-press), SAE,

Warrendale, PA. 1993 SAE Aerospace Atlantic Conference & Exposition, April 20-23, Dayton, Ohio.

Lou, Z., and Yang, W. J., 1993, "A computer simulation of the non-Newtonian blood flow at the aortic bifurcation," *Journal of Biomechanics*, Vol. 26, pp. 37-49.

Morishita, S., and Mitsui, J., 1992, "An electoronically controlled engine mount using electro-rheological fluid," Pub. No. 922290, SAE, Inc., Warrendale, PA.

Petek, N. K., 1992, "An electronically controlled shock absorber using electrorheological fluid," Pub. No. 920275, SAE, Inc., Warrendale, PA.

Rajagopal, K. R., and Wineman, A. S., 1992, "Flow of electro-rheological materials," *Acta Mechanica*, Vol. 91, pp. 57-75.

Schrag, J. L., Guess, J. F., and Thurston, G. B., 1965, "Shear-wave interference observed by optical birefringence induced in a viscous liquid," *Journal of Applied Physics*, Vol. 36, pp. 1996-2000.

Shul'man, Z. P., Khusid, B. M., Khizh'nskii, B. P., and Korobko, E. V., 1987, "Characteristics of an electrorheological damper in a vibration insulator," Vol. 52, pp. 237-44.

Stanway, R., Sproston, J., and Firoozian, R., 1989, "Identification of the damping law of an electro-rheological fluid: A sequential filtering approach," *Journal of Dynamic Systems, Measurement and Control*, Vol. 111, pp. 91-96.

Stanway, R., Sproston, J. L., and Stevens, N. G., 1987, "Non-linear modeling of an electro-rheological vibration damper," *Journal of Electrostatics*, Vol. 20, pp. 167-184.

Stevens, N. G., Sproston, J. L., and Stanway, R., 1984, "Experimental evaluation of a simple electroviscous damper," Vol. 15, pp. 275-283.

APPENDIX B:
Drawings of the ER Damper for the HMMWV

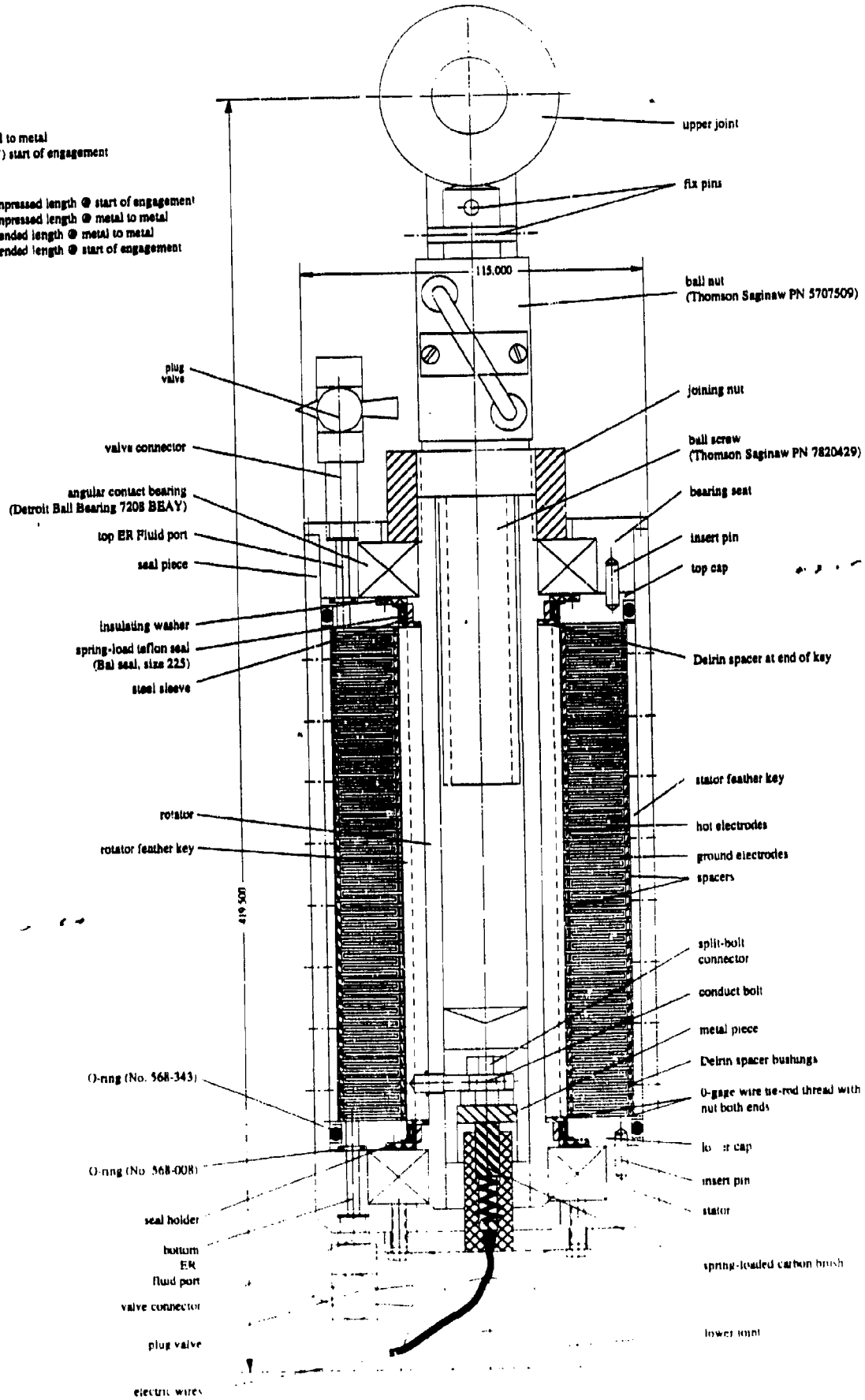

EP Damper Assembly

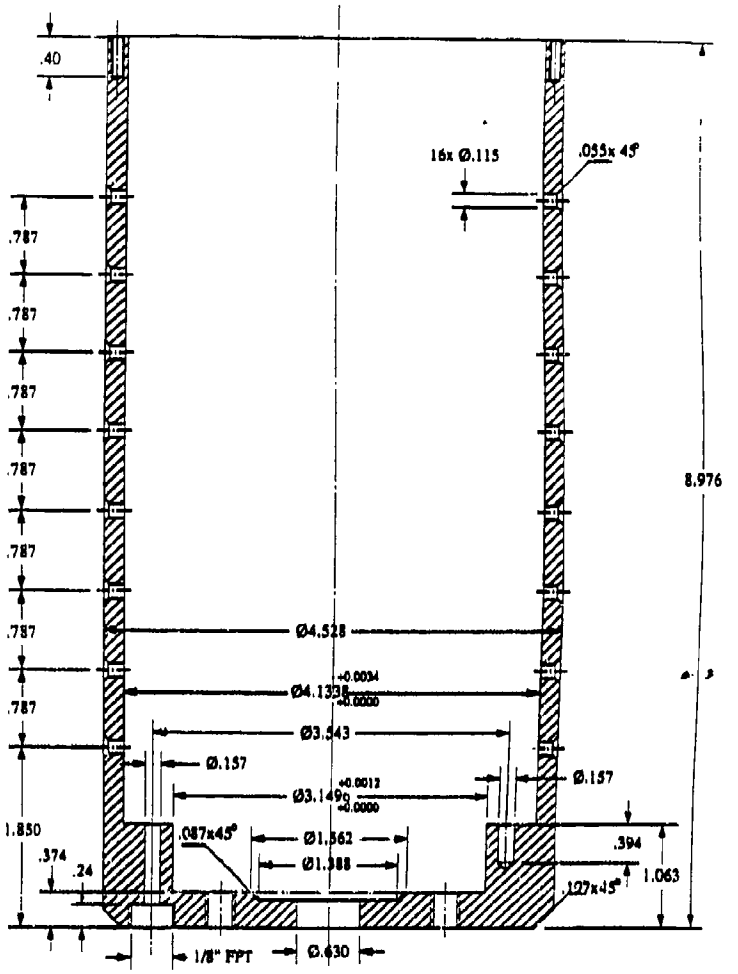

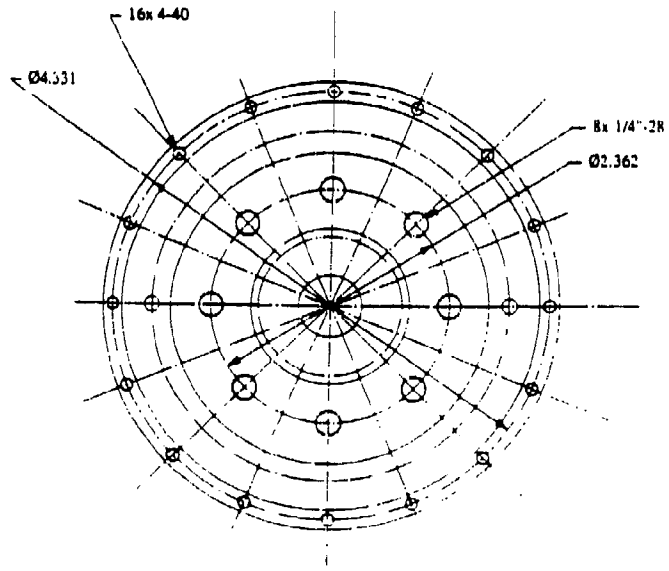

Stator	303 Stainless steel	1
Part name	Material	Qty

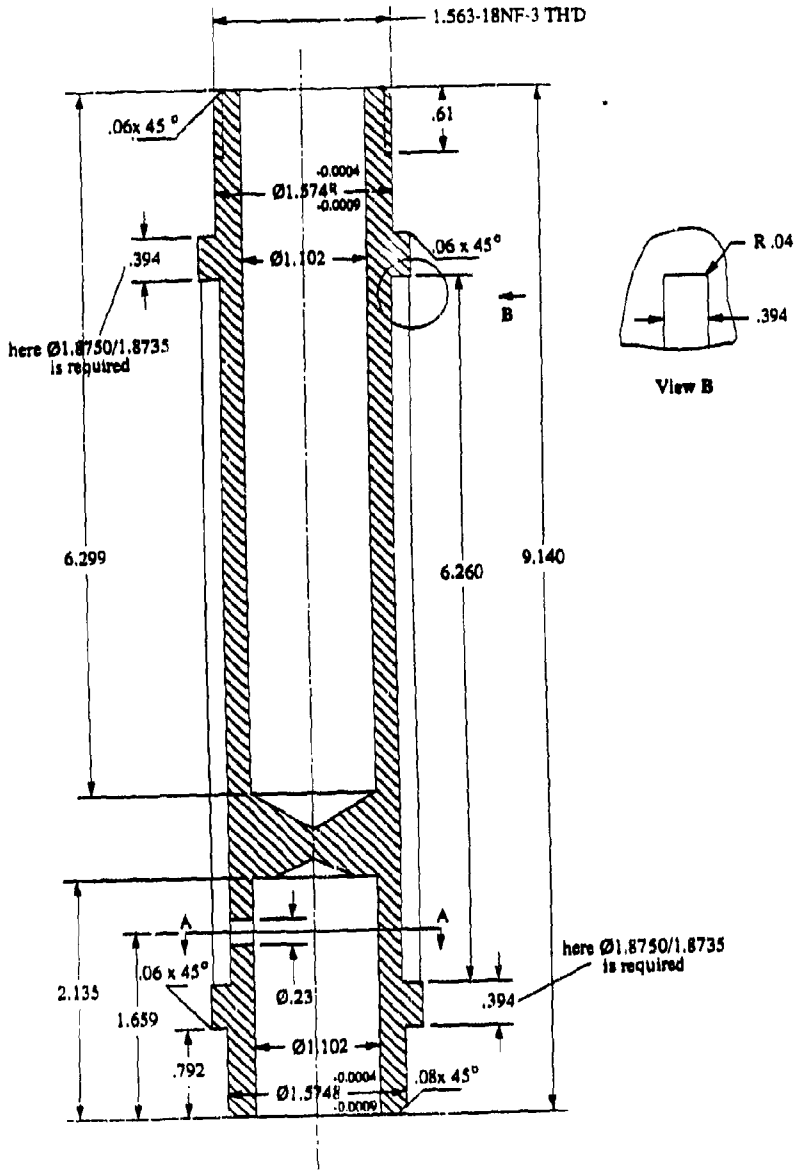

View B

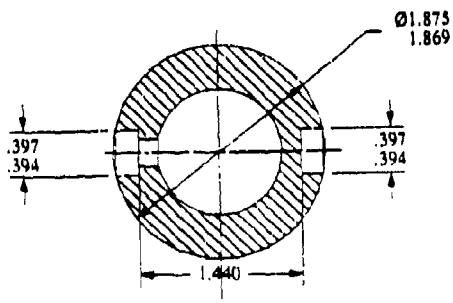

View A-A

All corners R 0.02

Part name	Material	Qty
Rotator	Glass epoxy G-11	1

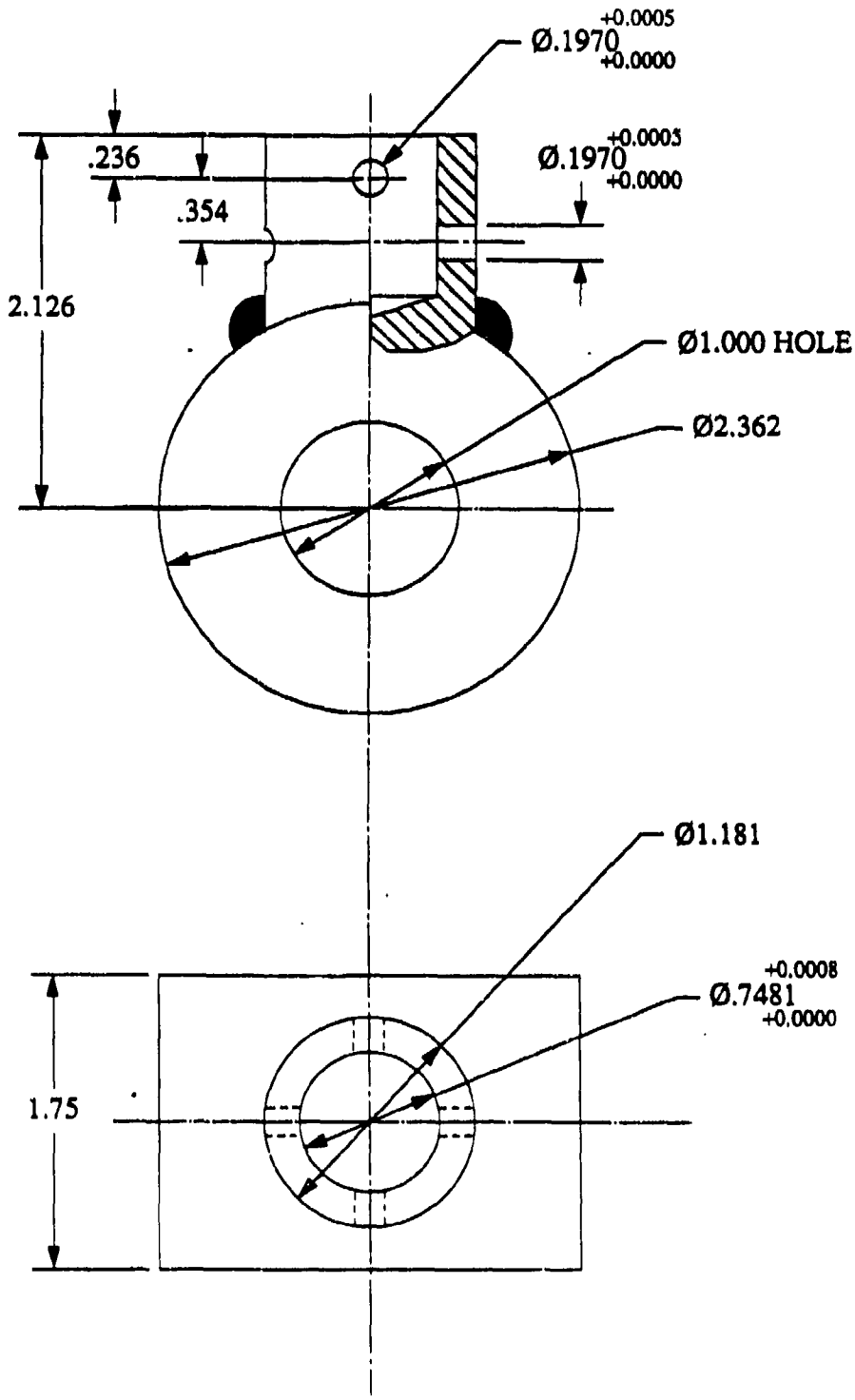

Upper joint	Grade 12.9 Alloy steel	1
Part name	Material	Qty

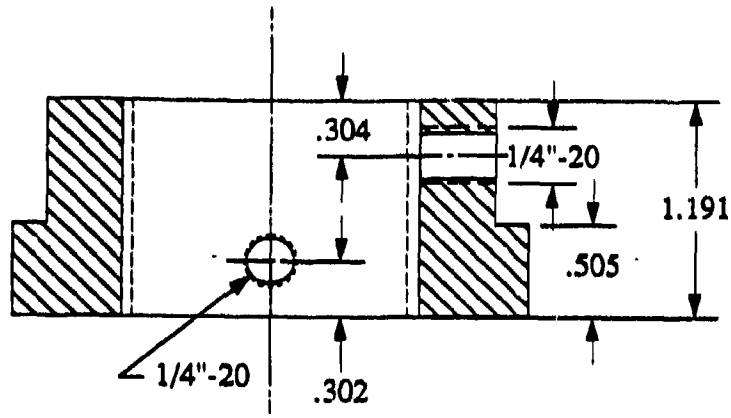

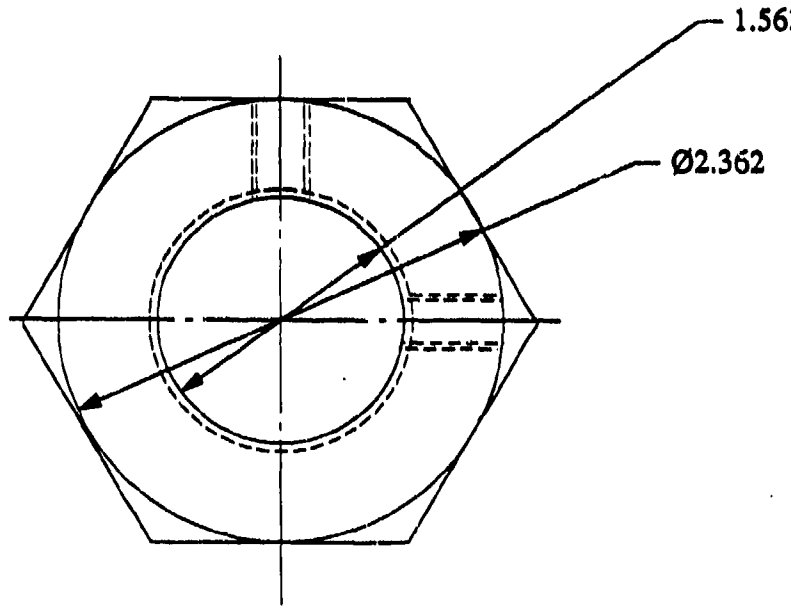

Part name	Material	Qty
Joining nut	Grade 12.9 Alloy steel	1

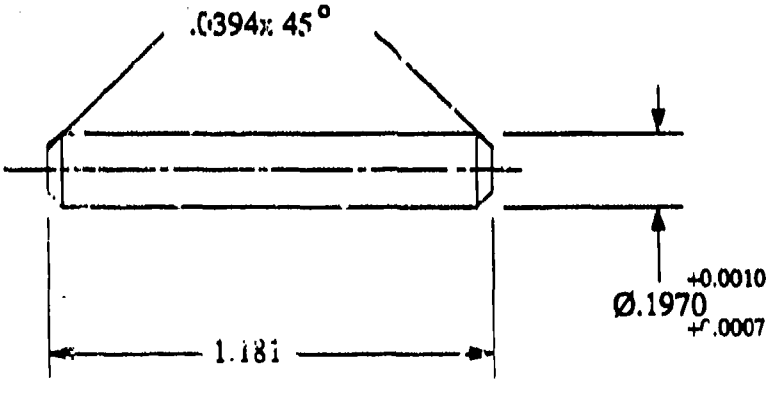

Scale : 2:1

Part name	Material	Qty
Pin	Grade 12.9 Alloy steel	2

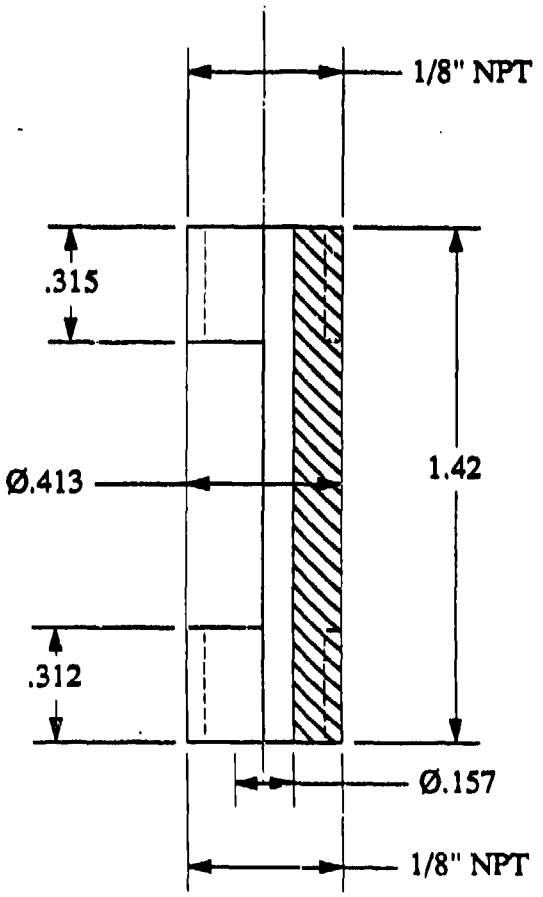

Scale : 2:1

Part name	Material	Qty
Valve connector	303 Stainless steel	1

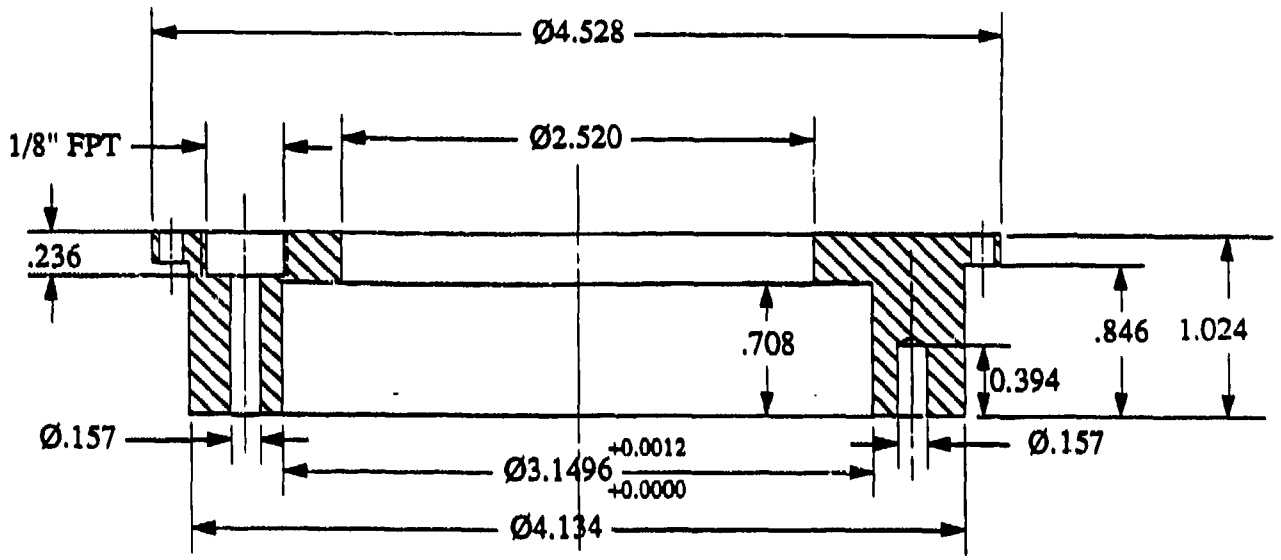

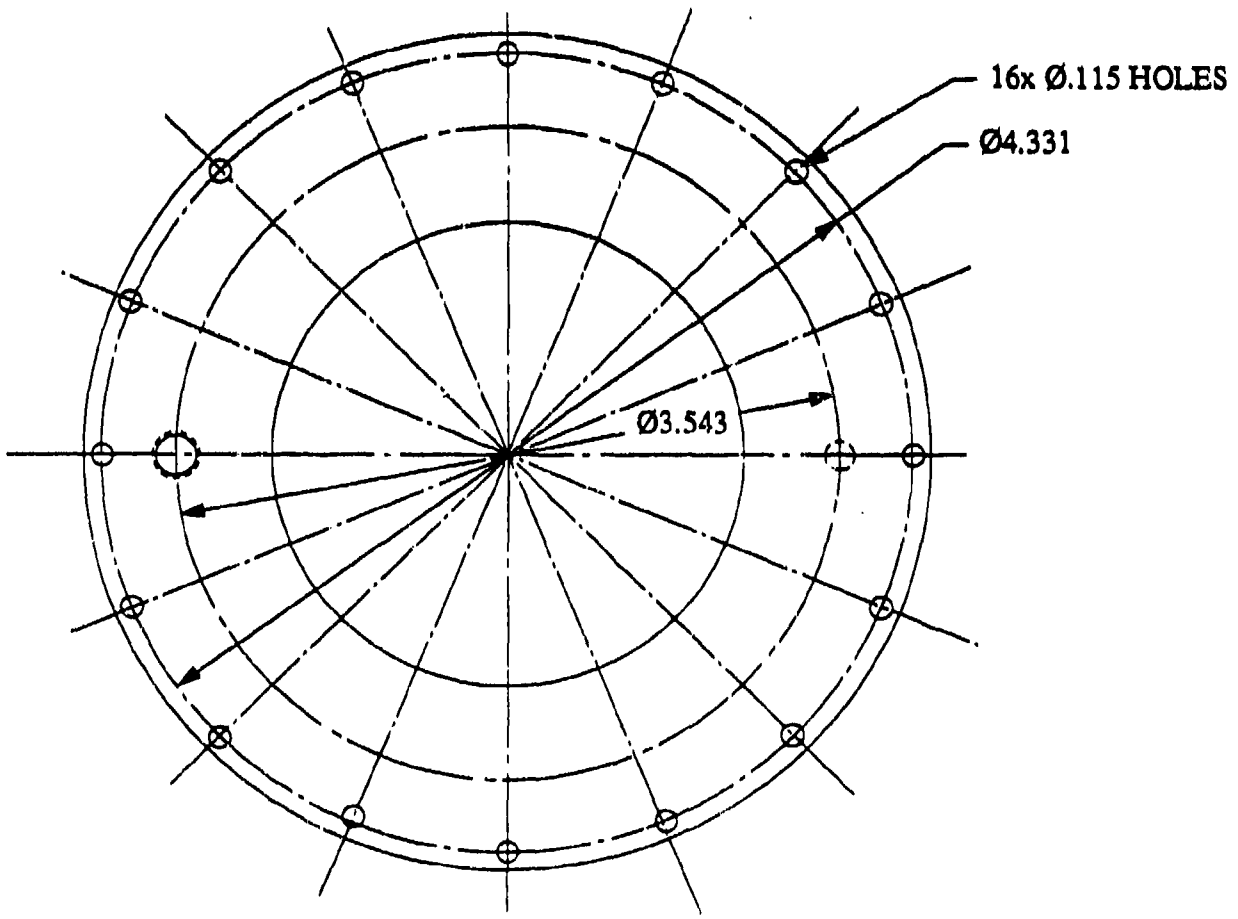

Bearing seat	303 Stainless steel	1
Part name	Material	Qty

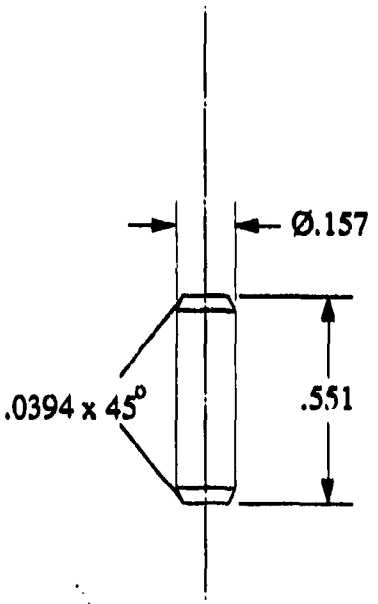

Scale: 2:1

Part name	Material	Qty
Insert pin	303 Stainless steel	2

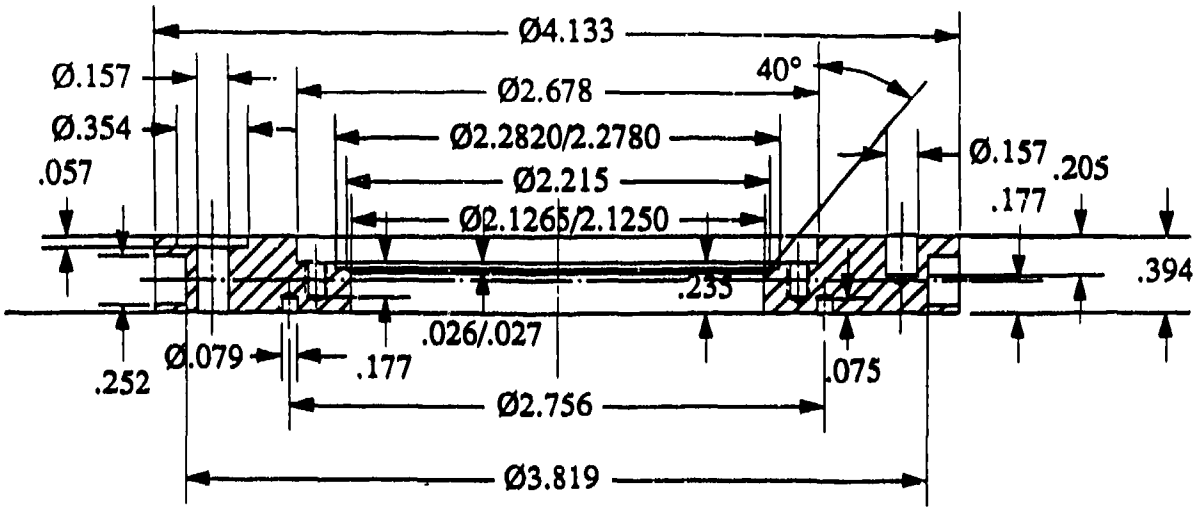

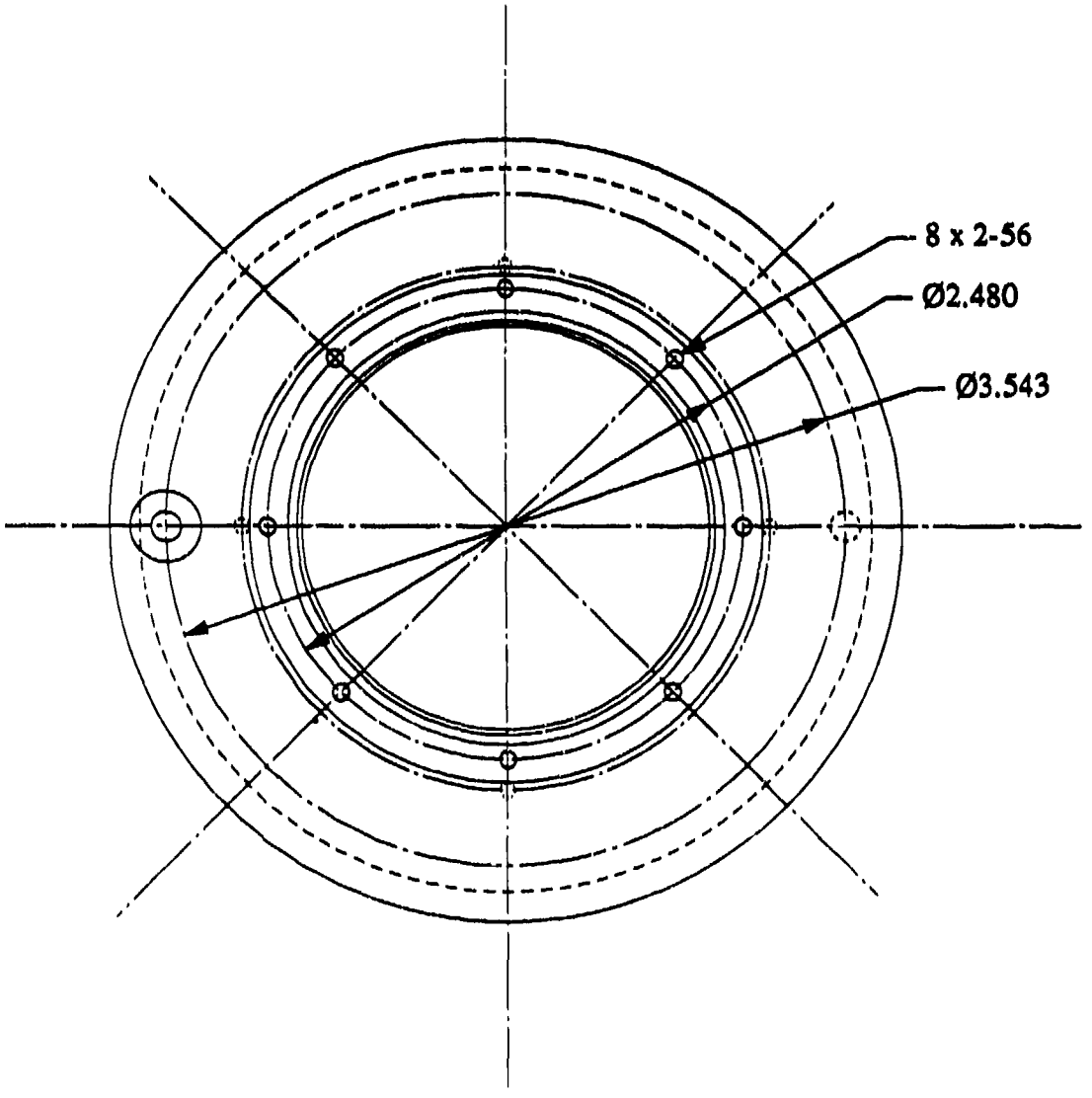

Cap	303 Stainless steel	2
Part name	Material	Qty

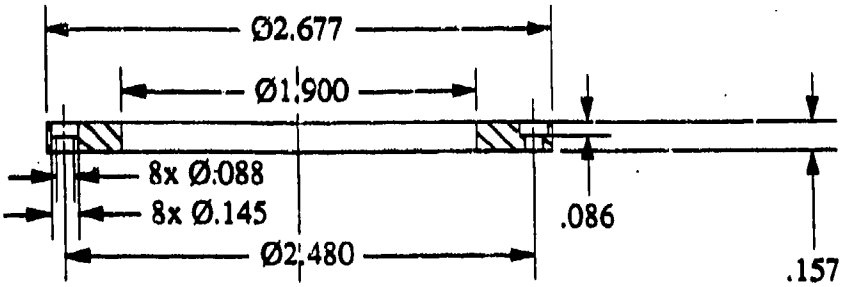

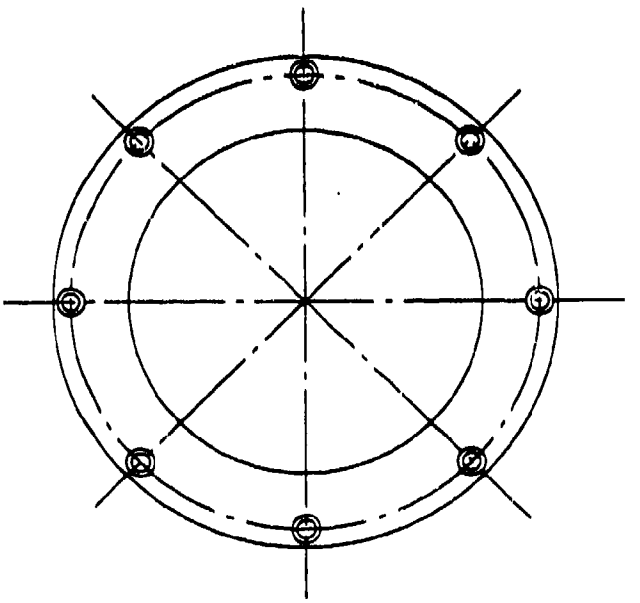

Part name	Material	Qty
Seal holder	303 Stainless steel	2

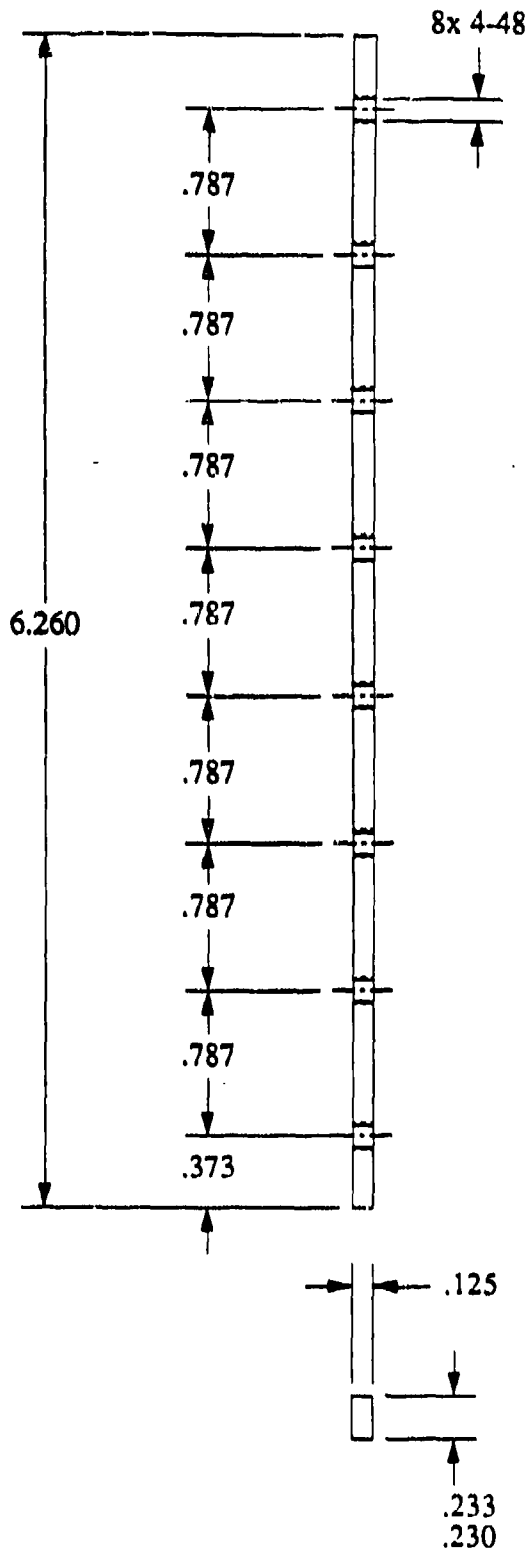

All corners R 0.02

Part name	Material	Qty
Stator feather key	303 Stainless steel	2

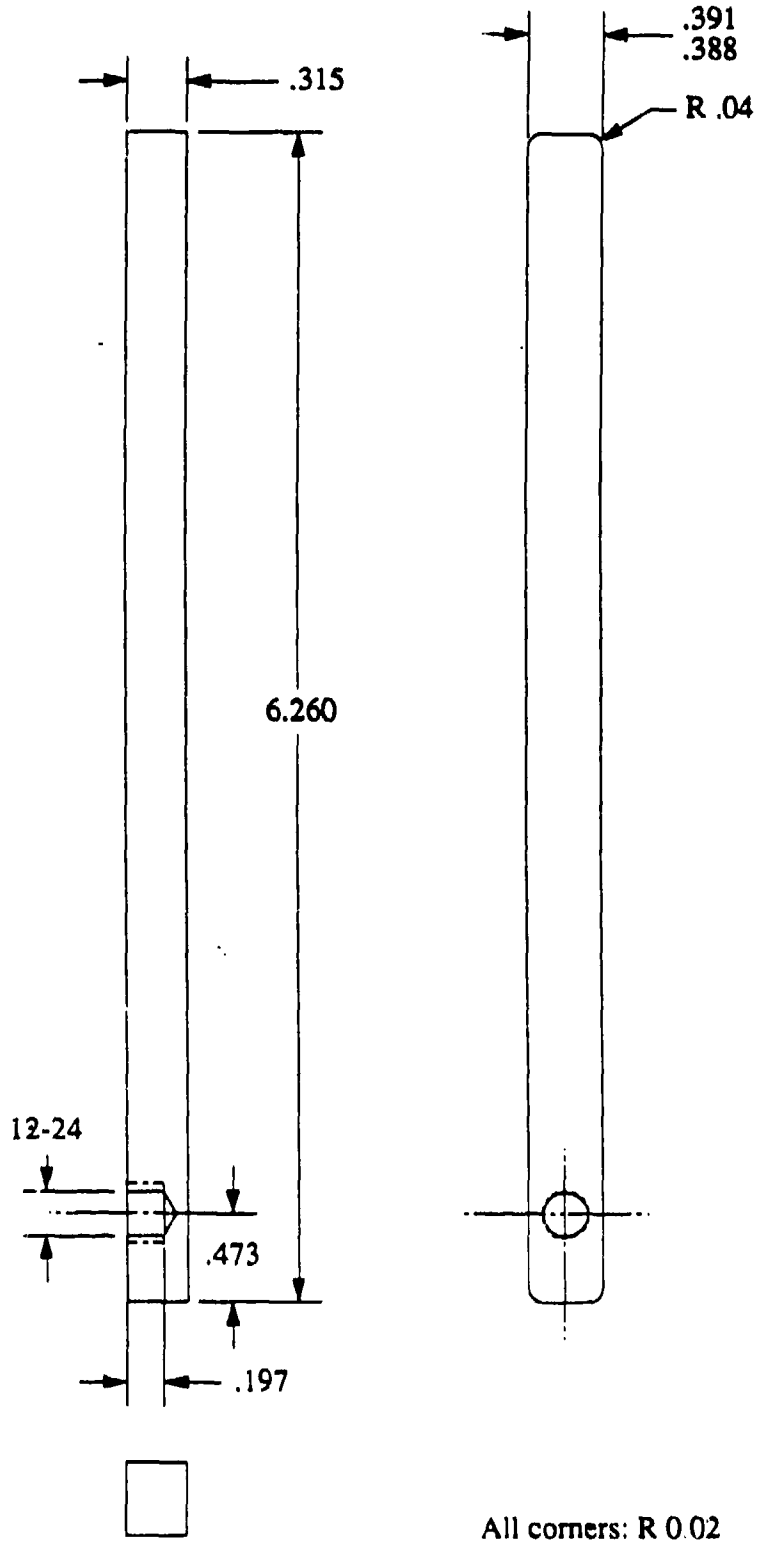

All corners: R 0.02

Part name	Material	Qty
Rotator feather key	303 Stainless steel	2

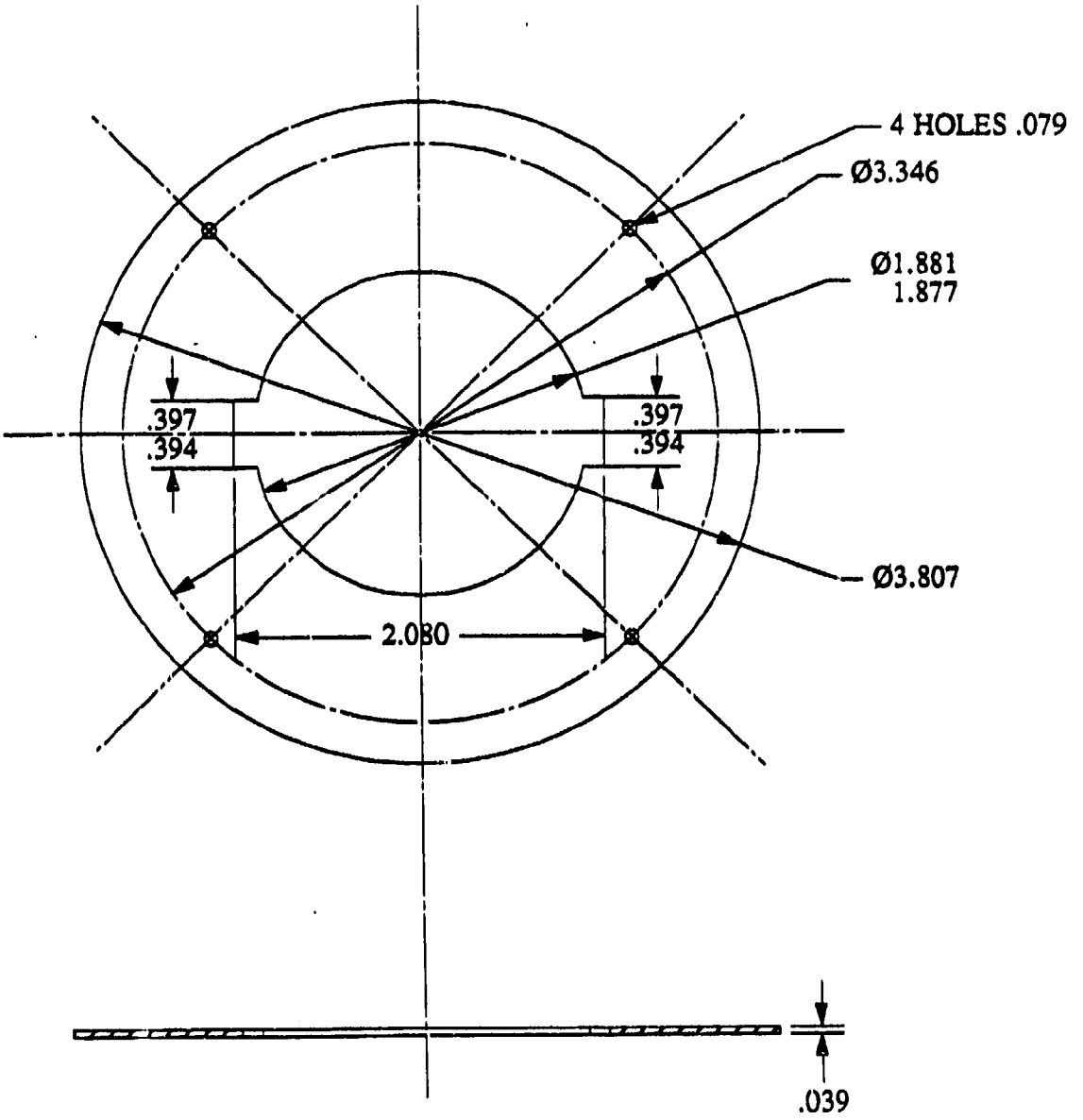

All corners: R 0.02

Part name	Material	Qty
Hot electrode	Stainless steel 18-8	40

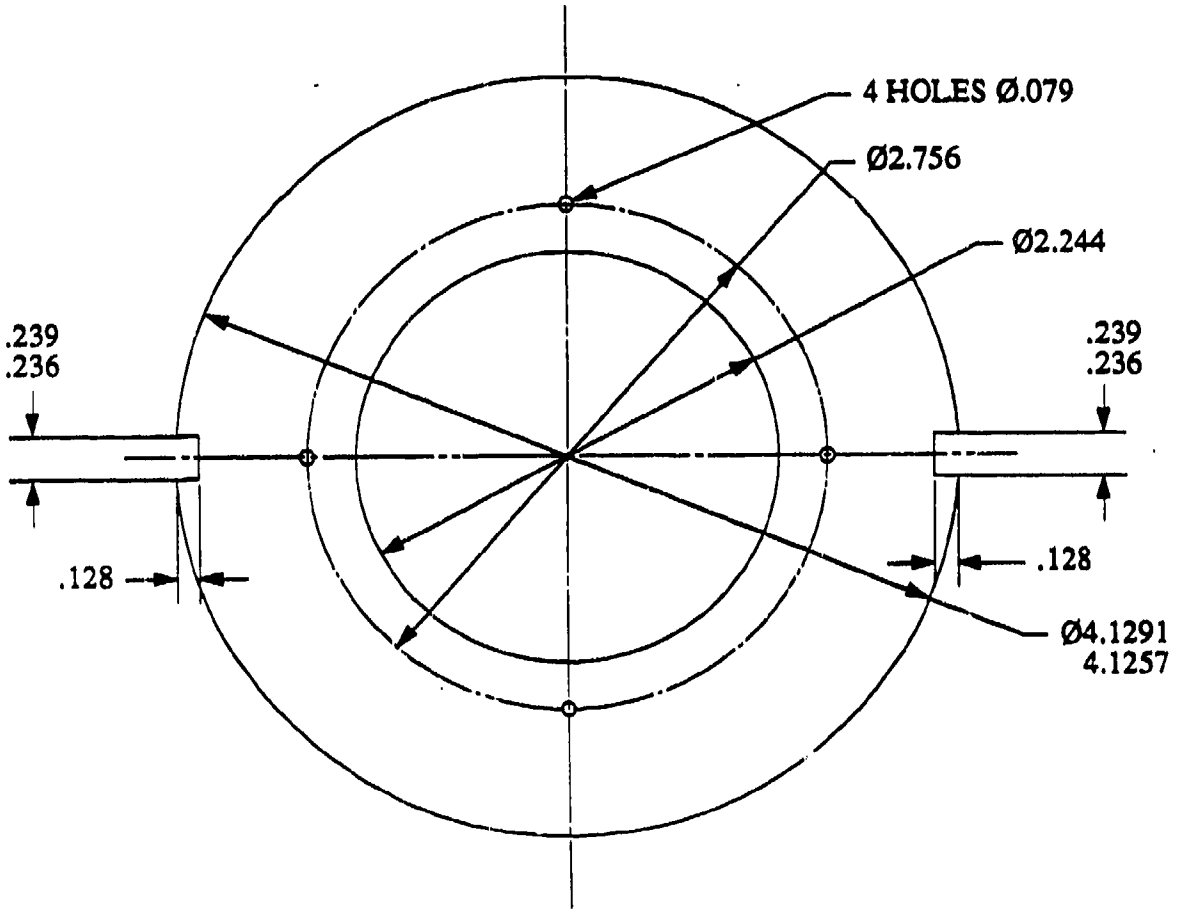

All corners: R 0.02

Thickness: .039

Part name	Material	Qty
Ground electrode	Stainless steel 18-8	39

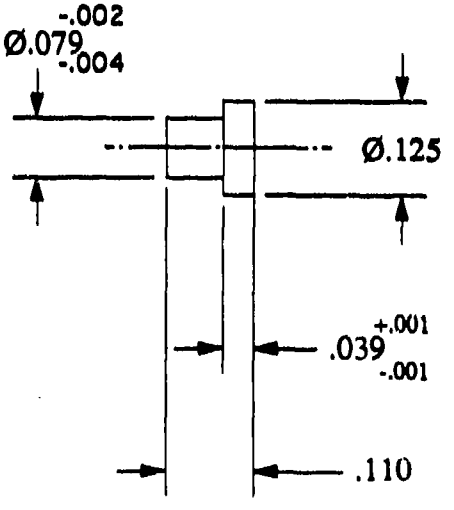

Scale: 4:1

Part name	Material	Qty
Spacer	Delrin	320

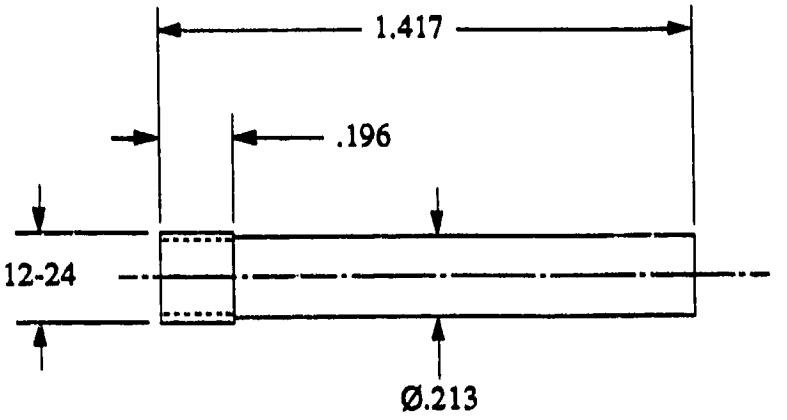

Scale: 2:1

Part name	Material	Qty
Conduct bolt	Brass	1

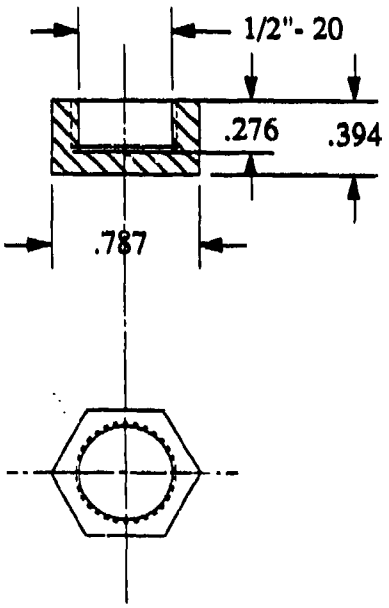

Part name	Material	Qty
Metal piece	Brass	1

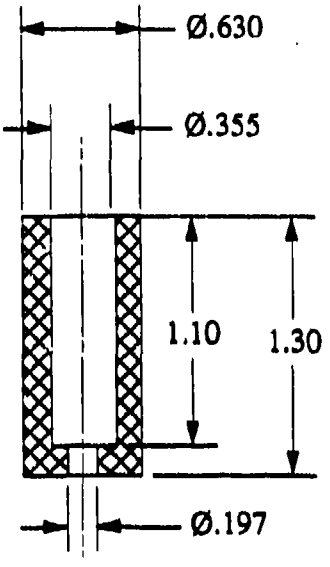

Part name	Material	Qty
Brush holder	Glass epoxy G-11	1

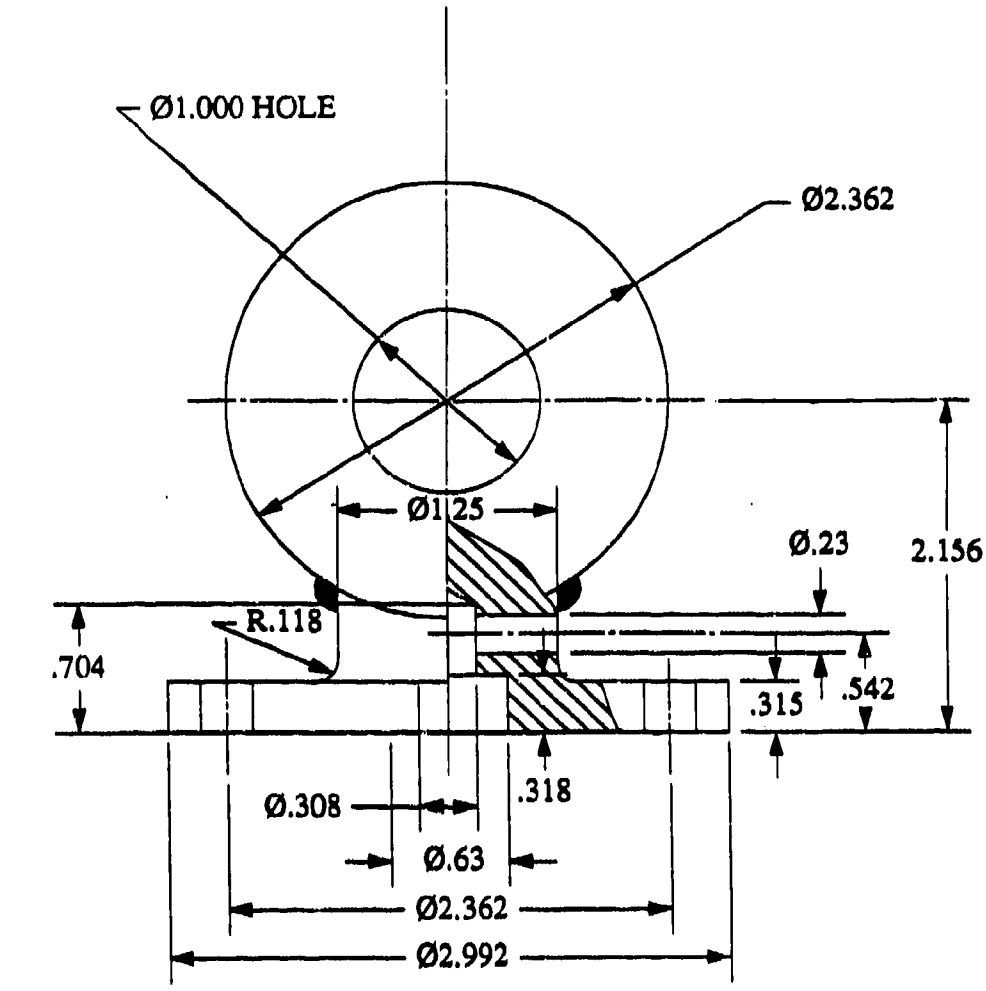

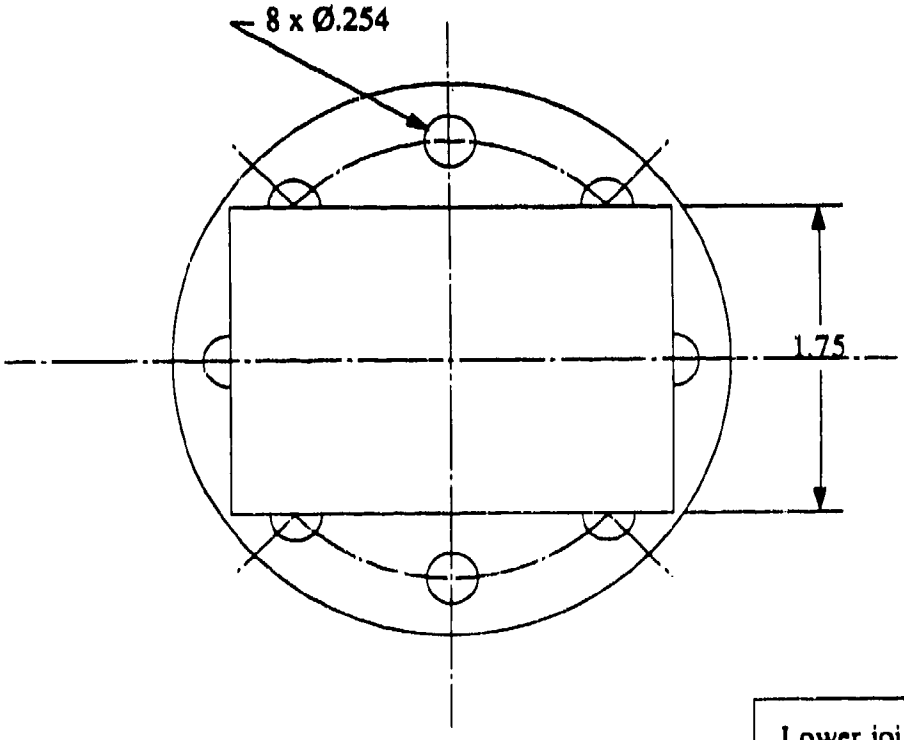

Lower joint	Grade 12.9 Alloy steel	1
Part name	Material	Qty

APPENDIX C:
The Quarter-HMMWV Simulation Program

The Simulation Program

```
C     TACSIM.FOR
C
C    To simulate the quarter car model for TACOM project.
C
C ***** Parameters and Variables
C
C    AS:      sprung mass acceleration
C    ASA:     sprung mass acceleration amplitude
C    ASOAG:   ASA/AGA
C    ASOAG:   ASA/AGA array
C    AU:      unsprung mass acceleration
C    AUA:     unsprung mass acceleration amplitude
C    AUOAG:   AUA/AGA
C    AUOAGA:  AUA/AGA array
C    AG:      ground acceleration
C    AGA:     ground acceleration amplitude
C    ANGLEA:  Screw-nut lead angle (e.g. 45 deg.)                    (input)
C    ANGTHR:  Thread angle for Acme threads (14.5 deg)               (in-data)
C    DEG:     phase angle in degree
C    DLS:     (dynamic) spring compression
C    DLSS:    static spring compression
C    DLT:     (dynamic) tire spring compression
C    DLTMAX:  maximum tire spring compression                        (input)
C    DLTS:    static tire spring compression
C    DPSCRE:  Screw-nut pitch diameter                               (input)
C    DT:      time step size
C    DTHETA:  phase angle step size
C    ERH:     ER valve gap hight                                     (input)
C    ERRHO:   ER fluid density                                       (input)
C    ERRI:    ER plate inner radius                                  (input)
C    ERRO:    ER plate outer radius                                  (input)
C    ETA:     plastic viscosity                                      (input)
C    F, FF:   Road profile frequency;  F single, FF array
C    FDN:     Newtonian part of damping force
C    FDER:    ER part of damping force
C    FDERC:   Control or ideal FDERC
C    FETA:    A factor in FDN calculation, FDN = FETA*ETA*DV
C    FIT:     Iteration factor
C    FS:      spring force
C    FSCREW:  Friction coefficient                                   (input)
C    FST:     total shock force
C    FT:      F_t, tire (spring) force
C    FTY:     A factor in FDER calculation, FDER = FTY*TY
C    G:       Gravitational acceleration
C    I3:      Output interval                                        (input)
C    ICONTR:  Control strategy:
C                  0 -- No ER control.
```

```
C                1-- Skyhook
C                2-- Conventional
C     ICYCLE: cycle counter
C     ICYCLM: maximum for ICYCLE                                    (input)
C     IMAX:   (IMAX-1) no. of steps in each cycle                   (input)
C     ITAU    = 1 if DT/TAUER > 1.0
C             = 0 otherwise
C     NPLT:   No. of plates                                         (input)
C     OMEGA:  angular frequency
C     RFT:    Ratio of the translational damping force to torque
C     RK:     k in equation (W3)                                    (input)
C     RKS:    spring constant.                                      (input)
C     RKSC:   k_c, compression constant in eq w4                    (input)
C     RKST:   k_t, tension constant in eq w4                        (input)
C     RKT:    tire spring constant                                  (input)
C     RLS:    (dynamic) spring length
C     RLSS:   static spring length
C     RMS:    sprung mass                                           (input)
C     RMU:    unsprung mass                                         (input)
C     RTR:    Ratio of the translational velocity to rotational
C             or angular velocity
C     T:      time
C     TAUER:  ER fluid time constant
C     THETA:  phase angle                                           (input)
C     TY:     The Bingham stress in TY = TYC*(VC)^TYN
C     TYC:    A constant in TY = TYC*(VC)^TYN                       (input)
C     TYLIM:  TY at VCLIM
C     TYN:    The exponent in TY = TYC*(VC)^TYN                     (input)
C     VC:     control voltage
C     VCLIM   the limit of VC                                       (input)
C     VG:     gournd velocity
C     VGA:    ground velocity amplitude
C     VS:     sprung velocity
C     VU:     unsprung velocity
C     VV      =VS(I)*VSU
C     XG:     ground displacement
C     XGA:    ground displacement amplitude                         (input)
C     XS:     sprung mass displacement
C     XU:     unsprung mass displacement
C
      IMPLICIT REAL*8(A-H,O-Z)

      DIMENSION XS(5000),XU(5000),VS(5000),VU(5000)
      DIMENSION AS(5000),AU(5000)
      DIMENSION FS(5000),FDER(5000),FDN(5000),DEG(5000)
      DIMENSION FST(5000),FT(5000)
      DIMENSION FF(50),ASOAGA(50),AUOAGA(50)

      OPEN (5,FILE='tacsim.5')
      OPEN (6,FILE='tacsim.6')

      READ(5,*) ANGLEA
      READ(5,*) DLTMAX
      READ(5,*) DPSCRE
      READ(5,*) ERH
      READ(5,*) ERRHO
      READ(5,*) ERRI
      READ(5,*) ERRO
```

```
      READ(5,*) ETA
      READ(5,*) FIT
      READ(5,*) FSCREW
      READ(5,*) I3
      READ(5,*) ICONTR
      READ(5,*) ICYCLM
      READ(5,*) IMAX
      READ(5,*) NPLT
      READ(5,*) RK
      READ(5,*) RKS
      READ(5,*) RKSC
      READ(5,*) RKST
      READ(5,*) RKT
      READ(5,*) RMS
      READ(5,*) RMU
      READ(5,*) TAUER
      READ(5,*) TYC
      READ(5,*) TYN
      READ(5,*) VCLIM
      READ(5,*) XGA
      READ(5,*) NF
      DO 5 IFF=1,NF
      READ(5,*) FF(IFF)
    5 CONTINUE

      WRITE(6,*) 'ANGLEA=',ANGLEA
      WRITE(6,*) 'DLTMAX=',DLTMAX
      WRITE(6,*) 'DPSCRE=',DPSCRE
      WRITE(6,*) 'ERH   =',ERH
      WRITE(6,*) 'ERRHO =',ERRHO
      WRITE(6,*) 'ERRI  =',ERRI
      WRITE(6,*) 'ERRO  =',ERRO
      WRITE(6,*) 'ETA   =',ETA
      WRITE(6,*) 'FIT   =',FIT
      WRITE(6,*) 'FSCREW=',FSCREW
      WRITE(6,*) 'I3    =',I3
      WRITE(6,*) 'ICONTR=',ICONTR
      WRITE(6,*) 'ICYCLM=',ICYCLM
      WRITE(6,*) 'IMAX  =',IMAX
      WRITE(6,*) 'NPLT  =',NPLT
      WRITE(6,*) 'RK    =',RK
      WRITE(6,*) 'RKS   =',RKS
      WRITE(6,*) 'RKSC  =',RKSC
      WRITE(6,*) 'RKST  =',RKST
      WRITE(6,*) 'RKT   =',RKT
      WRITE(6,*) 'RMS   =',RMS
      WRITE(6,*) 'RMU   =',RMU
      WRITE(6,*) 'TAUER =',TAUER
      WRITE(6,*) 'TYC   =',TYC
      WRITE(6,*) 'TYN   =',TYN
      WRITE(6,*) 'VCLIM =',VCLIM
      WRITE(6,*) 'XGA   =',XGA
      WRITE(6,*) 'NF    =',NF
      DO 7 IFF=1,NF
    7 WRITE(6,*) 'F',IFF,' = ',FF(IFF)

C ************** Initialization
```

```
      WRITE(6,*) ' '
      WRITE(6,*) 'Some output  '
      G=9.80665
      PI=3.14159
C thread angle 14.5 deg.
      ANGTHR=14.5*PI/180.0
C lead angle unit conversion
      ANGLEA=ANGLEA*PI/180.0
C Screw-nut conversion ratios
      RFT=(DPSCRE/2.0)*(DCOS(ANGTHR)*DTAN(ANGLEA)-
     +               FSCREW)/(FSCREW*DTAN(ANGLEA)+DCOS(ANGTHR))
      RTR=1.0/((DPSCRE/2.0)*DTAN(ANGLEA))
      WRITE(6,*) 'RFT   =',RFT
      WRITE(6,*) 'RTR   =',RTR

C FTY defined in FDER = FTY*TY
      FTY=(4.*PI*NPLT/3.)*(ERRO**3-ERRI**3)/RFT
      write(6,*) 'FTY = ', FTY

C FETA defined in FDN = FETA*(DV*ETA)
      FETA=(PI*NPLT*RTR/ERH)*(ERRO**4-ERRI**4)/RFT
      write(6,*) 'FETA =',FETA

      TYLIM=TYC*VCLIM**TYN
      WRITE(6,*) 'TYlim =',TYLIM

C Spring stuff
      DLSS=RMS*G/RKS
      DLTS=(RMS+RMU)*G/RKT
      WRITE(6,*) 'static spring deflection =',DLSS
      WRITE(6,*) 'static tire deflection =',DLTS

C ********************************* FREQUENCY ITERATION

      DO 800 IFF=1,NF

      F=FF(IFF)

      WRITE(6,*) ' '
      WRITE(6,*) ' ***************  F = ',F

C Angular frequency
      OMEGA=2.0*PI*F
C Ground acceleration amplitude
      AGA=OMEGA**2*XGA
C       Ground velocity amplitude
      VGA=OMEGA*XGA
      WRITE(6,*) 'AGA =',AGA
      WRITE(6,*) 'VGA =',VGA
C phase angle step size (in Radium)
      DTHETA=2.0*PI/(IMAX-1.0)
C time step size
      DT=DTHETA/OMEGA
      WRITE(6,*) 'DT    =', DT

      CONST=DT/TAUER
      WRITE(6,*) 'DT/TAUER =',CONST
      IF(CONST.GT.1.0) THEN
```

```
       ITAU=1
      ELSE
       ITAU=0
      END IF

C****************** Marching in Time Domain
      I=1
      DEG(I)=0.0
      XU(I)=0.0
      XS(I)=0.0
      VS(I)=0.0
      VU(I)=0.0
      AS(I)=0.0
      AU(I)=0.0
      FS(I)=0.0
      FT(I)=0.0
      FDN(I)=0.0
      FDER(I)=0.0
      FST(I)=0.0
      TYOLD=0.0

      ICYCLE=0
      ASA=9999.999
      AUA=9999.999
   40 ICYCLE=ICYCLE+1


      IF(ICYCLE.GT.1) THEN
         DASA=DABS((ASA-ASAOLD)/ASAOLD)
         I=1
         XU(I)=XU(IMAX)
         XS(I)=XS(IMAX)
         VS(I)=VS(IMAX)
         VU(I)=VU(IMAX)
         AS(I)=AS(IMAX)
         AU(I)=AU(IMAX)
         FS(I)=FS(IMAX)
         FT(I)=FT(IMAX)
         FDN(I)=FDN(IMAX)
         FDER(I)=FDER(IMAX)
         FST(I)=FST(IMAX)
         IF(DASA.LT.0.0001) GO TO 100
      END IF

      IF(ICYCLE.GT.ICYCLM) GO TO 100

         ASAOLD=ASA
         AUAOLD=AUA
         ASA=0.0
         AUA=0.0
         VCMAX=0.0
         TYMAX=0.0

      IMAXM1=IMAX-1

C NUMBER OF ITERATIONS
      NIT=0
C AVERAGE CONVERGENCE
```

```
      ACIT=0.0

      DO 90 I=2,IMAX

      THETA=(I-1.0)*DTHETA
      DEG(I)=THETA*180.0/PI

C ground Motion
      XG=XGA*DSIN(THETA)
C ground velocity
      VG=OMEGA*XGA*DCOS(THETA)

      XS(I)=XS(I-1)
      XU(I)=XU(I-1)
      VS(I)=VS(I-1)
      VU(I)=VU(I-1)
      AS(I)=AS(I-1)
      AU(I)=AU(I-1)

C  ********************   ITERATION
      DO 70 IT=1,20

C spring force
      DLS=DLSS+XU(I)-XS(I)
      FS(I)=RKS*DLS
C     relative velocity
      DV=VU(I)-VS(I)

C ***** Newtonian damping force (FDN)

C write(6,*) 'stop 1'
      FDN(I)=FETA*ETA*DV

C **** ER damping force (FDER)

C -- No ER control

      IF(ICONTR.EQ.0) THEN
         FDER(I)=0.0
      END IF

C -- Control Strategy 1

C Skyhook
      IF(ICONTR.EQ.1) THEN
        VSU=VS(I)-VU(I)
        VV=VS(I)*VSU
        IF(VV.GT.0.0) THEN
C FDER and VS have the opposite sign.
C Control voltage
            VC=(DABS(RK*VS(I)))**(1./2.5)
            IF(VC.GT.VCLIM) VC=VCLIM
            IF(ITAU.EQ.0) THEN
               TY=TYOLD+(DT/TAUER)*(TYC*VC**TYN-TYOLD)
            ELSE
       TY=TYC*VC**TYN
    END IF
            FDER(I)=-(VS(I)/(DABS(VS(I))+0.0000001))*FTY*TY
```

```
        ELSE
            FDER(I)=0.0
        END IF
      END IF

C -- Control Strategy 2

C Conventional Damper
      IF(ICONTR.EQ.2) THEN
        VSU=VS(I)-VU(I)
        IF(VSU.LT.0.0) THEN
C COMPRESSION (damping force on the sprung mass pointing up, FDER > 0)
          VC=(DABS(RKSC*VSU))**(1./2.5)
          IF(VC.GT.VCLIM) VC=VCLIM
          IF(ITAU.EQ.0) THEN
             TY=TYOLD+(DT/TAUER)*(TYC*VC**TYN-TYOLD)
          ELSE
     TY=TYC*VC**TYN
  END IF
          FDER(I)=-(VSU/(DABS(VSU)+0.0000001))*FTY*TY
        ELSE
C TENSION (damping force on the sprung mass pointing down, FDER < 0)
          VC=(DABS(RKST*VSU))**(1./2.5)
          IF(VC.GT.VCLIM) VC=VCLIM
          IF(ITAU.EQ.0) THEN
             TY=TYOLD+(DT/TAUER)*(TYC*VC**TYN-TYOLD)
          ELSE
     TY=TYC*VC**TYN
          END IF
          FDER(I)=-(VSU/(DABS(VSU)+0.0000001))*FTY*TY
        END IF
      END IF

C Control electric field strength

C Total strut force

      FST(I)=FDER(I)+FDN(I)+FS(I)

C ********** Integration

C **** Unsprung mass dynamics

C tire compression (positive when compressed)
      DLT=DLTS-XU(I)+XG
      IF(DLT.GT.DLTMAX) THEN
        WRITE(6,*) 'STOP, TIRE BOTTOMED OUT. ICYCLE, I=',ICYCLE,',',I
        CLOSE(5)
        CLOSE(6)
        STOP
      END IF
      IF(DLT.GT.0.0) THEN
         FT(I)=RKT*DLT
      ELSE
         FT(I)=0.0
      END IF

C unsprung mass acceleration
```

```
      CONST=(-FST(I)+FT(I))/RMU-G
      AU(I)=(1.0-FIT)*AU(I)+FIT*CONST

C velocity and displacement
      VU(I)=VU(I-1)+0.5*(AU(I)+AU(I-1))*DT
      XU(I)=XU(I-1)+0.5*(VU(I)+VU(I-1))*DT

C **** Sprung mass dynamics

C  sprung mass acceleration
      CONST=FST(I)/RMS-G
      CIT=DABS(CONST-AS(I))/(DABS(AS(I))+0.0000000001)
      AS(I)=(1.0-FIT)*AS(I)+FIT*CONST

C velocity and displacement
      VS(I)=VS(I-1)+0.5*(AS(I)+AS(I-1))*DT
      XS(I)=XS(I-1)+0.5*(VS(I)+VS(I-1))*DT

      IF(IT.GT.2) THEN
         IF(CIT.LT.0.001) GO TO 71
      END IF

   70 CONTINUE

   71 CONTINUE

      NIT=NIT+IT-1
      ACIT=ACIT+CIT

C absolute value
      AAS=DABS(AS(I))
      IF(AAS.GT.ASA) THEN
         ASA=AAS
      END IF
      AAU=DABS(AU(I))
      IF(AAU.GT.AUA) THEN
         AUA=AAU
      END IF

C **** Update

      IF(VC.GT.VCMAX) VCMAX=VC
      IF(TY.GT.TYMAX) TYMAX=TY

      TYOLD=TY

   90 CONTINUE

      GO TO 40

  100 CONTINUE

      ASOAG=ASA/AGA
      AUOAG=AUA/AGA
      WRITE(6,*) ''
      WRITE(6,*) 'ASA/AGA =',ASOAG
      WRITE(6,*) 'AUA/AGA =',AUOAG
      ICYCLE=ICYCLE-1
```

```
      WRITE(6,*) 'ICYCLE =',ICYCLE
      WRITE(6,*) 'VCMAX  =',VCMAX
      WRITE(6,*) 'TYMAX  =',TYMAX

      ASOAGA(IFF)=ASOAG
      AUOAGA(IFF)=AUOAG

      NIT=NIT/IMAXM1
      WRITE(6,*) 'AVERAGE NUMBER OF ITERATION = ',NIT
      ACIT=ACIT/IMAXM1
      WRITE(6,*) 'AVERAGE CONVERGNECE (%) = ',ACIT

  600 FORMAT(E12.5)

      IF(NF.EQ.1) THEN

      WRITE(6,*) ' '
      WRITE(6,*) 'DEG ='
      DO 120 I=1,IMAX,I3
  120 WRITE(6,600) DEG(I)

      WRITE(6,*) ' '
      WRITE(6,*) 'XS ='
      DO 122 I=1,IMAX,I3
  122 WRITE(6,600) XS(I)

      WRITE(6,*) ' '
      WRITE(6,*) 'XU ='
      DO 123 I=1,IMAX,I3
  123 WRITE(6,600) XU(I)

      WRITE(6,*) ' '
      WRITE(6,*) 'VS ='
      DO 124 I=1,IMAX,I3
  124 WRITE(6,600) VS(I)

      WRITE(6,*) ' '
      WRITE(6,*) 'VU ='
      DO 125 I=1,IMAX,I3
  125 WRITE(6,600) VU(I)

      WRITE(6,*) ' '
      WRITE(6,*) 'AS  ='
      DO 322 I=1,IMAX,I3
  322 WRITE(6,600) AS(I)

      WRITE(6,*) ' '
      WRITE(6,*) 'AU  ='
      DO 324 I=1,IMAX,I3
  324 WRITE(6,600) AU(I)

      WRITE(6,*) ' '
      WRITE(6,*) 'FS ='
      DO 126 I=1,IMAX,I3
  126 WRITE(6,600) FS(I)

      WRITE(6,*) ' '
      WRITE(6,*) 'FT  ='
```

```
      DO 127 I=1,IMAX,I3
  127 WRITE(6,600) FT(I)

      WRITE(6,*) ' '
      WRITE(6,*) 'FDN ='
      DO 128 I=1,IMAX,I3
  128 WRITE(6,600) FDN(I)

      WRITE(6,*) ' '
      WRITE(6,*) 'FDER ='
      DO 130 I=1,IMAX,I3
  130 WRITE(6,600) FDER(I)

      WRITE(6,*) ' '
      WRITE(6,*) 'FST ='
      DO 136 I=1,IMAX,I3
  136 WRITE(6,600) FST(I)

      END IF

  800 CONTINUE

      WRITE(6,*) ' '
      WRITE(6,*) 'ASA/AGA'
      DO 810 IFF=1,NF
  810 WRITE(6,*) ASOAGA(IFF)

      WRITE(6,*) ' '
      WRITE(6,*) 'AUA/AGA'
      DO 820 IFF=1,NF
  820 WRITE(6,*) AUOAGA(IFF)

      CLOSE(5)
      CLOSE(6)
      STOP
      END
```

An Input Data File

```
17.6568,        ANGLEA:   Screw-nut lead angle (e.g. 45 deg.)
0.25,           DLTMAX:   maximum tire spring compression              (input)
0.0254,         DPSCRE:   Screw-nut pitch diameter, 1" pitch, 1"
                          lead                                         (input)
0.001,          ERH:      ER valve gap hight                         (input)
1000.0,         ERRHO:    ER fluid density                           (input)
0.0285,         ERRI:     ER plate inner radius, Di = 2.244", Ri =
                          .0285 m                                    (input)
0.0483489,      ERRO:     ER plate outer radius, Do=3.807",
                          Ro=0.04835 m                               (input)
0.222,          ETA:      plastic viscosity, 100cP = 0.1 N.s/m^2
                          (input)
0.2,            FIT       iteration factor, ------
0.033,          FSCREW:   Friction coef = 0.033 for a efficiency of
                          89% with 1"X1"
5,              I3,       Output interval                            (input)
1,              ICONTR:   Control strategy --------                  (input)
```

```
10,             ICYCLEM:  Maximum cycle number                          (input)
361,            IMAX:     (IMAX-1) no. of steps in each cycle           (input)
40,             NPLT:     No. of plates                                 (input)
590550000.0,    RK:       k in equation w3                              (input)
163300.0,       RKS:      spring constant                               (input)
315000000.0,    RKSC:     k_c, compression constant in eq w4            (input)
630000000.0,    RKST:     k_t, tension constant in eq w4                (input)
463800.0,       RKT:       tire spring constant                         (input)
998.0,          RMS:      sprung mass  2200 lb = 998 kg                 (input)
181.0,          RM        U: unsprung mass 400 lbm = 181 kg
0.0002,         TAUER     ----------
0.000095,       TYC
2.0,            TYN
3000.0          VCLIM -   LIMIT FOR VC = 3000 V.
0.01,           XGA:      ground displacement amplitude,                (input)

25,             NF
1e-1,           F1
2e-1,           F2
5e-1,
8e-1,
1e+0,
1.5e+0,
1.8e+0,
1.9e+0,
2e+0,
2.5e+0,
3e+0,
4e+0,
6e+0,
7e+0,
8e+0,
8.5e+0,
9e+0,
9.5e+0,
1e+1,
1.2e+1,
1.4e+1,
1.6e+1,
1.8e+1,
2e+1,
2.5e+1,
```

APPENDIX D:
Data Plots from Tests of the ER Damper on the Quarter-HMMWV Ride Simulator

This appendix presents a complete set of data plots from the testing of the ER damper on the quarter-HMMWV ride simulator.

Figure D-1 shows the modified road profiles used to drive the simulator. This profiles were derived from the proving grounds road profiles which were provide to UMTRI by TACOM. The modifications were essentially the necessary high-pass filtering required to reduce the vertical elevation of the road profiles to within the capability of the simulator.

Figure D-2 through D-25 present results of testing displayed as transfer function gains in the frequency domain. Figures D-2 through D-9 show the gains of sprung mass acceleration, relative to road surface acceleration, as observed on the eight road surfaces, respectively. Each figure contains three plots, one each for the gains under three operating conditions. These were (1) ER damper installed with control voltage off, (2) ER damper installed and the skyhook controller in use, and (3) conventional HMMWV shock absorber installed.

Figures D-10 through D-17 is display comparing the sprung mass acceleration gains observed using the conventional shock absorber with the same gain observed when the ER damper was controlled to simulate a conventional damper. Again, there are eight figures associated with the eight roads, respectively.

Finally, figures D-18 through D-25 show the tire forces gains, that is: (tire force)/(road surface acceleration). The eight figures are for the eight roads, respectively. The three plots are for the same three operating conditions described for figures D-2 through D-17.

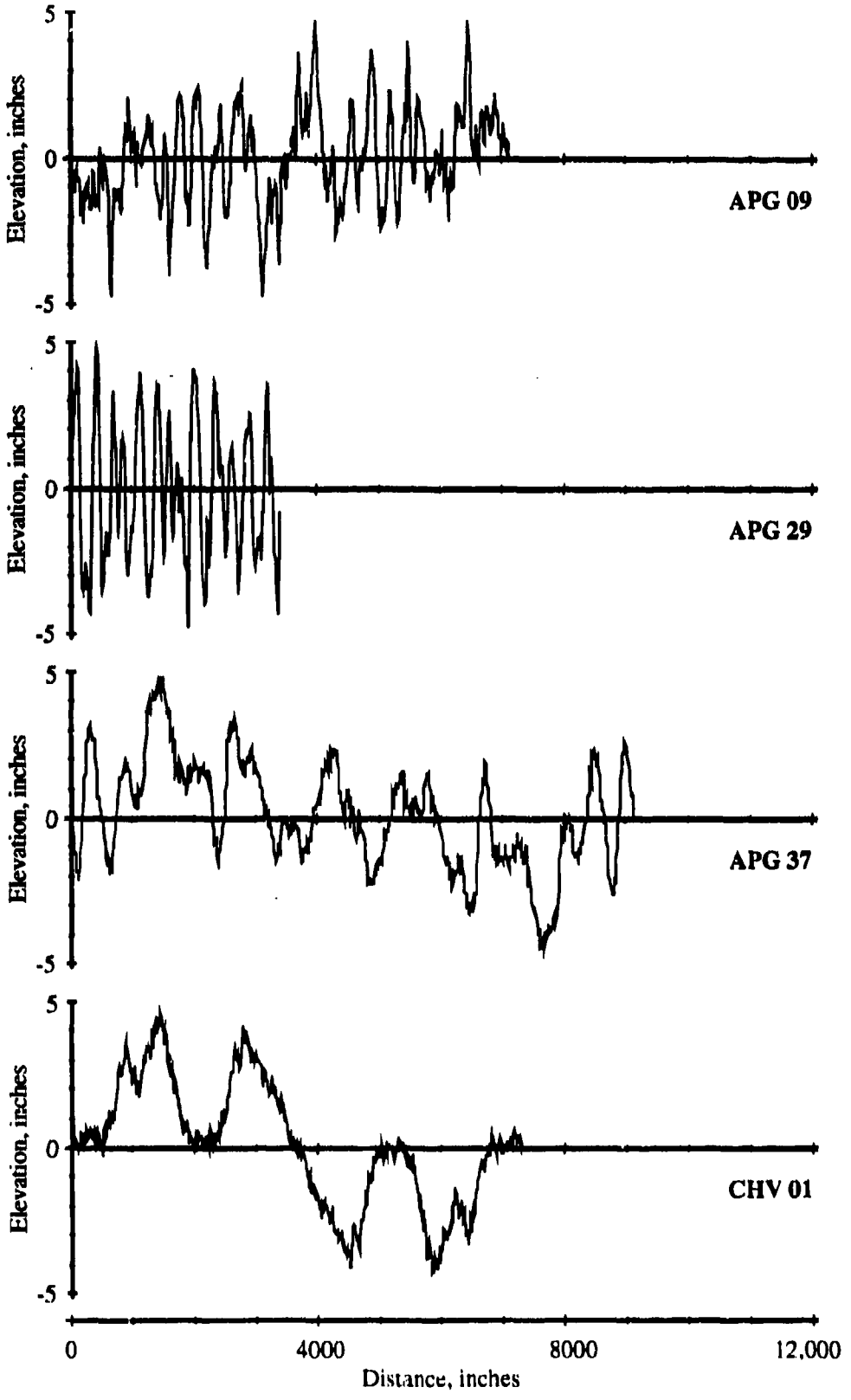

Figure D.1. Road profiles used in quarter-HMMWV testing

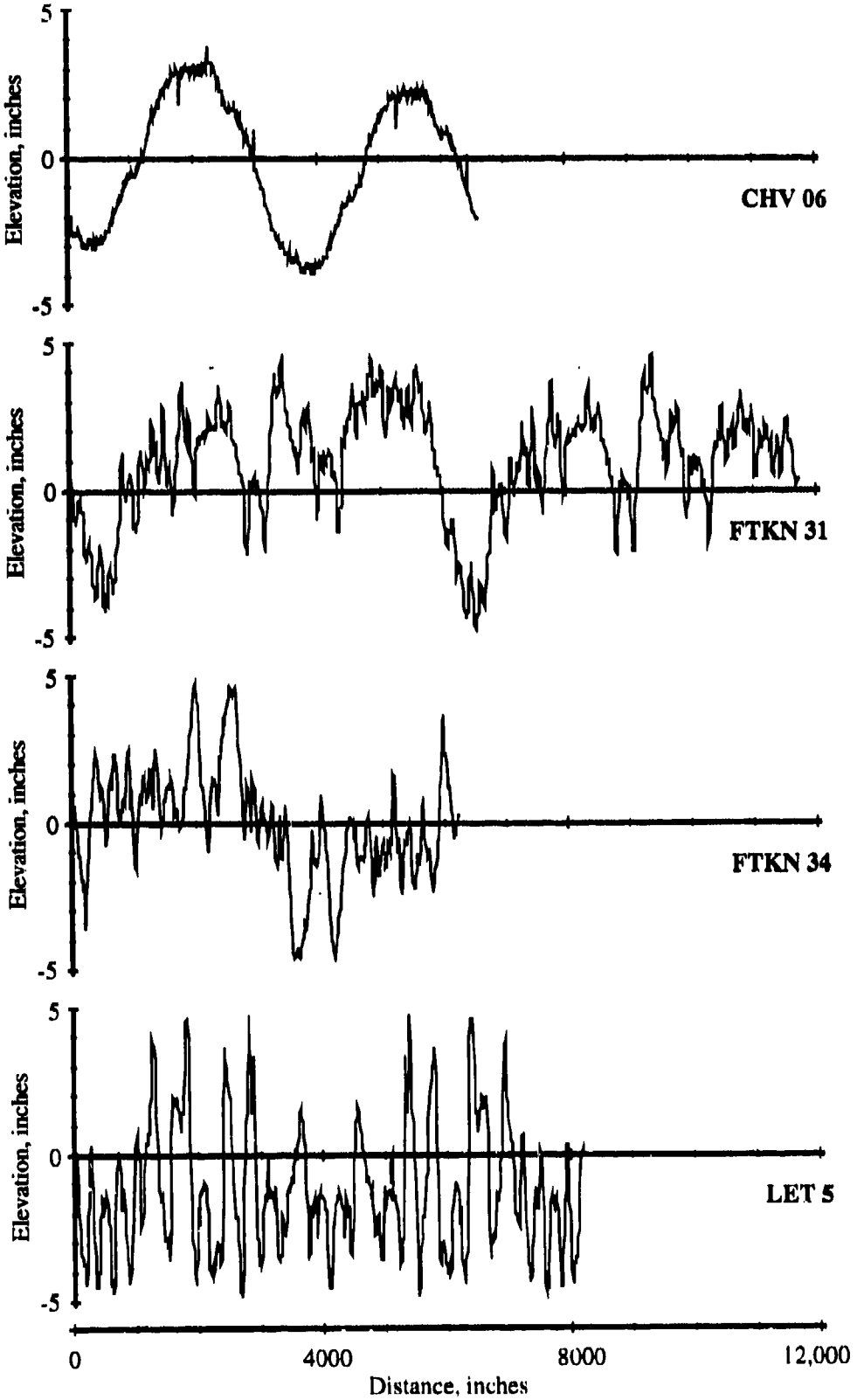

Figure D.1 (continued). Road profiles used in quarter-HMMWV testing

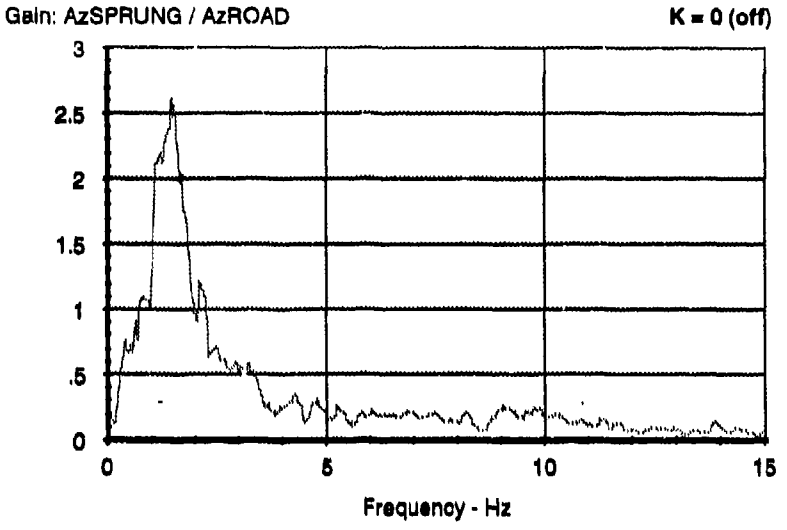

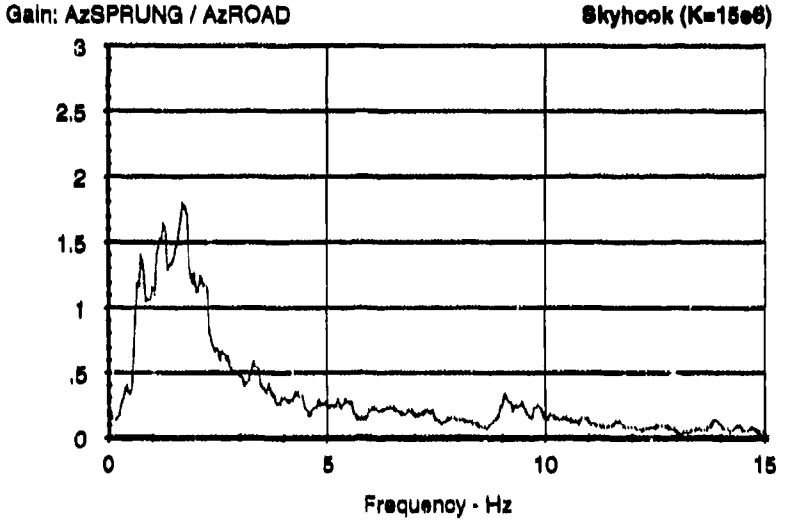

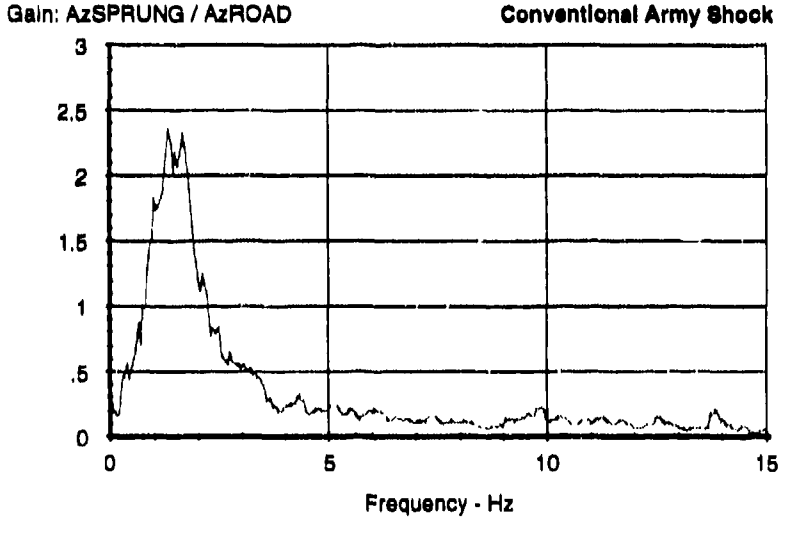

Figure D.2. Sprung mass acceleration transfer function gains for APG 09

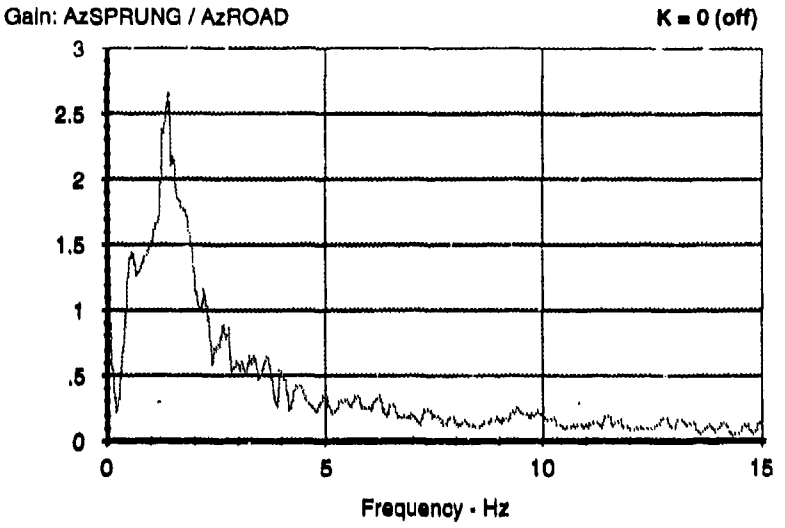

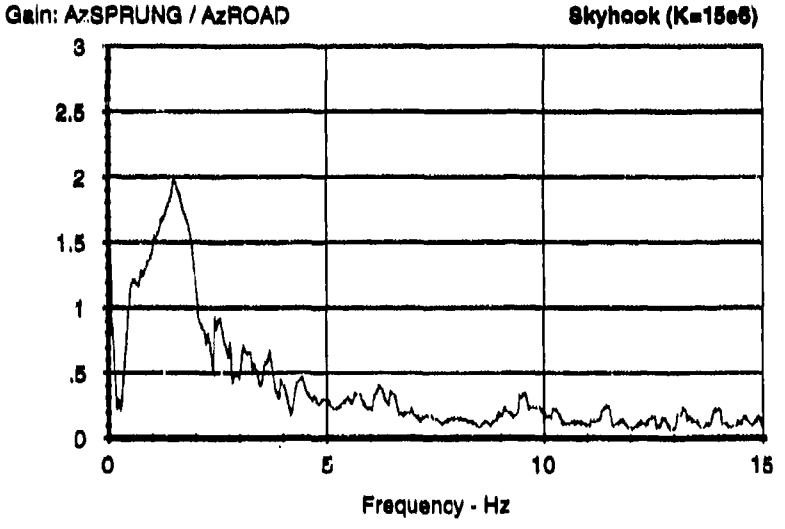

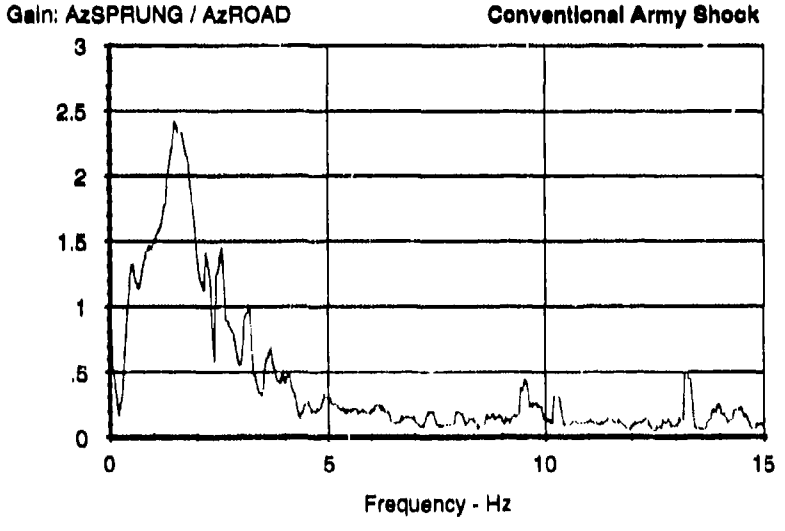

Figure D.3. Sprung mass acceleration transfer function gains for APG 29

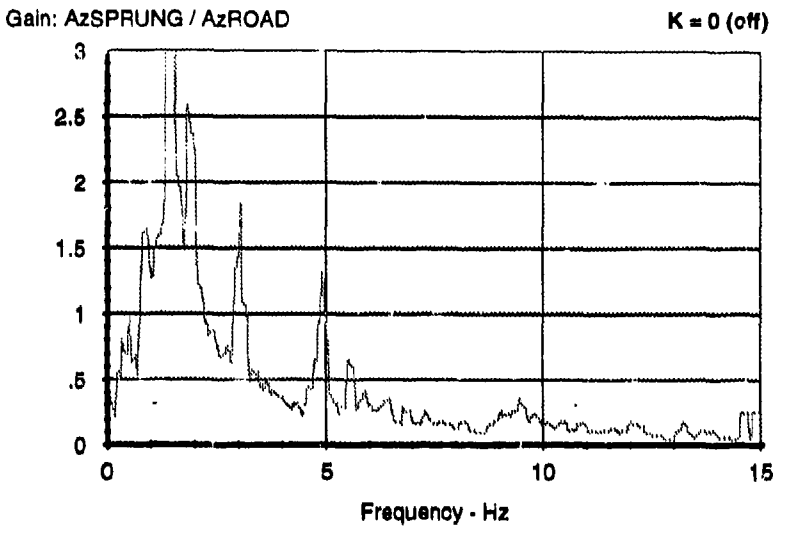

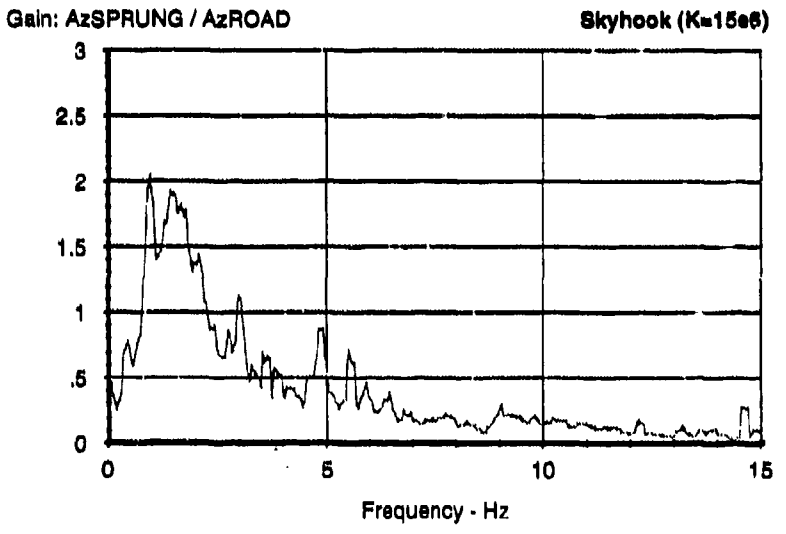

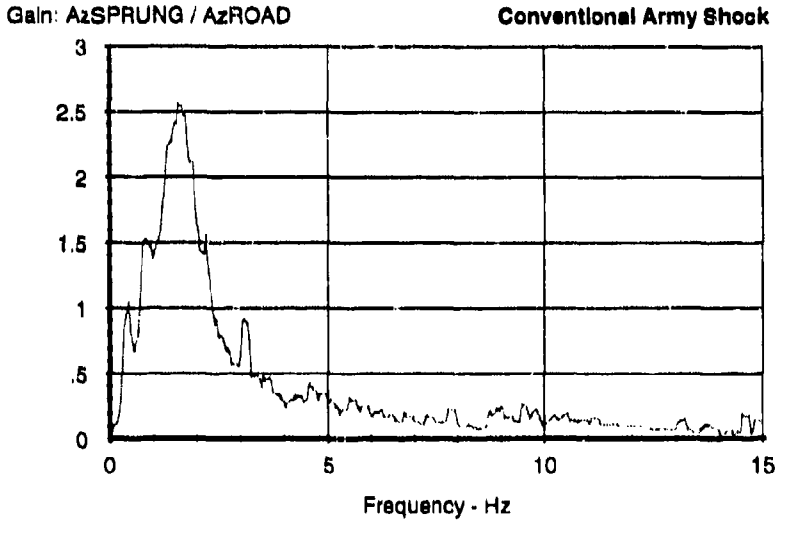

Figure D.4. Sprung mass acceleration transfer function gains for APG 37

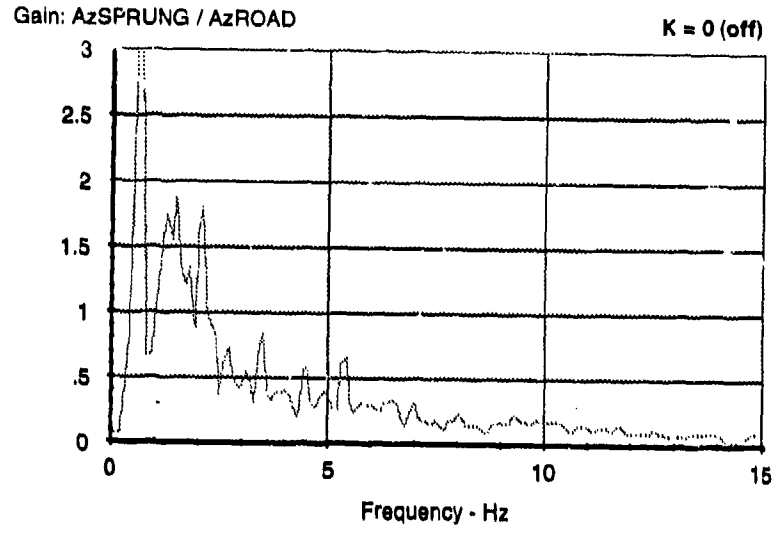

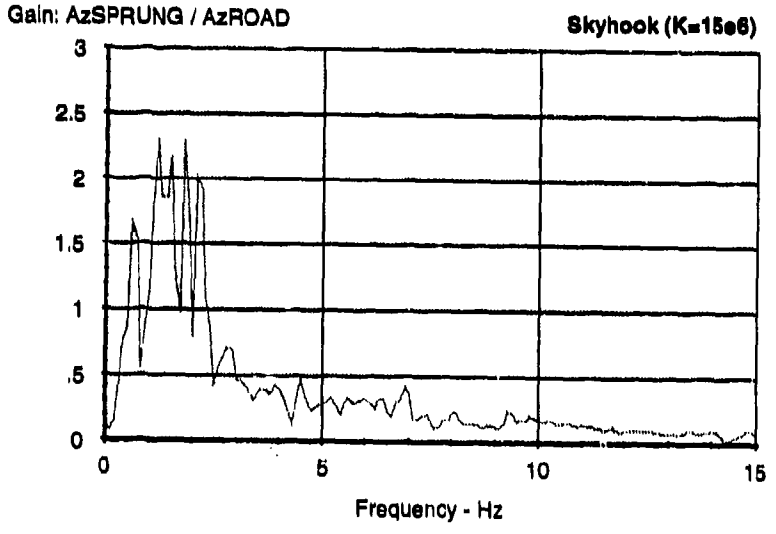

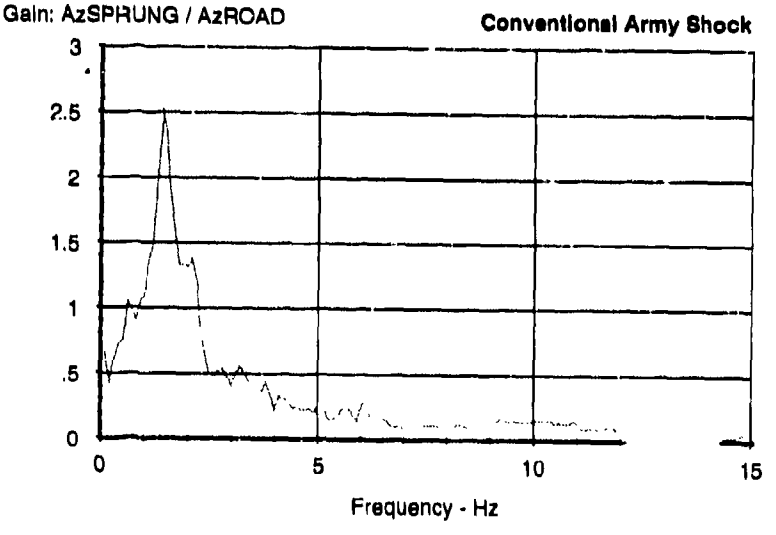

Figure D.5. Sprung mass acceleration transfer function gains for CHV 01

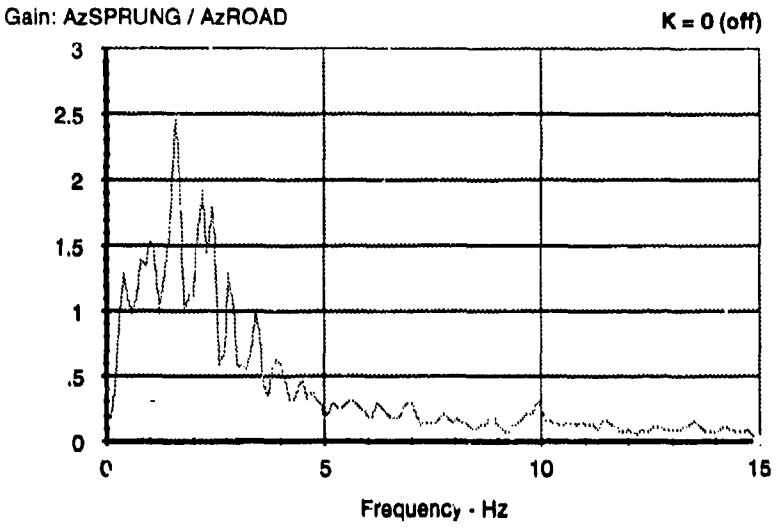

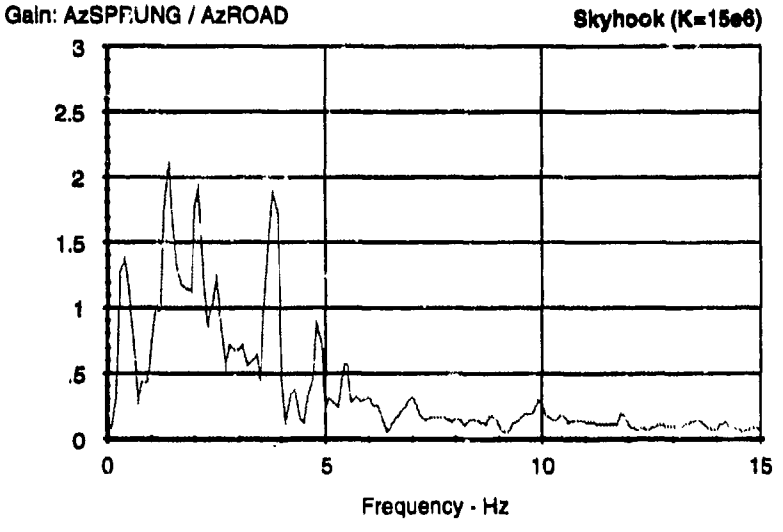

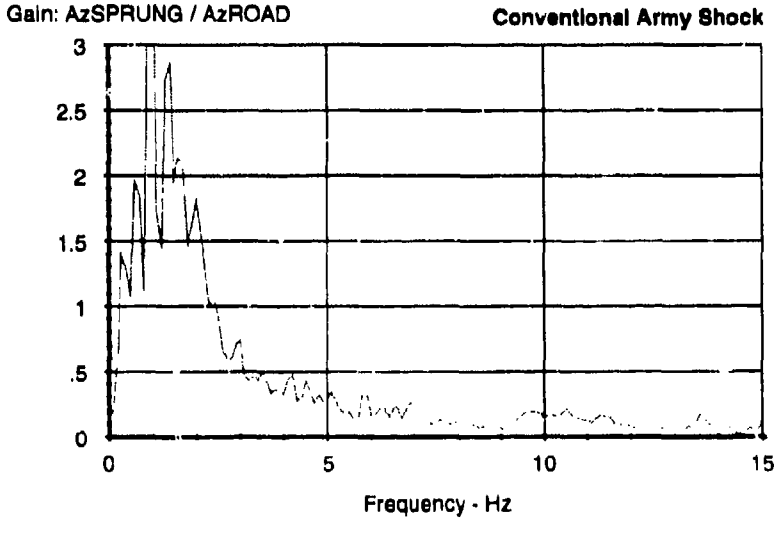

Figure D.6. Sprung mass acceleration transfer function gains for CHV 06

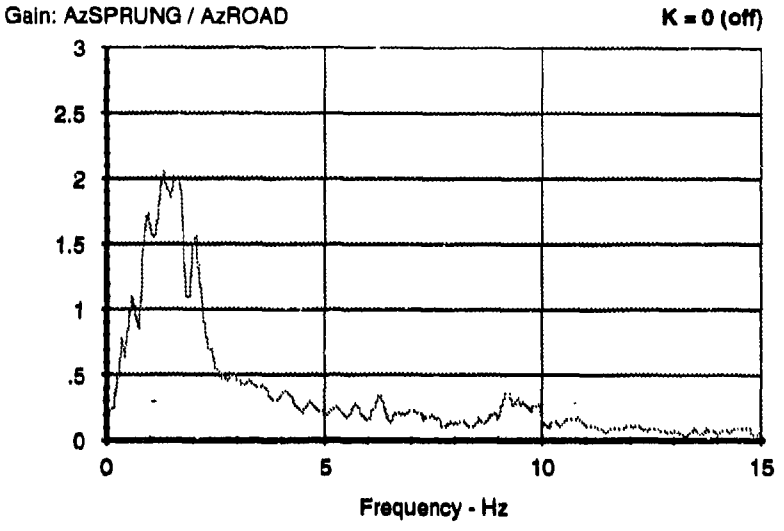

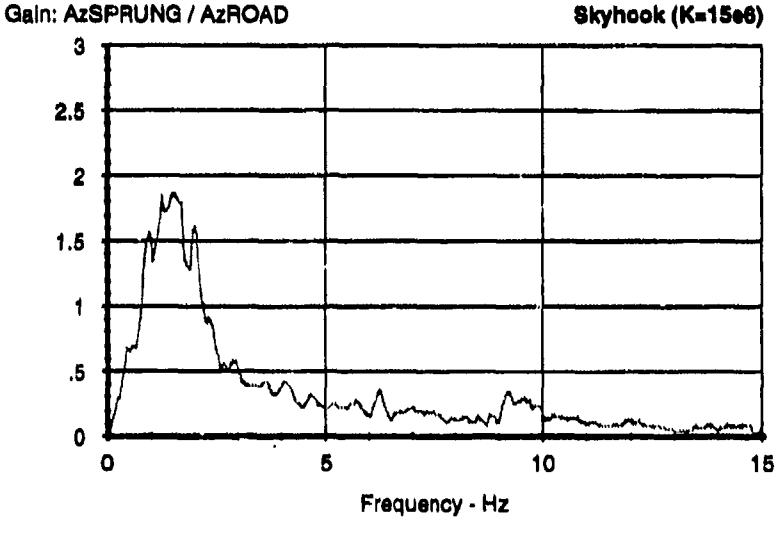

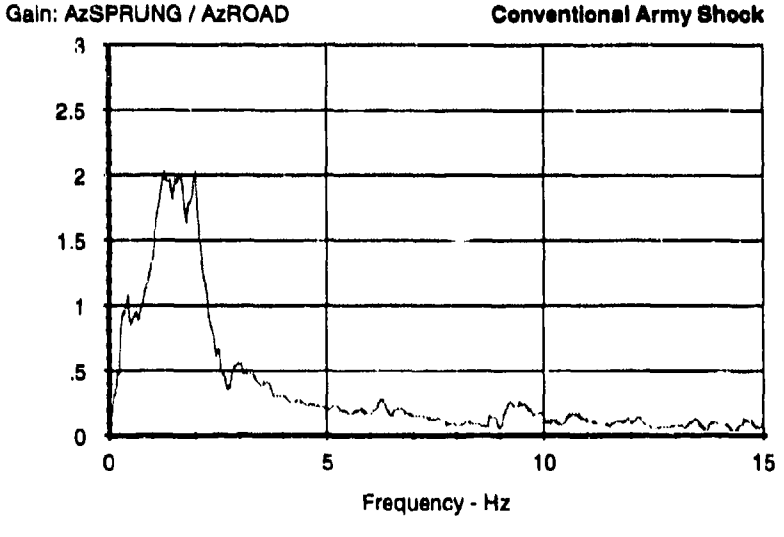

Figure D.7. Sprung mass acceleration transfer function gains for FTKN 31

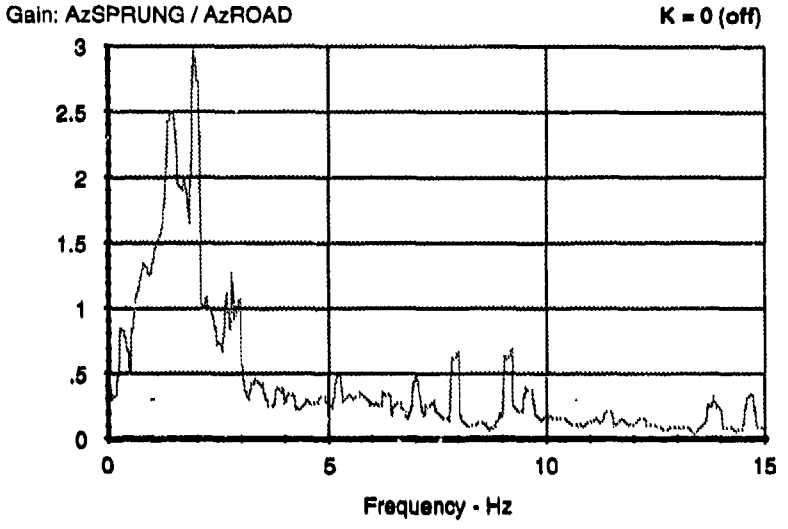

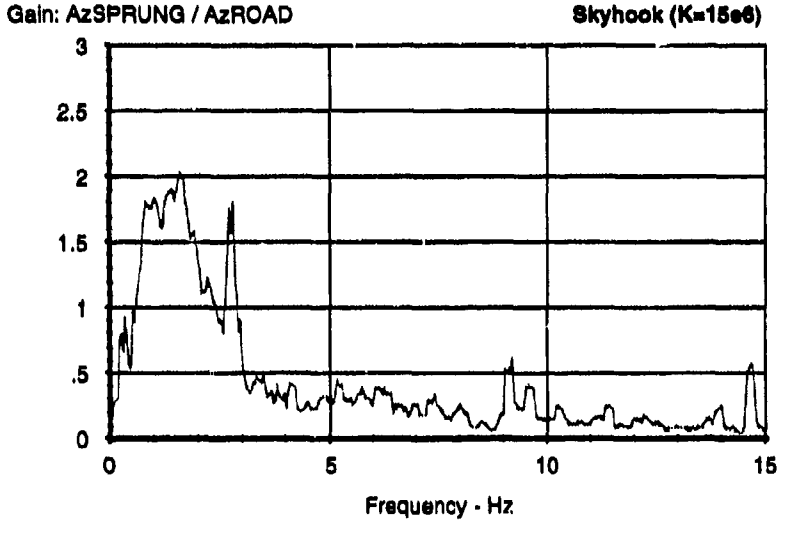

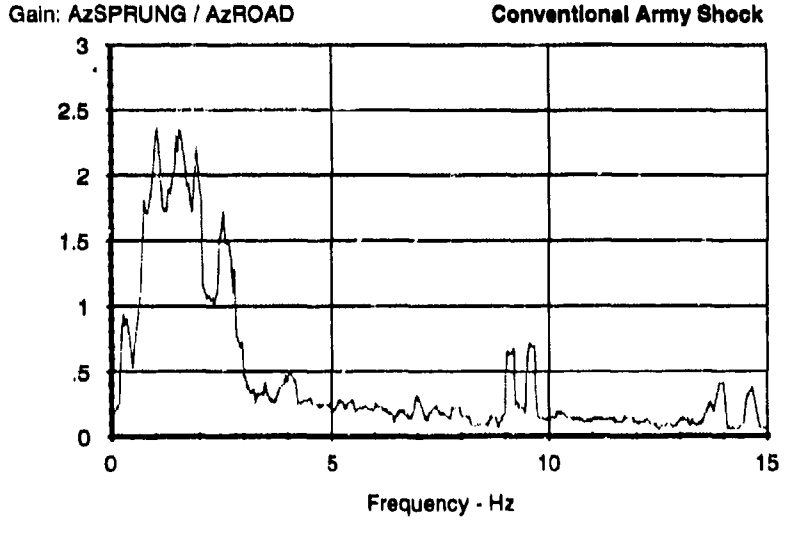

Figure D.8. Sprung mass acceleration transfer function gains for FTKN 34

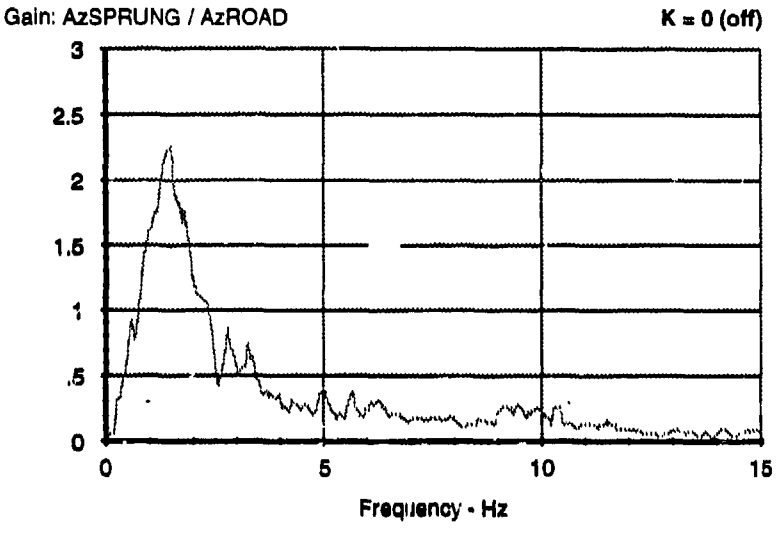

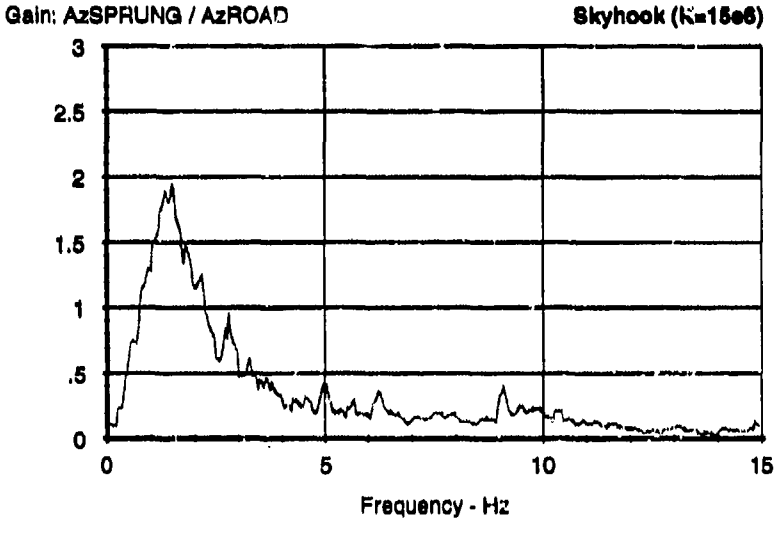

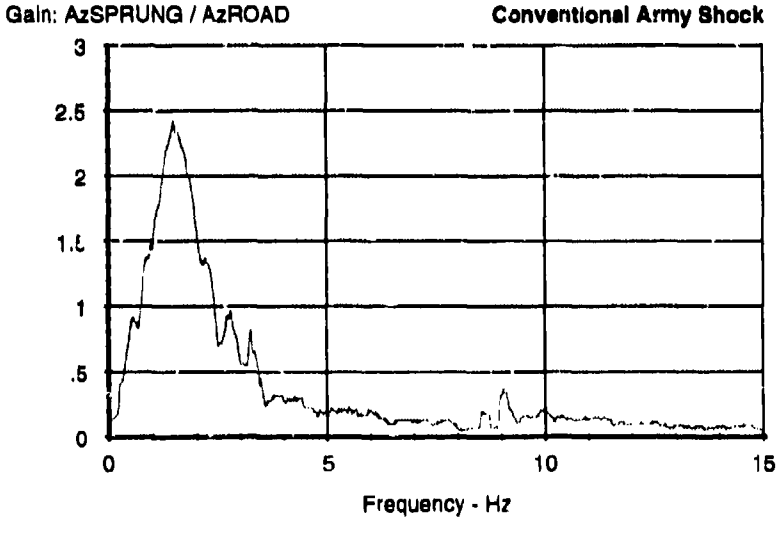

Figure D.9. Sprung mass acceleration transfer function gains for LET 5

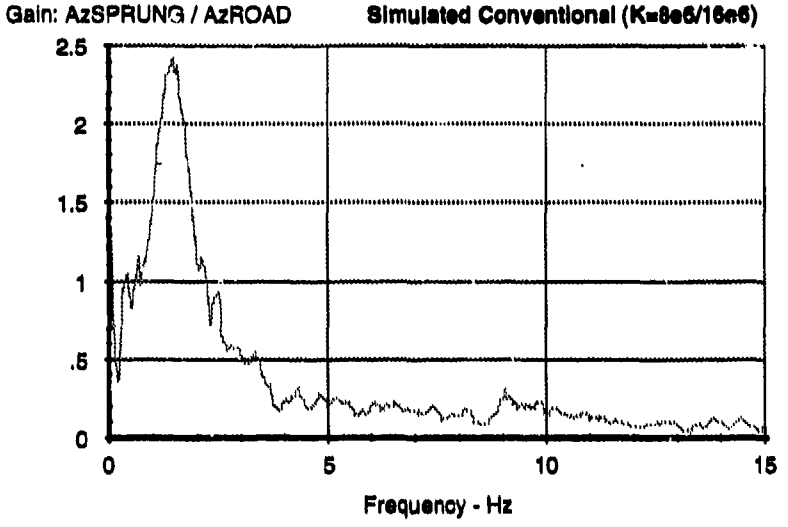

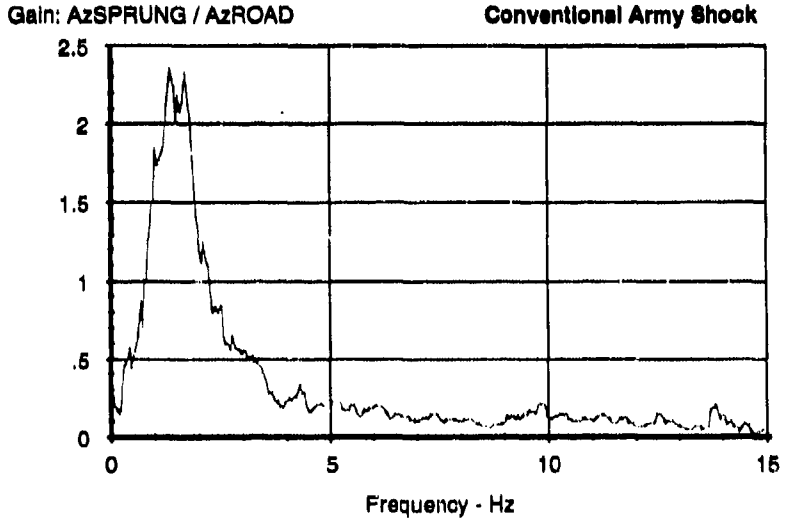

Figure D.10. Sprung mass acceleration transfer function gains measured with simulated and actual conventional shock absorber for APG 09

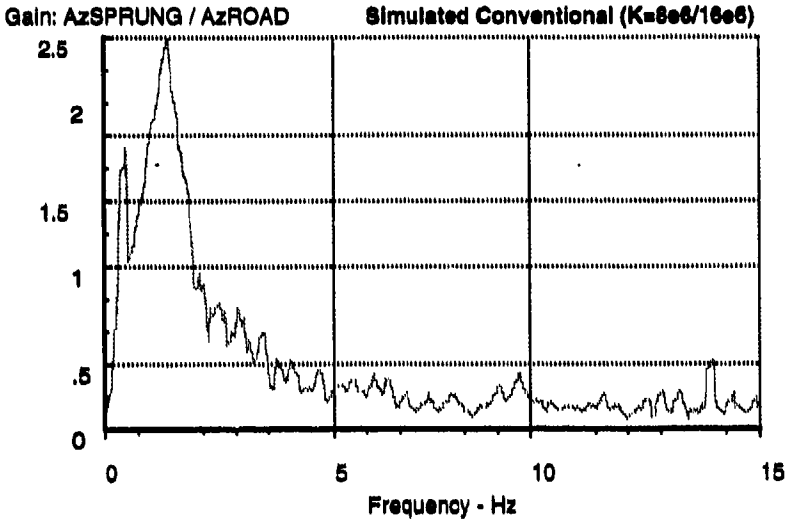

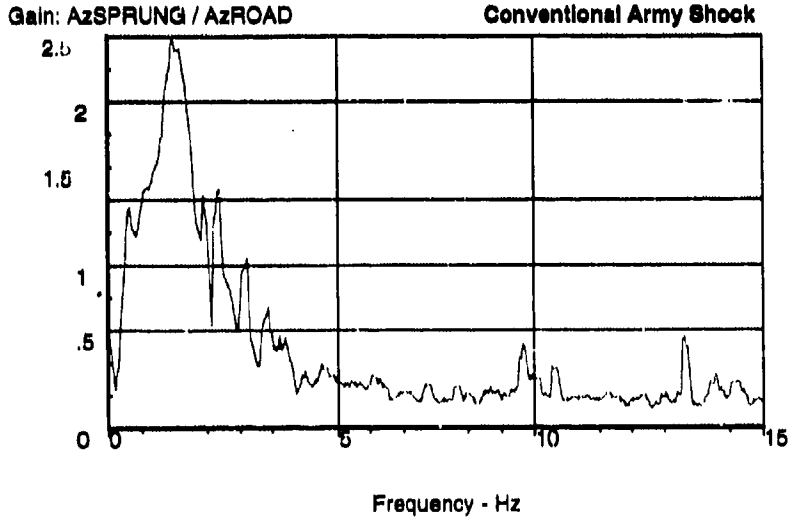

Figure D.11. Sprung mass acceleration transfer function gains measured with simulated and actual conventional shock absorber for APG 29

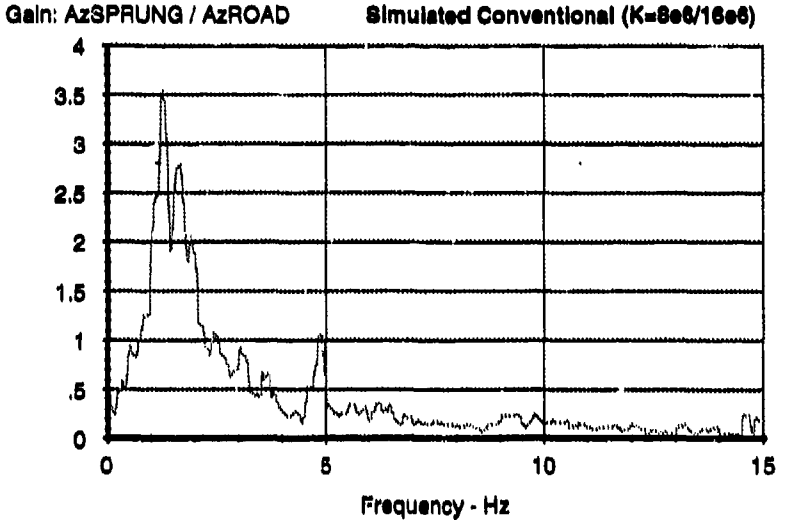

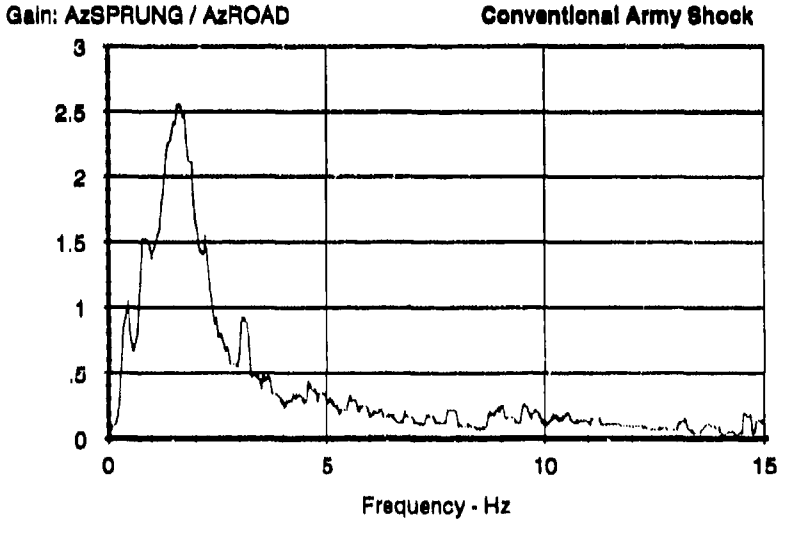

Figure D.12. Sprung mass acceleration transfer function gains measured with simulated and actual conventional shock absorber for APG 37

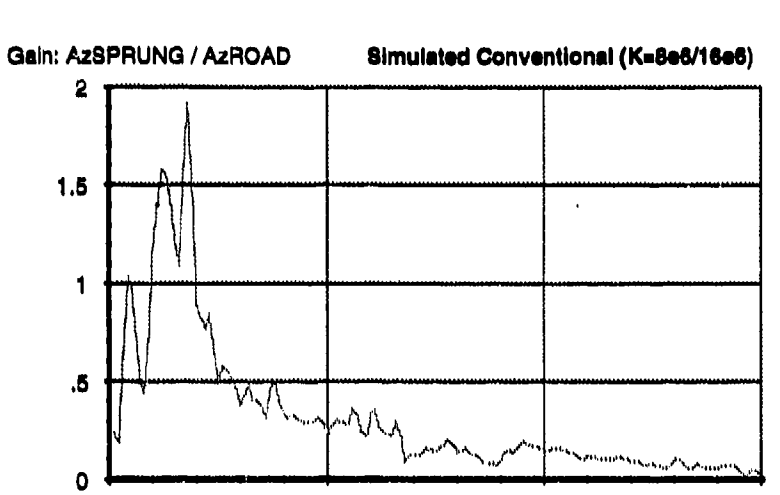

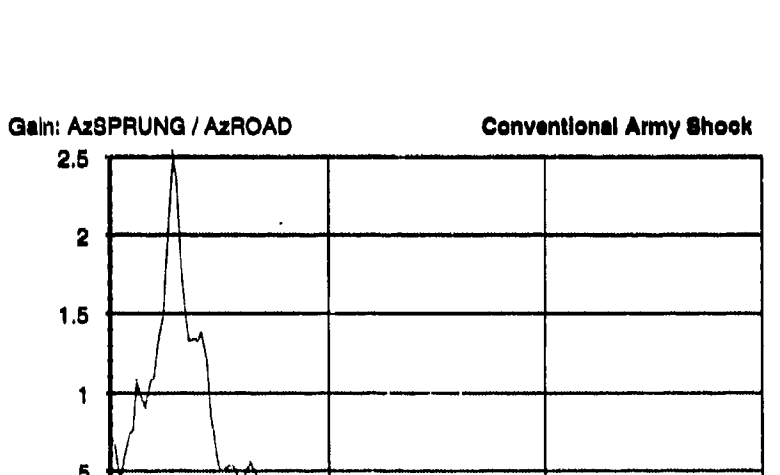

Figure D.13. Sprung mass acceleration transfer function gains measured with simulated and actual conventional shock absorber for CHV 01

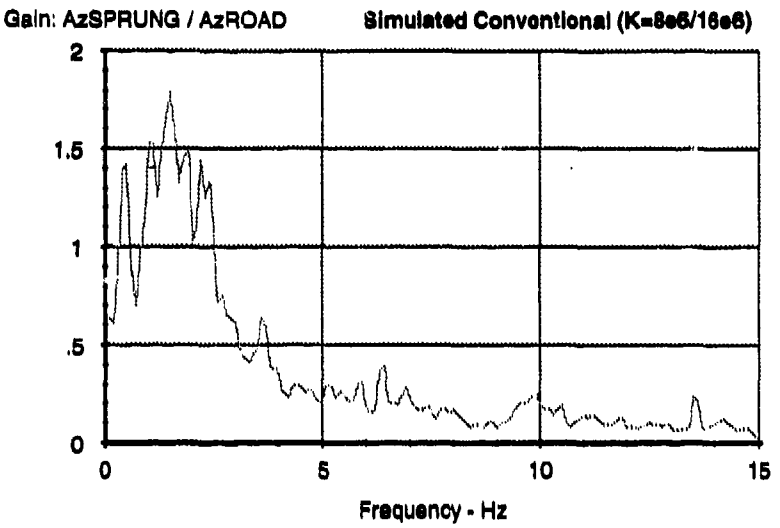

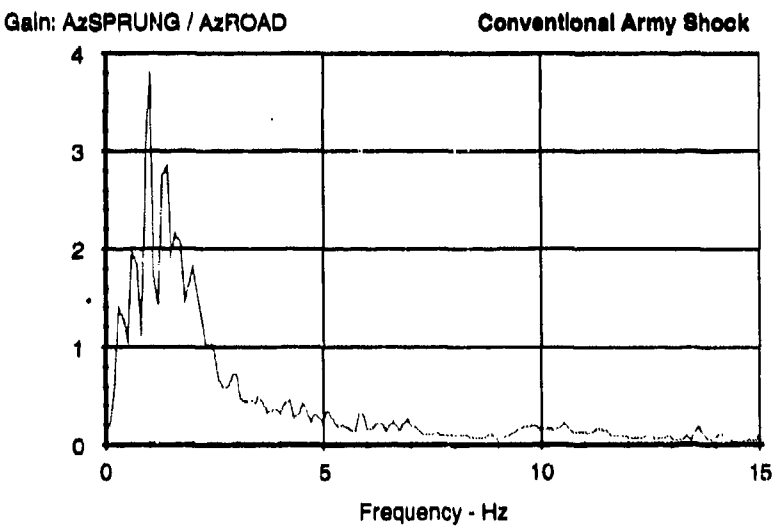

Figure D.14. Sprung mass acceleration transfer function gains measured with simulated and actual conventional shock absorber for CHV 06

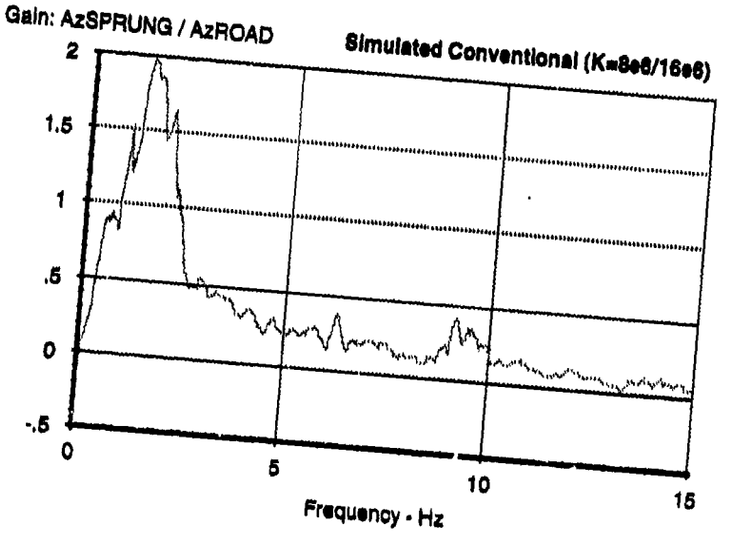

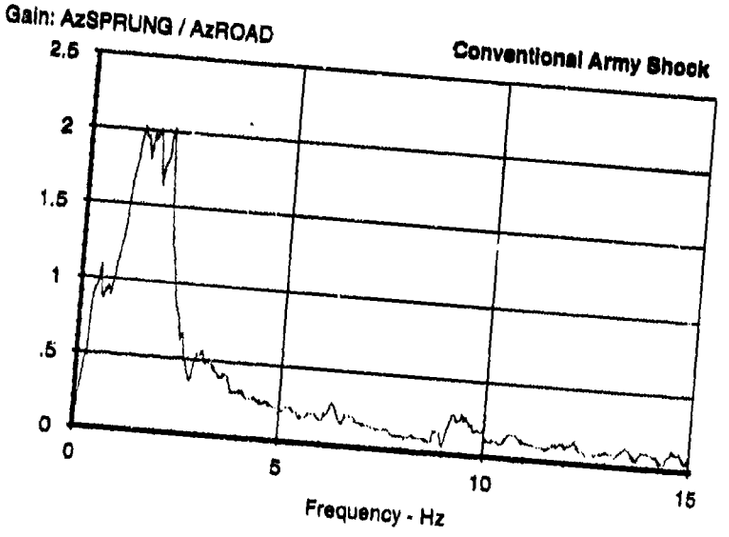

Figure D.15. Sprung mass acceleration transfer function gains measured with simulated and actual conventional shock absorber for FTKN 31

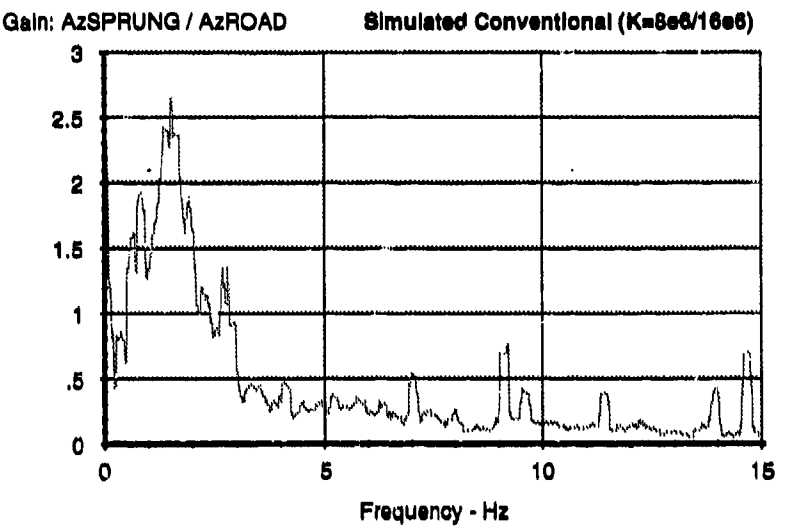

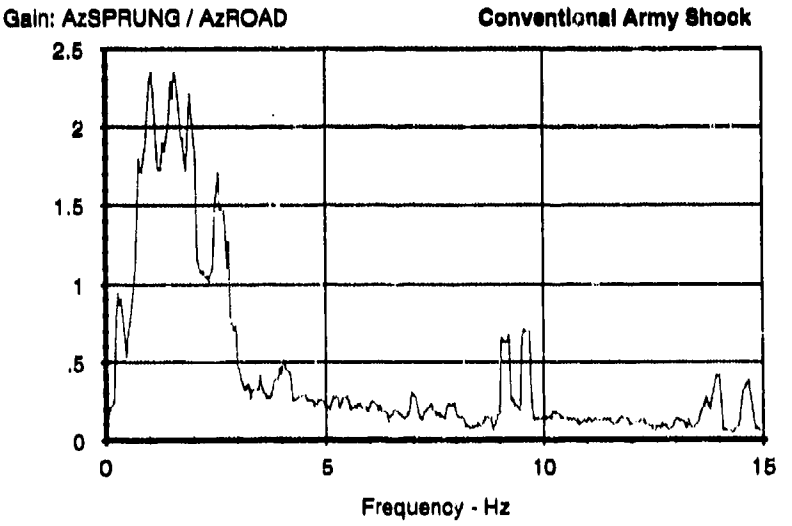

Figure D.16. Sprung mass acceleration transfer function gains measured with simulated and actual conventional shock absorber for FTKN 34

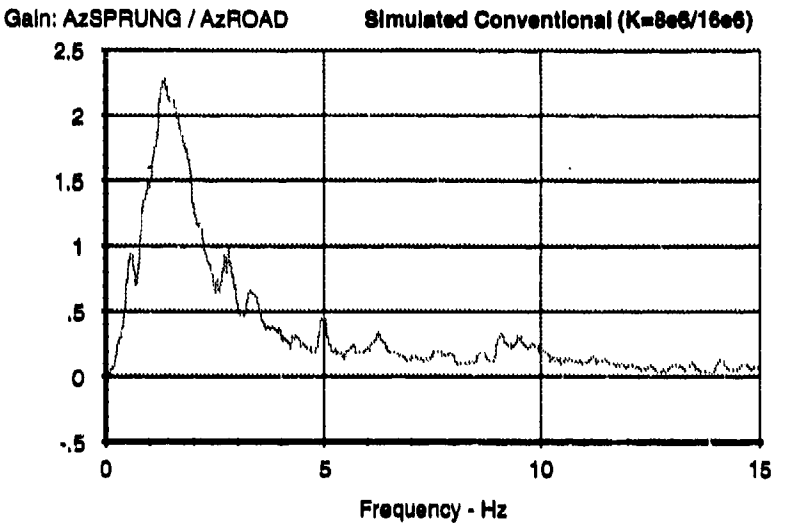

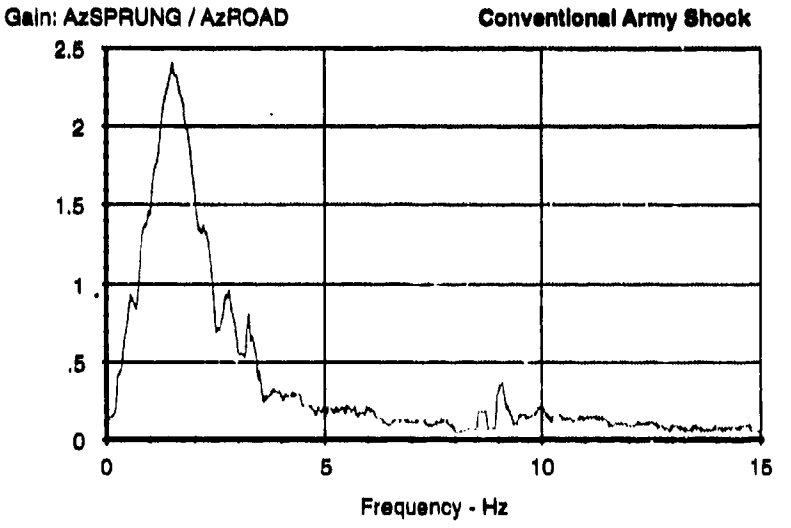

Figure D.17. Sprung mass acceleration transfer function gains measured with simulated and actual conventional shock absorber for LET 5

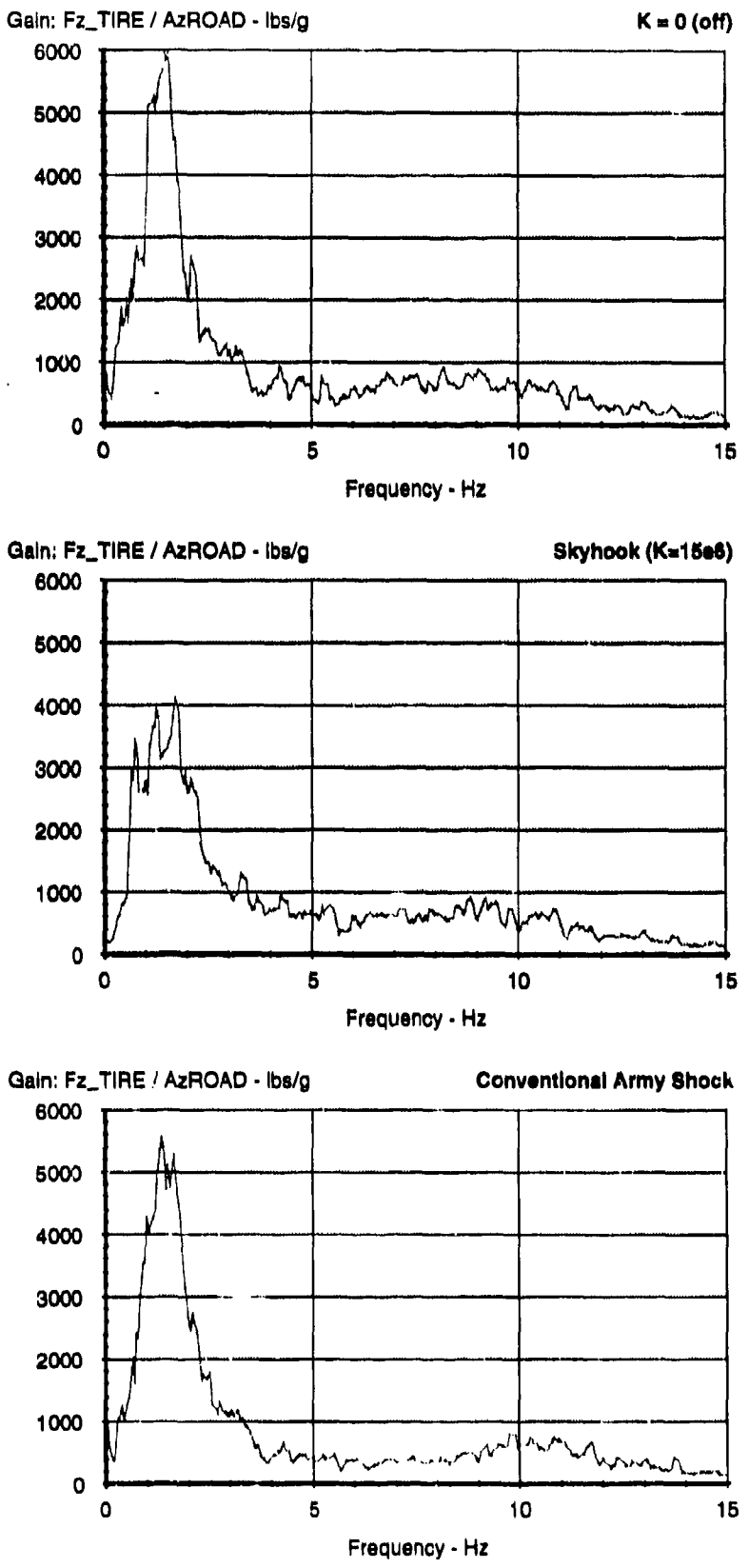

Figure D.18. Tire force transfer function gains for APG 09

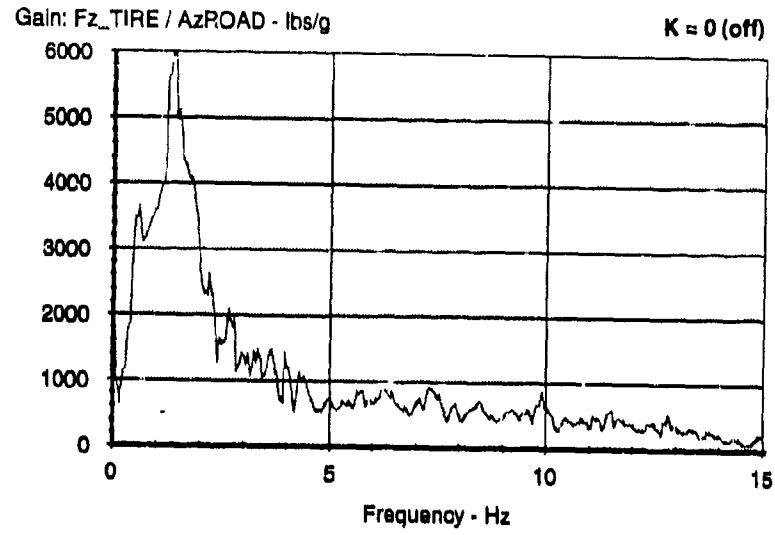

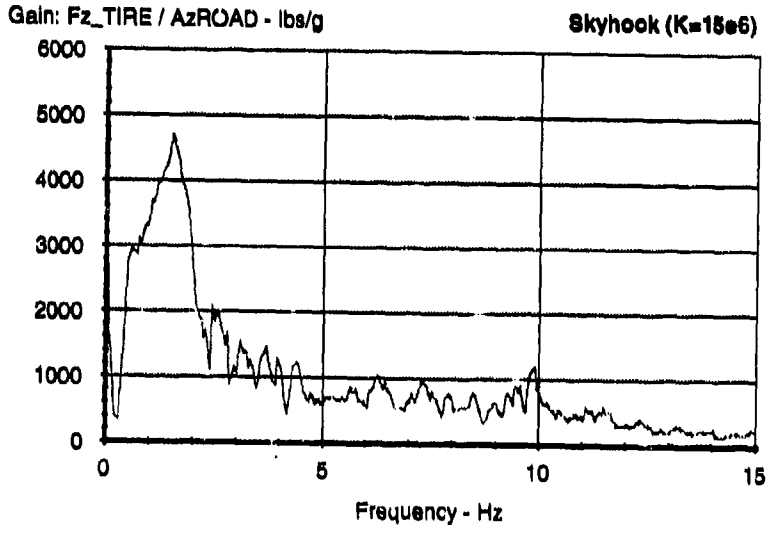

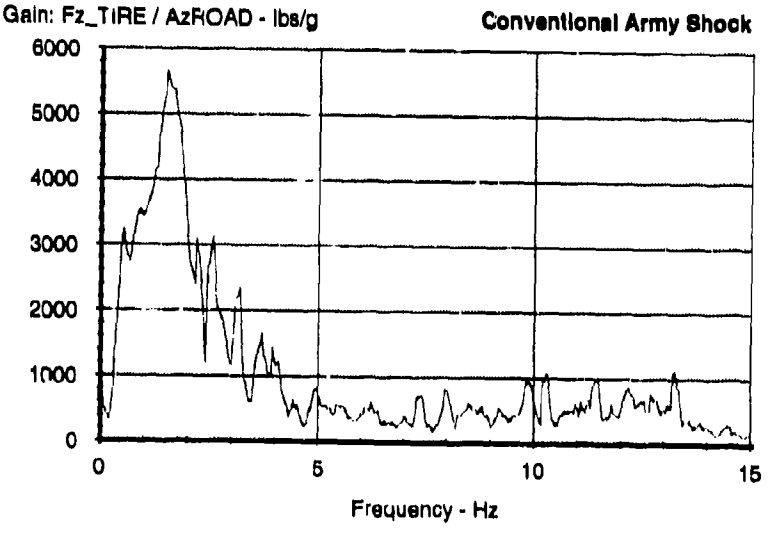

Figure D.19. Tire force transfer function gains for APG 29

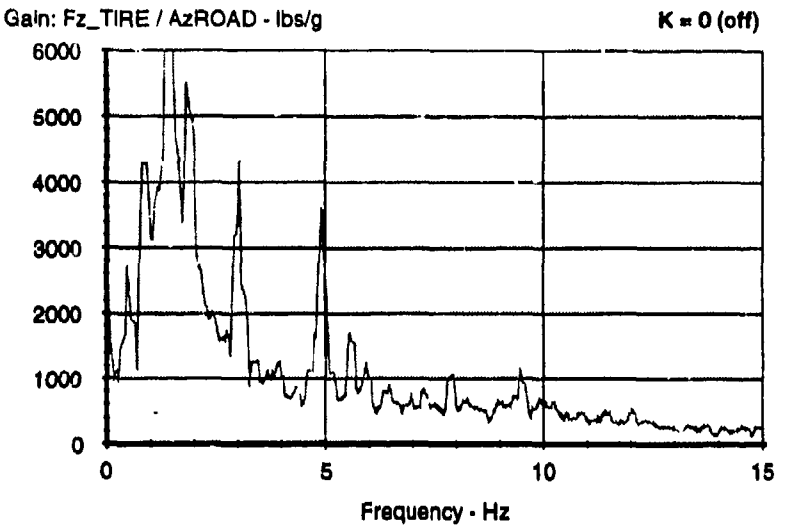

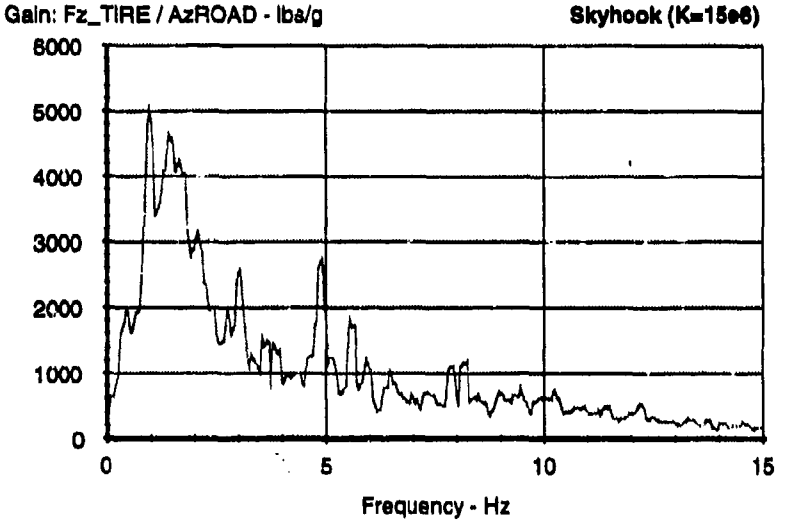

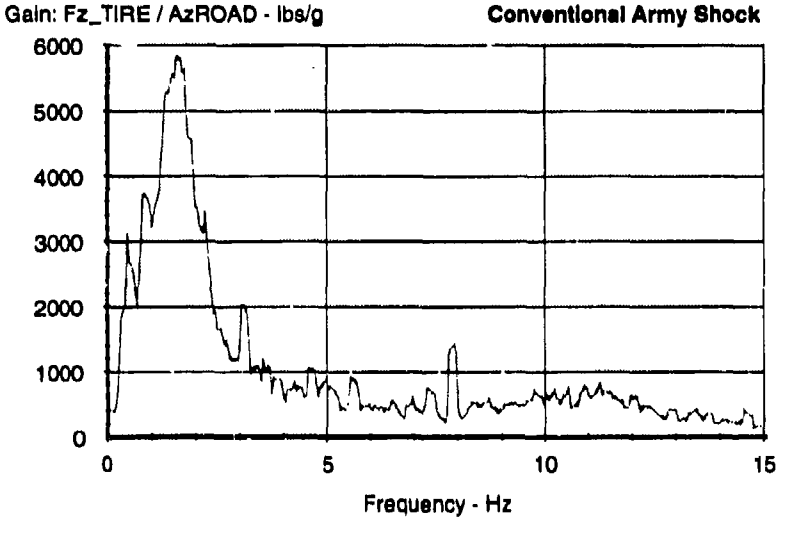

Figure D.20. Tire force transfer function gains for APG 37

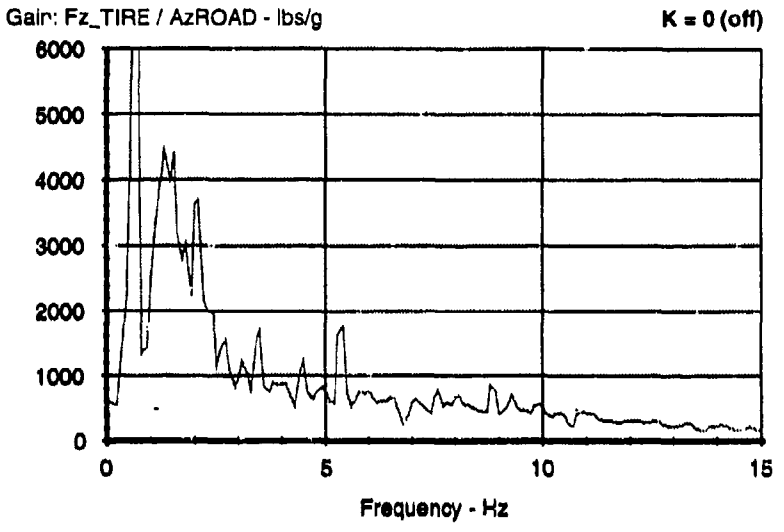

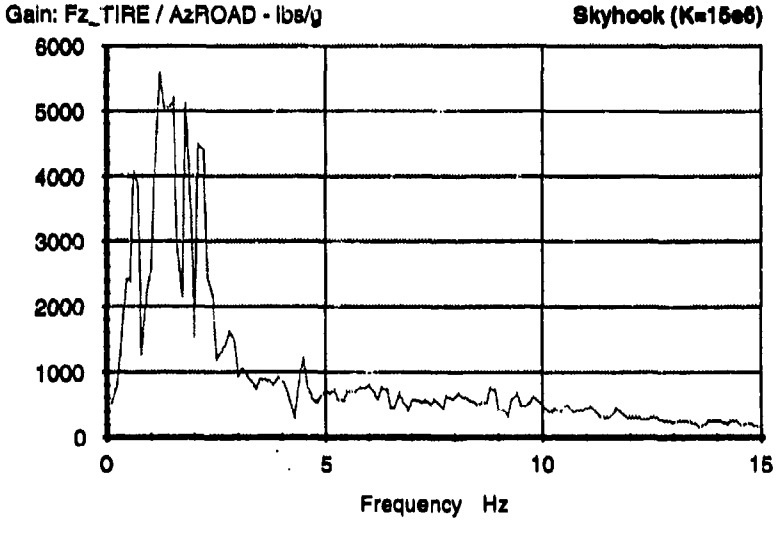

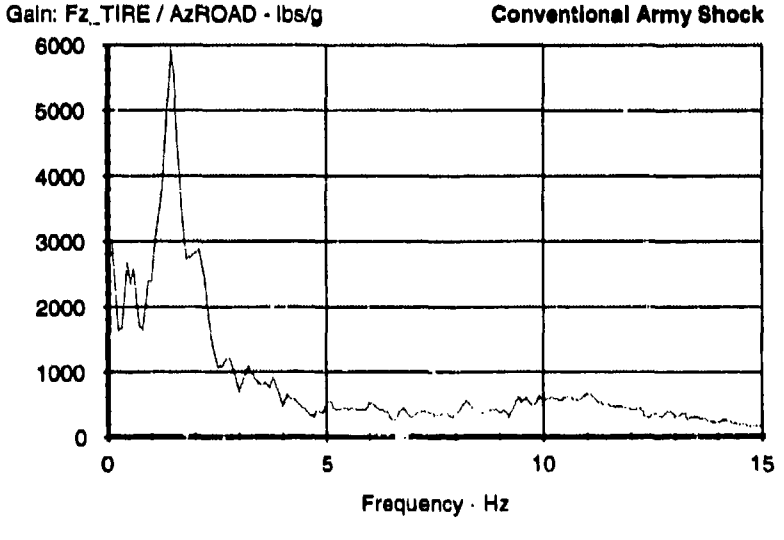

Figure D.21. Tire force transfer function gains for CHV 01

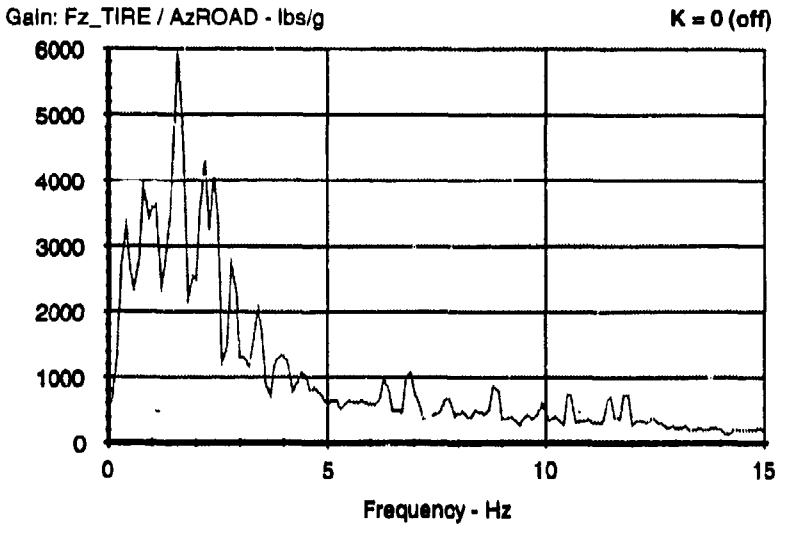

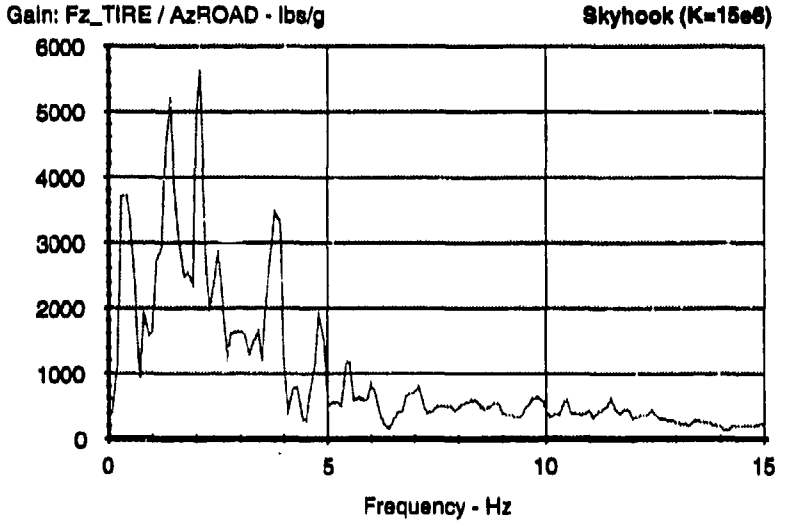

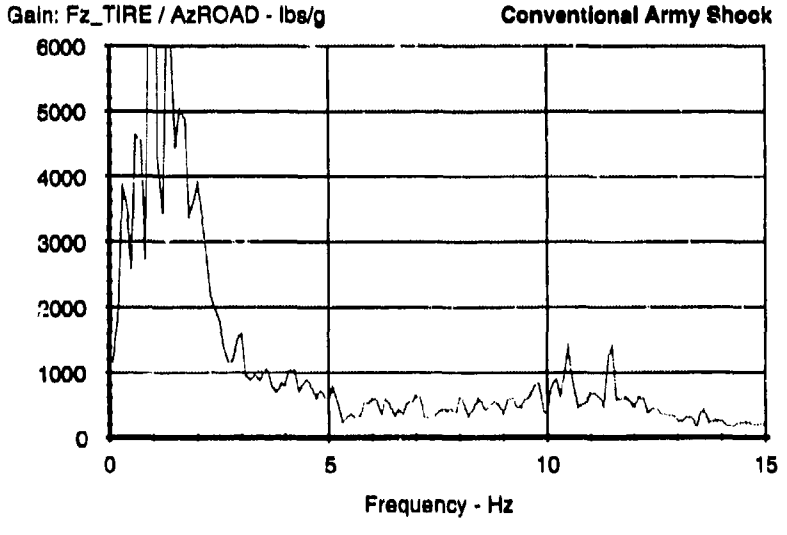

Figure D.22. Tire force transfer function gains for CHV 06

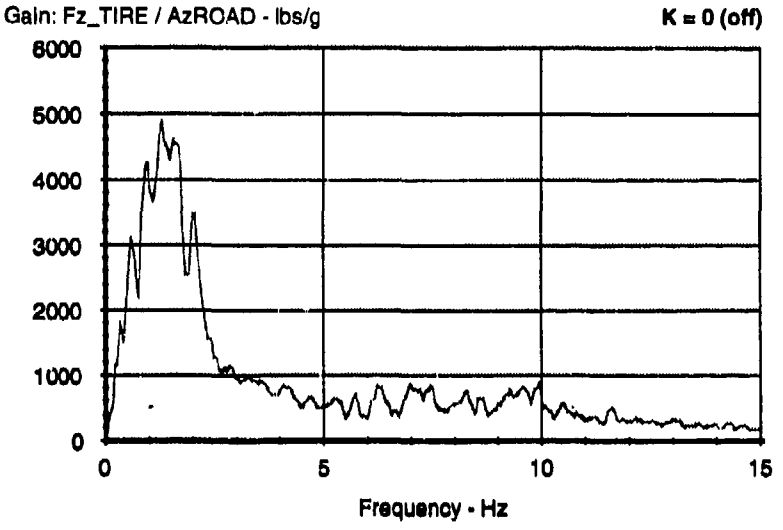

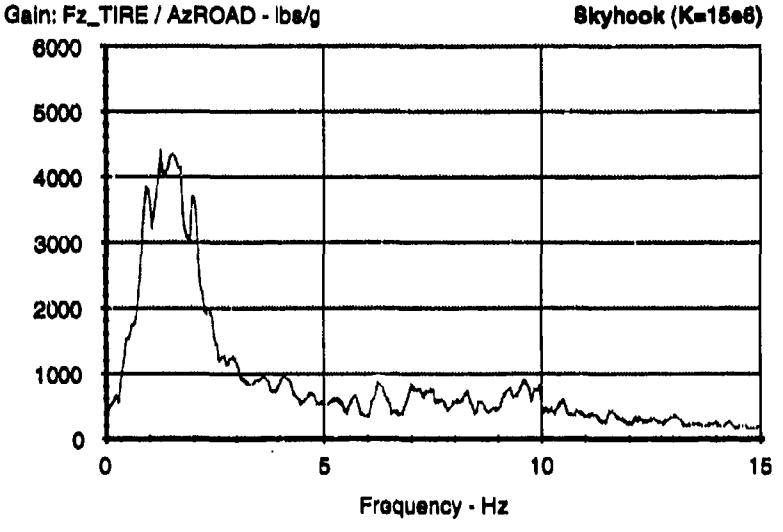

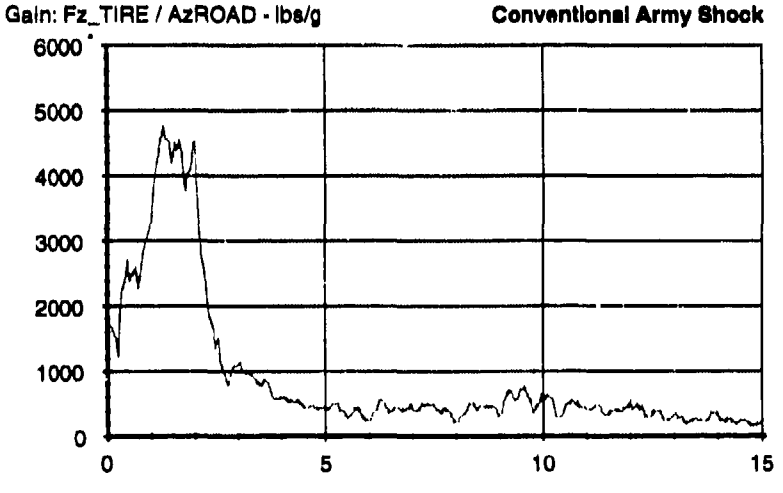

Figure D.23. Tire force transfer function gains for FTKN 31

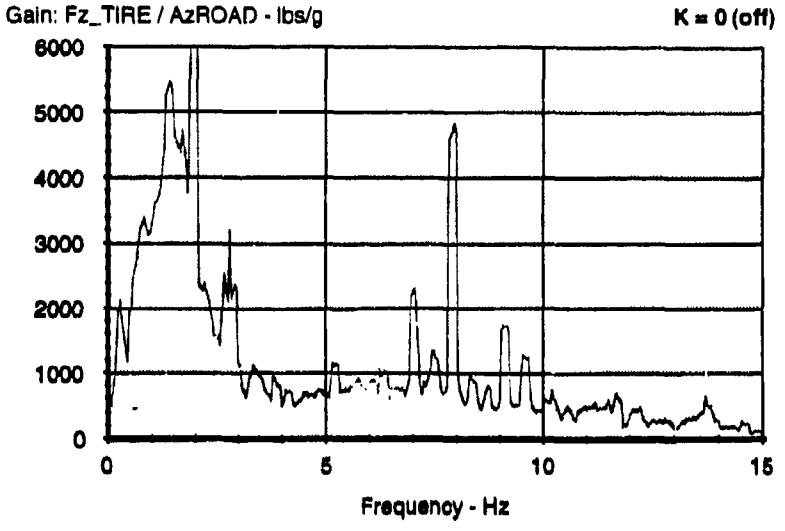

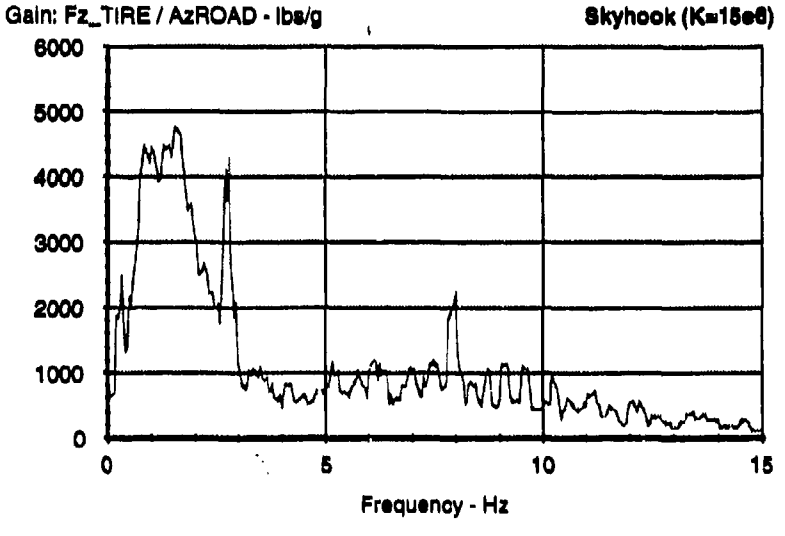

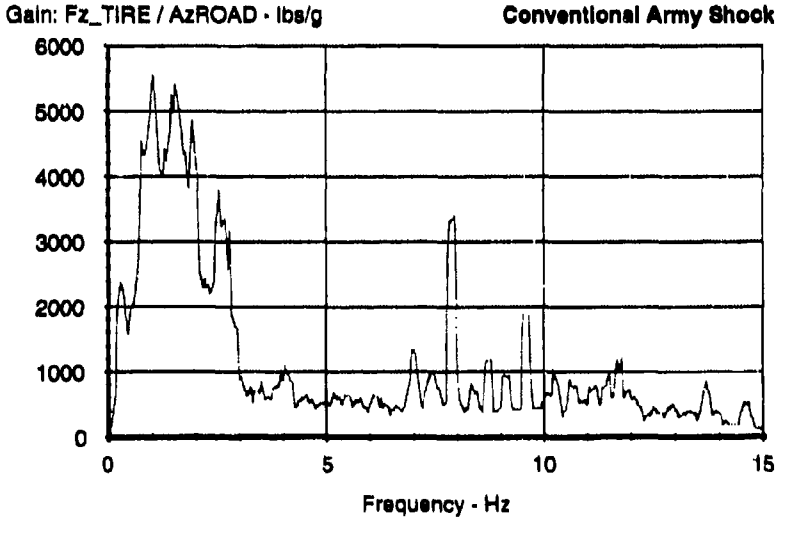

Figure D.24. Tire force transfer function gains for FTKN 34

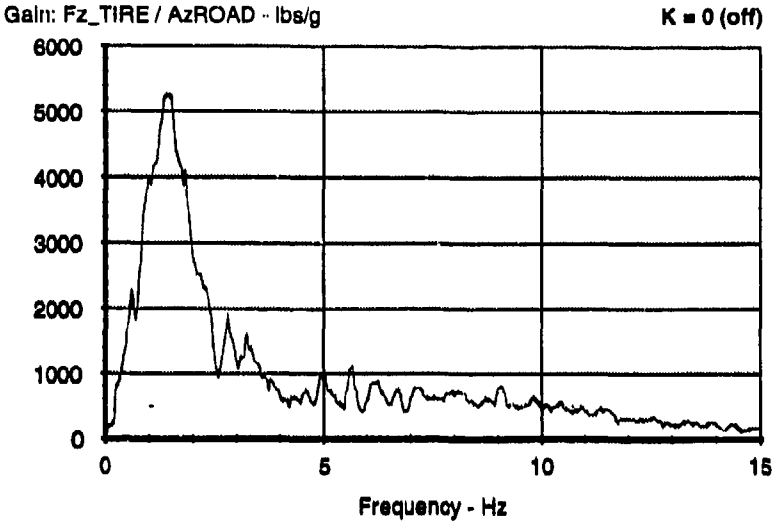

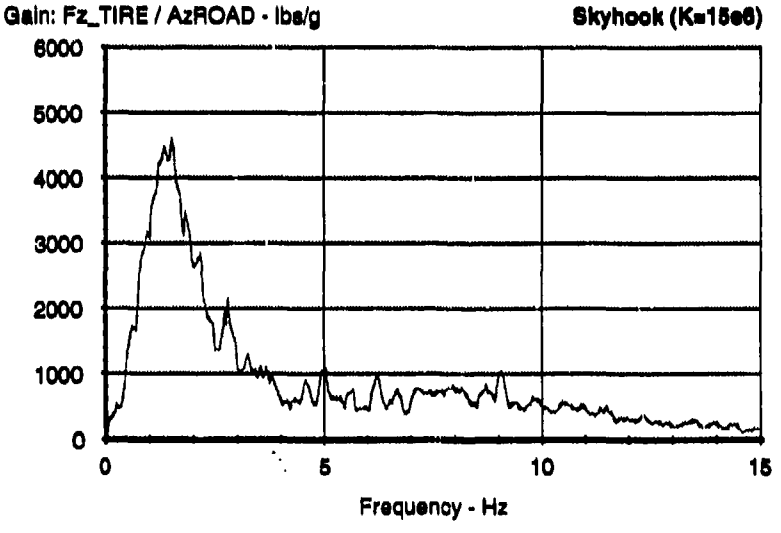

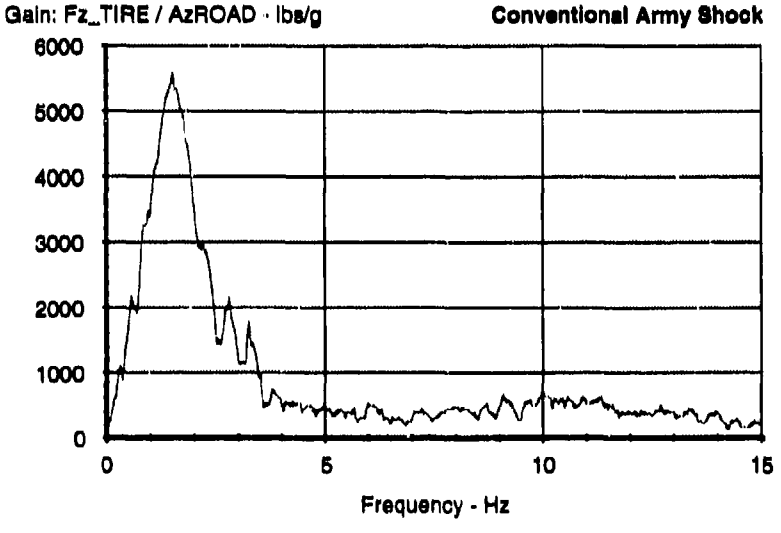

Figure D.25. Tire force transfer function gains for LET 5